# Visual landmark coding and dynamic coupling with path integration circuits in area 29e of the rodent parahippocampal cortex

Gorkem Secer[1,3,4,*], Bharath Krishnan[1,2,3,*], Noah J. Cowan[3,4,5,#] and James J. Knierim[1,3,6,#]

[1]Zanvyl Krieger Mind/Brain Institute, Johns Hopkins University
[2]Department of Biomedical Engineering, Johns Hopkins University
[3]Kavli Neuroscience Discovery Institute, Johns Hopkins University
[4]Laboratory for Computational Sensing and Robotics, Johns Hopkins University
[5]Department of Mechanical Engineering, Johns Hopkins University
[6]Solomon H. Snyder Department of Neuroscience, Johns Hopkins University

* - These authors contributed equally, # - These authors jointly supervised this work

**The brain relies on external landmarks to anchor internal spatial representations. The neural mechanisms underlying this process and the sources of landmark signals remain unknown in mammals. Here, we simultaneously recorded single neurons across five parahippocampal regions in rats navigating a virtual reality environment that preserved natural locomotion. Area 29e, an understudied parahippocampal field, displayed strong locking to visual landmarks under conditions in which neurons in the other regions, such as the medial entorhinal cortex, decoupled their spatial firing from the landmarks. Compared to the other regions, area 29e neurons also displayed weaker theta modulation, stronger gamma rhythmicity, stronger egocentric head-direction tuning, and enhanced landmark contrast sensitivity. The loss of landmark anchoring in non-29e parahippocampal neurons was preceded by a decline of gamma-band influence from 29e to medial entorhinal cortex. Together, these findings position 29e as a specialized visuospatial hub that may carry landmark signals for anchoring parahippocampal representations of space to the external world.**

Neural systems display internal dynamics and represent explicit cognitive states in the absence of overt sensory stimulation. Sensory input does not drive a "blank slate" of quiescent neurons waiting for input about the external world. Rather, such input modulates a rich set of internally generated representations that perform important neural computations that are critical for the proper functioning of the system. Understanding the interplay between external sensory input and endogenous neural dynamics is key toward understanding the principles of neural computation. Spatial navigation provides an ideal model for dissecting this interplay. The hippocampal-parahippocampal system, coordinated by endogenous theta and gamma oscillations (*1–5*), updates a position signal on the animal's cognitive map by integrating self-motion-generated cues over time—a process known as path integration (*6–9*). To prevent or correct error from accumulating in this incremental estimate of the animal's position in the world, stable external landmarks must be incorporated into the internally generated map to anchor the map to an external reference frame (*10–13*).

Although the neural correlates of path integration (e.g., grid cells and speed cells) are relatively well characterized in rodent hippocampal and parahippocampal areas (*9*, *14–19*), the sources of external visual landmark signals that calibrate and correct this internal computation remain unclear. Area 29e is a relatively understudied region interposed between the dorsal presubiculum (PR) and the parasubiculum (PA). Recent work suggests that rodent area 29e is homologous with the primate region prostriata, which has been implicated in processing rapidly moving stimuli in the far peripheral visual field (*20–22*). These observations, together with 29e's distinctive connectivity (*23–28*)—direct inputs from dorsal lateral geniculate nucleus and V1 and projections to PR and medial entorhinal cortex (MEC)—identify 29e as a potential candidate relay of visual landmark signals to parahippocampal circuits supporting path integration in rodents. Using a virtual reality system that allowed us to decouple self-motion signals from visual landmarks in a closed-loop feedback circuit (*12*, *29*, *30*), we found that 29e neurons had directionally tuned response curves that were tightly coupled to distal visual landmarks, even under conditions in which the firing fields of parahippocampal neurons became decoupled from the landmark frame of reference. Furthermore, the normal theta- and gamma-mediated communication between 29e and MEC became disrupted when the landmarks lost control of the MEC spatial firing. Our findings provide a physiological and functional characterization of area 29e in freely moving animals, revealing the neural dynamics by

which the parahippocampal system integrates visual landmark information with the internal path-integration estimate of position.

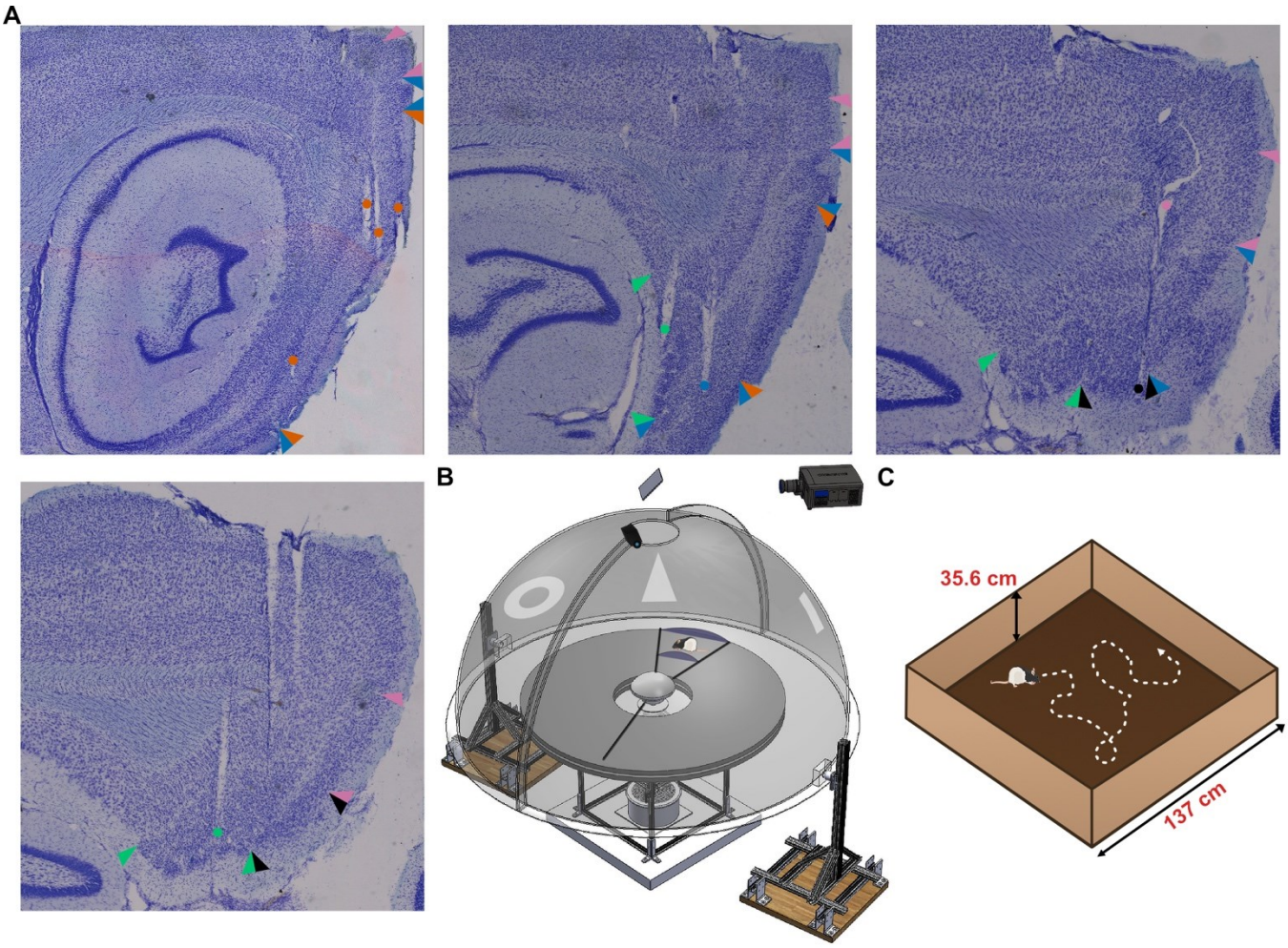


**Fig. 1.** Nissl-stained sagittal sections showing tetrode recording sites across parahippocampal regions in one rat and schematics of the Dome and open arena recording environments.
**(A)** Four representative sections, arranged from lateral-most (top left) to medial-most (bottom left), from Rat 1061. Colored arrowheads demarcate the superficial borders of parahippocampal regions: area 29e (black), MEC (orange), PA (blue), PO (pink) and PR (green). Dots indicate example recording locations in these regions. This color scheme is used throughout all figures.
**(B)** Schematic of the Dome virtual-reality apparatus (*29*). A large opaque hemispherical shell (rendered semi-transparent to visualize the interior) displayed three visual landmarks (annulus, triangle, and rectangle) as a seamless wrap-around scene. Inside, the rat ran circular laps around the perimeter of a table. A rotating central pillar carried three radial boom arms: a front arm with a reward spout, a back arm that guides the recording tether, and a cleaning arm (hardware not shown). An enclosure of short clear walls affixed to the feeding and tether booms surrounded, and moved with, the animal to keep it radially centered throughout the session. An overhead camera viewed the annular track through the top aperture for real-time behavior tracking. Components that could otherwise provide angular cues either co-rotated with the animal or were circularly symmetric, making the projected landmarks the dominant polarizing cues.
**(C)** Schematic of open arena apparatus. A 137 cm square arena enclosed by 35.6 cm-high walls was used during free exploration to identify functional parahippocampal cell types. The arena was placed on the floor in a room with multiple distal visual cues (not shown), providing stable landmarks outside the apparatus. Drawings of rats in B and C by E. Ackermann, adapted from https://github.com/kemerelab/ratpack/ under a Creative Commons license CC BY-SA 4.0.

## Area 29e spatial tuning is more tightly bound to visual landmarks than neighboring parahippocampal areas

We performed simultaneous tetrode recordings in area 29e (Fig. 1A and fig. S1) and four other parahippocampal areas (MEC, PA, PR, and postrhinal cortex [PO]), as rats (n = 5) navigated freely in two environments: a virtual-reality apparatus that allowed for precise control of the visual landmarks' locations and saliency during untethered physical locomotion (*12*, *29*) (Fig. 1B) and a square open-field arena (Fig.

1C). When the landmarks were stationary, a comparable proportion of 29e neurons displayed significant spatial information as in the other parahippocampal regions (29e: 70/78, MEC: 257/328, PA: 178/232, PO: 87/112, PR: 32/44; chi-squared test $\chi^2$ (4,796) = 7.64, p = 0.105). Many spatially tuned 29e neurons increased or decreased their firing rates selectively at locations adjacent to each landmark (Fig. 2A). We defined two metrics to quantify the strength and between-landmark consistency of such peri-landmark firing-rate changes: (1) the *z-index* was computed as the mean absolute difference between z-scored firing rates at track locations closest to landmarks and those midway between landmarks and (2) the *local similarity index* was computed as the mean pairwise correlation between spatial firing-rate profiles taken from a local window centered on each landmark. Both metrics were significantly larger in 29e spatially tuned neurons than those from other regions (Fig. 2B).

Considering this overrepresentation of locations near landmarks among spatially tuned 29e neurons, we next tested the extent to which their firing fields were dynamically controlled by landmarks when the entire landmark constellation was rotated around the track in a behaviorally closed-loop fashion. The rotation of landmarks was controlled by an experiment gain (G) that set the ratio between the rat's travel distance in the landmark frame of reference to the travel distance in the laboratory frame of reference (*12*). When G < 1, the landmark array was rotated around the center of the track in the same direction as the rat, providing the rat with the illusion that it was moving slower than it really was; when G > 1, it was rotated in the opposite direction, providing the rat with the illusion that it was moving faster than it really was (Fig. 2C). In each session, the value of G was initialized at 1 (corresponding to stationary landmarks), gradually ramped to its final value, and then held constant for the remainder of the session.

Under these manipulations, spatially tuned neurons across all regions often maintained stable firing fields in the rotating landmark frame of reference across laps—a manifestation of landmark control (Fig. 2D and fig. S2A for example sessions). This lap-to-lap stability, however, was disrupted in some sessions, typically during the gain-ramp epoch and persisting until the end of the experiment (Fig. 2E and fig. S2B for example sessions). To quantify the lap-to-lap stability of each neuron's firing fields in the rotating landmark frame of reference, we defined a landmark-locking score based on the spatial autocorrelogram (up to a 10-lap lag) of the neuron's activity during the last 12 laps (see Methods). A landmark-locking score close to 1 indicates highly stable lap-to-lap firing of a neuron in the landmark frame (e.g., Fig. 2D bottom inset), while a score near 0 indicates loss of this stability (e.g., Fig. 2E bottom inset). Averaging landmark-locking scores across all spatially tuned neurons in each session (number of neurons recorded per session mean ± s.d. = 33.0 ± 17.2) revealed a bimodal distribution (Fig. 2F). An unsupervised clustering algorithm identified two clusters within this distribution. We refer to the cluster of sessions with higher landmark-locking scores (mean ± s.e.m. = 0.68 ± 0.02; n = 13 sessions) as *LM-control* sessions, indicating reliable control of the landmarks over spatially tuned neurons (as in Fig. 2D). By contrast, the remaining cluster of sessions with lower landmark-locking scores (0.27 ± 0.02; n = 21 sessions) are termed *LM-failure* sessions (*31*), indicating the failure of landmark control over spatially tuned neurons (as in Fig. 2E). *LM-failure* sessions were observed predominantly when the experimental gain reached more extreme values in a session (i.e., much higher or lower than 1; fig. S3A), having induced large conflicts between the path integration and visual landmark-inferred position estimates.

Area 29e neurons showed greater control by the landmarks than the other parahippocampal regions. In *LM-control sessions*, landmark-locking scores of spatially tuned neurons were strongly skewed towards 1 in all regions (Fig. 2G, left). In *LM-failure sessions*, however, landmark-locking scores of spatially tuned neurons in MEC, PA, PO, and PR were skewed towards 0, while those in 29e remained skewed toward 1, indicating greater anchoring to landmarks in 29e than in the other regions (Fig. 2G, right). To ensure these regional differences were not due to session-specific effects or non-uniform sampling, we compared mean landmark-locking scores between simultaneously recorded neurons from 29e and other regions, which confirmed our findings (Fig. 2H). Specifically, in LM-control sessions (n = 7), mean landmark-locking scores did not significantly differ between 29e (mean ± s.e.m. = 0.62 ± 0.04) and other regions (0.66 ± 0.02), whereas in *LM-failure sessions* (n = 8), 29e (0.56 ± 0.05) showed significantly higher mean landmark-locking score than other regions (0.21 ± 0.03). This selective anchoring of 29e neurons to landmarks—but not neurons from other regions—persisted even when landmark rotation was independent of the rat's movement, including when the animal was stationary and the landmarks moved past (fig. S4).

Collectively, these data suggest that, compared to neighboring parahippocampal regions specialized for spatial processing with greater reliance on path integration, area 29e may be more specialized as a visuospatial region that codes for landmark-based spatial representations.

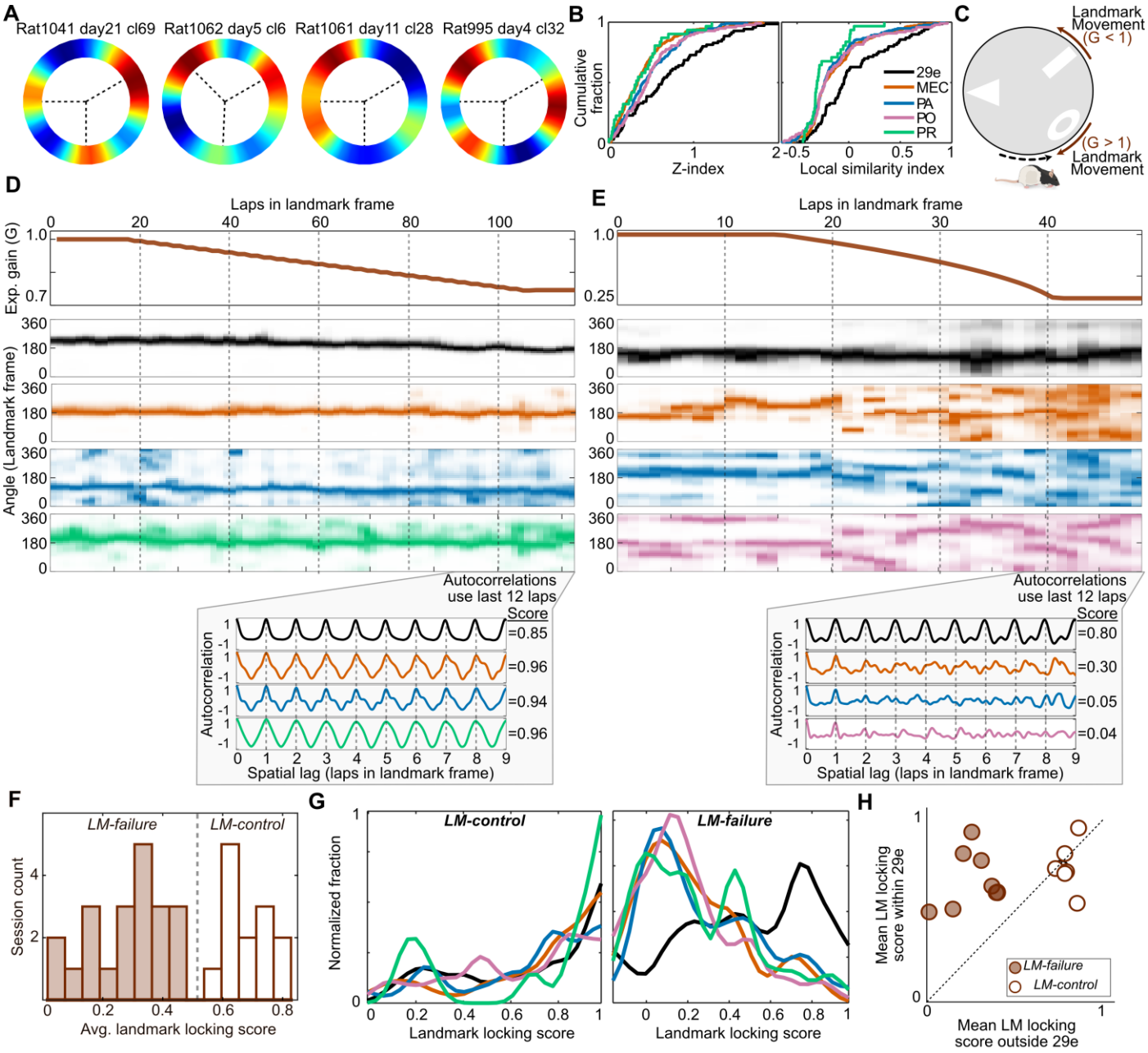


**Fig. 2.** Landmark-anchored spatial tuning in 29e compared to spatial tuning in neighboring parahippocampal regions (MEC, PA, PO, and PR) that are more reliant on path integration.

**(A)** Examples of circular rate maps of four spatially tuned 29e neurons, with red indicating higher and blue indicating lower firing rates. Above each map, rat ID, day number, and the neuron's identification number are shown. Dashed lines mark the angular positions of the centers of the three landmarks projected onto the Dome. The first two examples show neurons that increase firing near landmarks, while the last two show neurons that decrease firing near landmarks.

**(B)** Cumulative distributions of z-index (left) and local-similarity index (right), which quantify the strength and uniformity of landmark selective firing, respectively. The z-index was significantly larger in 29e than other regions (29e median [IQR]: 0.60 [0.24, 1.02], MEC = 0.33 [0.16, 0.54], PA = 0.40 [0.22, 0.72], PO = 0.44 [0.21, 0.60], PR = 0.33 [0.14, 0.54]; Kruskal-Wallis test $\chi^2(4) = 22.2$, $p < 0.001$; post-hoc Wilcoxon rank-sum tests with Holm-Bonferroni correction 29e vs. MEC: $Z = 4.18$, $p < 0.001$; 29e vs. PA: $Z = 2.70$, $p = 0.013$; 29e vs. PO: $Z = 2.38$, $p = 0.017$; 29e vs. PR: $Z = 2.87$, $p = 0.012$). The local-similarity index was also larger in 29e than other regions (29e median [IQR]: 0.05 [–0.24, 0.28], MEC = –0.23 [–0.31, 0.00], PA = –0.23 [–0.32, –0.02], PO = –0.23 [–0.30, –0.01], PR = –0.30 [–0.33, –0.06]; Kruskal-Wallis test $\chi^2(4) = 22.3$, $p < 0.001$; post-hoc Wilcoxon rank-sum tests with Holm-Bonferroni correction 29e vs. MEC: $Z = 3.68$, $p < 0.001$; 29e vs. PA: $Z = 4.06$, $p < 0.001$; 29e vs. PO: $Z = 3.14$, $p < 0.001$; 29e vs. PR: $Z = 3.75$, $p < 0.001$).

**(C)** Illustration of experimental gain manipulation. Visual landmarks inside the Dome were moved as a function of the rat's movement, controlled by the experiment gain (G), defined as the ratio of the rat's movement in the landmark frame to its movement in the lab frame. Drawing of rat adapted from https://github.com/kemerelab/ratpack/ (E. Ackermann) under a Creative

Commons license CC BY-SA 4.0.
**(D)** Representative closed-loop gain manipulation session. The top row shows the experimental gain as a function of laps in the landmark frame (x-axis). The session began with a gain of 1 (i.e., stationary landmarks). The gain was then gradually ramped up to its target value, during which the landmark array rotated at increasing speeds opposite to the animal's movement direction. The final gain was then held constant for the duration of the session. The bottom row shows the lap-to-lap (with respect to landmarks) firing rate as a function of the animal's angle in the landmark frame (y-axis) from example neurons, color-coded by region (as in panel B). The intensities were normalized to the maximum firing rate of the given neuron. In this session, the firing locations of all spatially tuned neurons remained anchored to rotating landmarks. Inset shows the spatial autocorrelogram of each representative neuron's activity in the rotating landmark frame, calculated using the last 12 laps for lags from 0 to 10 laps. Note the lap-to-lap periodicity in the autocorrelation traces for these neurons, whose firing remained anchored to landmarks.
**(E)** Same format as (D). Representative session where most spatially tuned neurons—except in 29e—lost their anchoring during the gain ramp. After about lap 20, the firing fields of the MEC (orange), PA (blue), and PO (pink) neurons became increasingly diffuse. The 29e neuron (black), by contrast, maintained stable landmark-relative firing throughout the session. Insets show the spatial autocorrelogram of each neuron's activity in the rotating landmark frame, calculated using the last 12 laps for lags from 0 to 10 laps. Note that the lap-to-lap periodicity in the autocorrelation traces (inset) for the neurons that lost landmark anchoring showed disrupted autocorrelation structures: either no clear periodicity (e.g., the orange neuron), or a non-unity periodicity (e.g., the blue and pink neurons), reflecting the continued firing of the neuron at repeated intervals different than a single lap.
**(F)** Session-level bimodality of neuronal populations' average landmark-locking scores. Sessions were classified as *LM-failure* (shaded bars) *or LM-control* (unshaded bars).
**(G)** Distributions of landmark-locking scores for individual spatially tuned neurons. *LM-control sessions* (left) show statistically comparable landmark-locking scores across all regions (median [IQR]: 29e = 0.73 [0.39, 0.90], MEC = 0.81 [0.52, 0.92], PA = 0.76 [0.46, 0.88], PO = 0.66 [0.39, 0.85], PR = 0.89 [0.23, 0.97]; Kruskal-Wallis test $\chi^2(4) = 4.2$, $p = 0.376$). By contrast, *LM-failure sessions* (right) show significantly larger scores in 29e than other regions (median [IQR]: 29e = 0.50 [0.25, 0.77], MEC = 0.19 [0.06, 0.41], PA = 0.22 [0.07, 0.50], PO = 0.15 [0.03, 0.34], PR = 0.20 [0.04, 0.44]; Kruskal-Wallis test $\chi^2(4) = 31.4$, $p < 0.001$; post-hoc Wilcoxon rank-sum tests with Holm-Bonferroni correction 29e vs. MEC: $Z = 5.13$, $p < 0.001$; 29e vs. PA: $Z = 4.11$, $p < 0.001$; 29e vs. PO: $Z = 4.74$, $p < 0.001$; 29e vs. PR: $Z = 3.08$, $p < 0.001$).
**(H)** Mean landmark-locking score of spatially tuned 29e neurons within a session (y axis) and their simultaneously recorded counterparts in other regions (x axis) within the same session. In *LM-control sessions (*unfilled circles), the normalized difference between scores of neurons inside 29e vs. outside 29e (i.e., (inside – outside)/(inside + outside)) was not significantly different than zero (one-sample t-test $t(6) = 0.964$, $p = 0.372$), whereas in *LM-failure* sessions (filled circles), the normalized difference was significantly positive (one-sample t-test $t(7) = 6.93$, $p < 0.001$), indicating greater anchoring to landmarks in 29e than in other regions.

## Area 29e is sensitive to sensory aspects of visual landmarks

We next investigated the sensitivity of area 29e to sensory aspects of the landmarks in comparison to neighboring parahippocampal areas. Following the closed-loop gain manipulations, visual landmarks were removed, causing rapid changes in unsorted, multi-unit firing rates across all regions (Fig. 3A). We calculated a landmark-removal response score, which quantifies the magnitude (increase or decrease) of such changes during the 375 ms immediately following landmark removal compared to the 375 ms immediately preceding it (see Methods). A score close to 1 indicates the occurrence of a large, statistically unlikely firing-rate change (increase or decrease) after landmark removal, while a score near 0 indicates little to no change. On average, landmark-removal response scores were highest in tetrodes located in 29e (Fig. 3B). However, these differences were statistically significant only when comparing 29e to MEC and PA.

To determine whether these greater changes in 29e multi-unit activity were related to tuning of its single neurons to the luminance or contrast of the landmarks, we performed additional experiments in a subset of animals (n = 2), recording from 29e, MEC, and PR (no tetrodes were in PA or PO in these animals). As rats ran laps, we pseudo-randomly varied landmark and background luminance between two levels (i.e., high or low) across six-lap blocks, with the experimental gain fixed at 1 to keep landmark locations stationary (Fig. 3C). Similar proportions of neurons with significant luminance sensitivity were identified across all recorded regions (29e: 28/45; MEC: 14/24; PR: 9/25; chi-squared test $\chi^2(2,94) = 4.66$, p = 0.096). However, the magnitude of luminance sensitivity was significantly larger in neurons from 29e than those from MEC and PR (Fig. 3D). This heightened effect of landmark and background luminance on 29e single-neuron activity may reflect their tuning to the contrast between the landmark and background luminance or to total luminance. For each neuron with significant luminance sensitivity, we fit a linear model to the peak firing rates on each lap, using landmark contrast and total luminance as predictors. Two-way ANOVA (region x predictor) on the partial $R^2$ values—which quantify the firing-rate variance uniquely explained by each predictor—revealed particularly pronounced tuning of 29e neurons to landmark contrast, the strength of

which significantly exceeded not only contrast tuning in other regions but also total luminance tuning in any region (Fig. 3E).

Following the luminance-change epochs, we performed closed-loop gain manipulations with sufficiently large gains to induce landmark-control failure. In spatially tuned neurons of 29e, there was a positive but marginally significant relationship (Fig. 3F) between the strength of landmark-contrast tuning and the degree of landmark-anchored firing. No relationship was observed in other regions (fig. S5A). A multiple regression model including region identity, landmark-locking score, and their interaction confirmed that the positive relationship between contrast tuning and landmark anchoring was specific to area 29e (slope in 29e: $\beta = 0.43$, $t(69) = 3.1$, $p = 0.002$; interaction term: $\beta = -0.29$, $t(69) = -2.05$, $p = 0.043$).

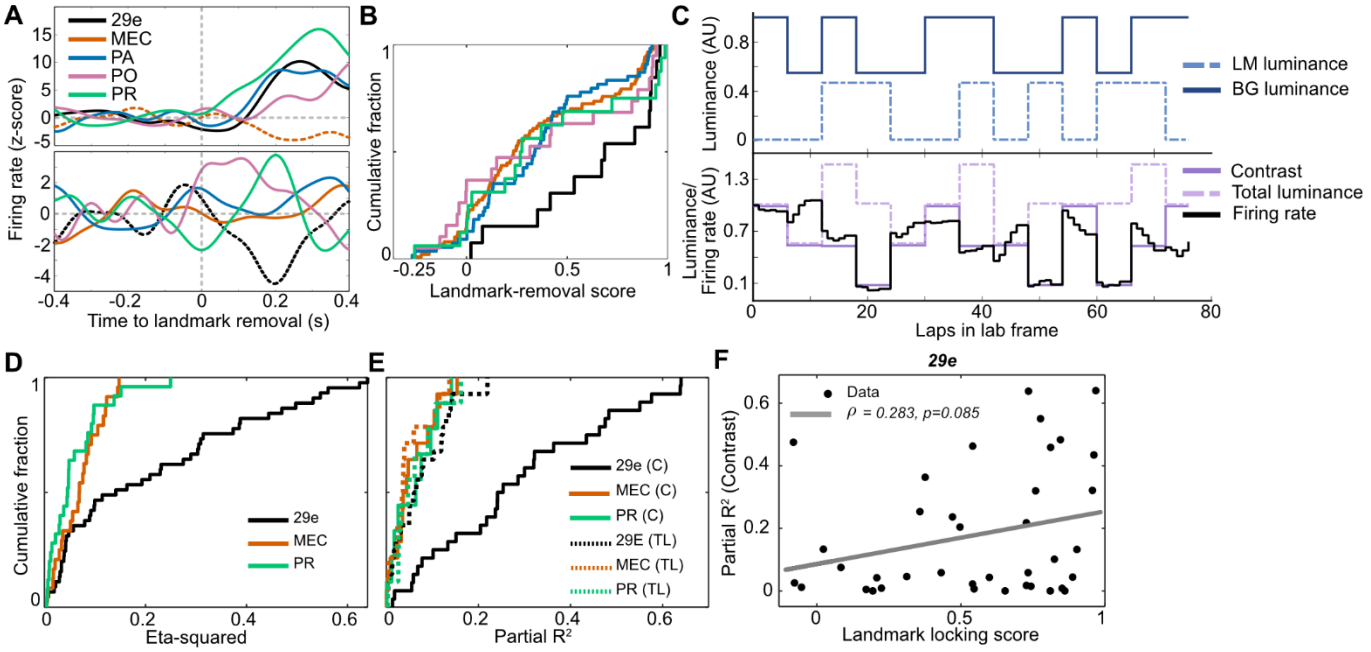


**Fig. 3.** Greater sensitivity of area 29e to sensory aspects of visual landmarks compared to neighboring parahippocampal areas.
**(A)** Example multi-unit firing-rate traces aligned to visual landmark removal, showing the largest change (top) and the median change (bottom) per region.
**(B)** Cumulative distributions of landmark-removal response scores from unique tetrode locations (29e: n = 13, MEC: n = 87, PA: n = 54, PO: n = 19, PR: n = 16; colors as in Panel A). Response scores of tetrodes in 29e were significantly higher than those in MEC and PA, but not PO and PR (median [IQR] 29e = 0.68 [0.40, 0.91], MEC = 0.23 [0.03, 0.67], PA = 0.33 [0.10, 0.50], PO = 0.31 [-0.02, 0.84], PR = 0.27 [0.01, 0.83]); Kruskal-Wallis test $\chi^2(4) = 8.58$, $p < 0.001$; post-hoc Wilcoxon rank-sum tests with Holm-Bonferroni correction 29e vs. MEC: $Z = 2.84$, $p = 0.017$; 29e vs. PA: $Z = 2.67$, $p = 0.022$; 29e vs. PO: $Z = 1.88$, $p = 0.120$; 29e vs. PR: $Z = 1.38$, $p = 0.167$).
**(C)** Protocol for luminance manipulation experiments and an example of a contrast-responsive neuron. Top: Experiment design. Bottom: Example neuron from area 29e showing peak lapwise firing rate changes (black) that more closely followed changes in landmark contrast (C = LM - BG, solid purple) rather than total luminance (TL = LM + BG, dashed purple). Firing rates are normalized to the neuron's peak firing rate in the first lap of the session.
**(D)** Region-wise cumulative distributions of total eta-squared values from two-way ANOVA with background and landmark luminance as factors. Total eta-squared was significantly larger in 29e neurons than in MEC and PR neurons (median [IQR] 29e = 0.14 [0.04, 0.32], MEC = 0.06 [0.03, 0.09], PR = 0.04 [0.01, 0.08]; Kruskal-Wallis test $\chi^2(2) = 13.95$, $p < 0.001$; post-hoc Wilcoxon rank-sum tests with Holm-Bonferroni correction 29e vs. MEC: $Z = 2.61$, $p = 0.008$; 29e vs. PR: $Z = 3.30$, $p = 0.001$).
**(E)** Cumulative distributions of partial $R^2$ values from linear models predicting neurons' lapwise peak firing rates using landmark contrast (C, solid lines) and total brightness (TL, dashed lines) as predictors. Two-way ANOVA revealed significant main effects of region ($F(2,96) = 16.0$, $p < 0.001$) and predictor type ($F(1,96) = 8.6$, $p = 0.004$), as well as a significant interaction ($F(2,96) = 10.8$, $p < 0.001$). Post-hoc tests (with Holm-Bonferroni corrections) showed that partial $R^2$ for landmark contrast in 29e (mean ± s.e.m. = 0.28 ± 0.03) was significantly greater than landmark-contrast partial $R^2$ in MEC (0.05 ± 0.01) and PR (0.06 ± 0.01), and total-brightness partial $R^2$ in all recorded regions (29e: 0.07 ± 0.01; MEC: 0.04 ± 0.01; PR: 0.06 ± 0.01); all pairwise comparisons with landmark contrast in 29e: $p < 0.001$.
**(F)** There was a positive but non-significant relationship between the partial $R^2$ (y-axis) for landmark-contrast tuning of spatially tuned 29e neurons and their landmark-locking scores (x-axis). Each dot corresponds to one neuron. The Pearson correlation coefficient and its significance are reported.

**Area 29e demonstrates tuning to egocentric and allocentric head direction, with egocentric tuning more closely associated with sensory-like responses to landmarks**

To further characterize spatial tuning in 29e in comparison to neighboring parahippocampal areas, we analyzed single-unit activity obtained as the rats (n = 5) foraged in an open arena after they completed each Dome session. The arena was in a separate room from the Dome. We computed Skaggs' spatial information (SI) scores (*32*) from each neuron's 2D positional rate map and Rayleigh scores from its head-direction (HD) tuning curve (*33*, *34*) as traditional measures of allocentric place and HD tuning (Fig. 4A, fig. S6A). Spatial information scores were not significantly different across regions (Fig. 4B, top). In contrast, 29e had significantly higher Rayleigh scores than MEC, PA, and PO, but not PR (Fig. 4B, bottom), showing that 29e neurons were more selective for head direction than spatial location, compared to neighboring regions. Because behavioral correlations between position and HD can lead to a bias in values of independently calculated SI and Rayleigh scores (*35*, *36*), we also used a generalized linear model (GLM), jointly estimating each neuron's place and HD tuning (fig. S6B-C). GLM-based analysis confirmed significantly higher Rayleigh scores in 29e compared to MEC, PA, and PO but not PR. Place tuning from the GLM, however, showed a different trend compared to the original result: SI scores were significantly lower in 29e than MEC, PA, and PO but not PR.

Classic, allocentric HD cells fire maximally in a consistent direction regardless of the animal's location, yielding parallel preferred HD vectors across the arena (*36*, *37*)(fig. S7A). Many 29e neurons, however, exhibited progressive, location-dependent shifts in their preferred HD, forming vector fields with rotational, radial (outward/inward-pointing), or hybrid patterns—consistent with egocentric HD coding (Fig. 4C and fig. S7B; see fig. S7C for examples from other regions). To quantify egocentric tuning, we developed an egocentric vector-field (EVF) score that measures the consistency of rotational and radial egocentric patterns within a neuron's HD vector field across the arena (see fig. S8 and Methods). The EVF score quantifies a neuron's egocentric tuning strength between 0 (no egocentric tuning such as when HD vectors are randomly distributed or parallel everywhere) to 1 (strongest egocentric tuning). Across all neurons, the EVF scores had significantly higher values in 29e than other regions (Fig. 4D).

We used a combination of EVF, Rayleigh, and SI scores to determine the spatial tuning class of each neuron. First, each neuron's EVF score was compared to two null models: a temporal null (shuffling spike times relative to behavior, disrupting all tuning) and a spatial null (shuffling HD vector locations, disrupting the location x preferred HD relation underlying the egocentric patterns while preserving overall allocentric tuning; see Methods). Neurons with significant EVF scores under both nulls and stable tuning throughout the session were classified as egocentric HD-tuned. Neurons not meeting these criteria were tested for allocentric HD tuning, using a Rayleigh score-based shuffle and stability of HD tuning; those failing both HD tests were classified as nondirectional and screened for allocentric place tuning (see Methods). Neurons that passed significance tests for both egocentric and allocentric tuning were classified as egocentric, as in 95% of the cases (116/122) an egocentric-based GLM outperformed an allocentric GLM in terms of a lower BIC score. None of the results below were changed when the remaining six neurons were re-labeled as allocentric HD-tuned.

The classification revealed significant regional differences in the prevalence of spatial tuning types (chi-squared test $\chi^2(12,996) = 110.34$, $p < 0.001$). Egocentric HD-tuned neurons were significantly more prevalent in 29e (47/115, 40.8%) than in MEC (39/418, 9.3%), PA (54/294, 18.3), PO (18/92, 19.5%), and PR (16/77, 20.7%) (post-hoc Fisher's exact test with Holm-Bonferroni correction, 29e vs. MEC, PA: $p < 0.001$, 29e vs. PO $p = 0.002$, 29e vs. PR $p = 0.018$). Nondirectional place-tuned neurons were rare in 29e (1/115, 0.8%), at a proportion significantly lower than in MEC (67/418, 17.2%; post-hoc test $p < 0.001$) and PA (43/294, 14.6%; $p < 0.001$), but not PO (3/92, 3.2%; $p = 0.650$) or PR (4/88, 4.5%; $p = 0.563$). The prevalence of allocentric HD-tuned neurons was similar across regions (ranging from 40 to 51%; all post-hoc pairwise $p > 0.400$).

Because visual sensory cues are initially encoded in egocentric (head- and retina-centric) frames before being converted to an allocentric frame in some higher-order areas, we hypothesized that egocentric HD-tuned neurons would be more closely associated with encoding visual landmarks than allocentric ones. Indeed, egocentric neurons of 29e exhibited higher landmark-locking scores (Fig. 4E) and a higher prevalence of contrast sensitivity (Fig. 4F) in the Dome; no significant differences were found in other regions (fig. S9A). The positive relationships between egocentric tuning and landmark anchoring were

specific to area 29e, compared to other regions (multiple regression analysis for landmark anchoring: egocentric vs. allocentric: $\beta = 0.37$, $t(297) = 2.82$, $p = 0.005$; interaction term: $\beta = -0.53$, $t(297) = -2.18$, $p = 0.029$).

We hypothesized that egocentric 29e neurons would be anchored to locations outside the open arena, where salient landmarks were located. To test this prediction, we computed for each egocentric neuron the shortest signed distance from the arena boundary to its optimal anchor point estimated by maximizing the negative log-likelihood of a GLM. A negative distance indicates an anchor point inside the arena, while a positive distance indicates one outside. Median signed distance was significantly positive in 29e (median [IQR] = 68 [–12, 307] cm; Wilcoxon's signed-rank test: $p < 0.001$). By contrast, the medians were negative in other regions (MEC = –27 [–47, –12], $p < 0.001$; PA = –13 [–28, 7], $p = 0.056$; PO = –21 [–39, 28], p = 0.445; PR = –17.3 [–44, 66], p = 0.947), with only MEC being statistically significant. Cross-regional comparison of signed distance distributions confirmed that anchoring to locations outside the arena is a distinguishing feature of egocentric neurons in 29e (Fig. 4G).

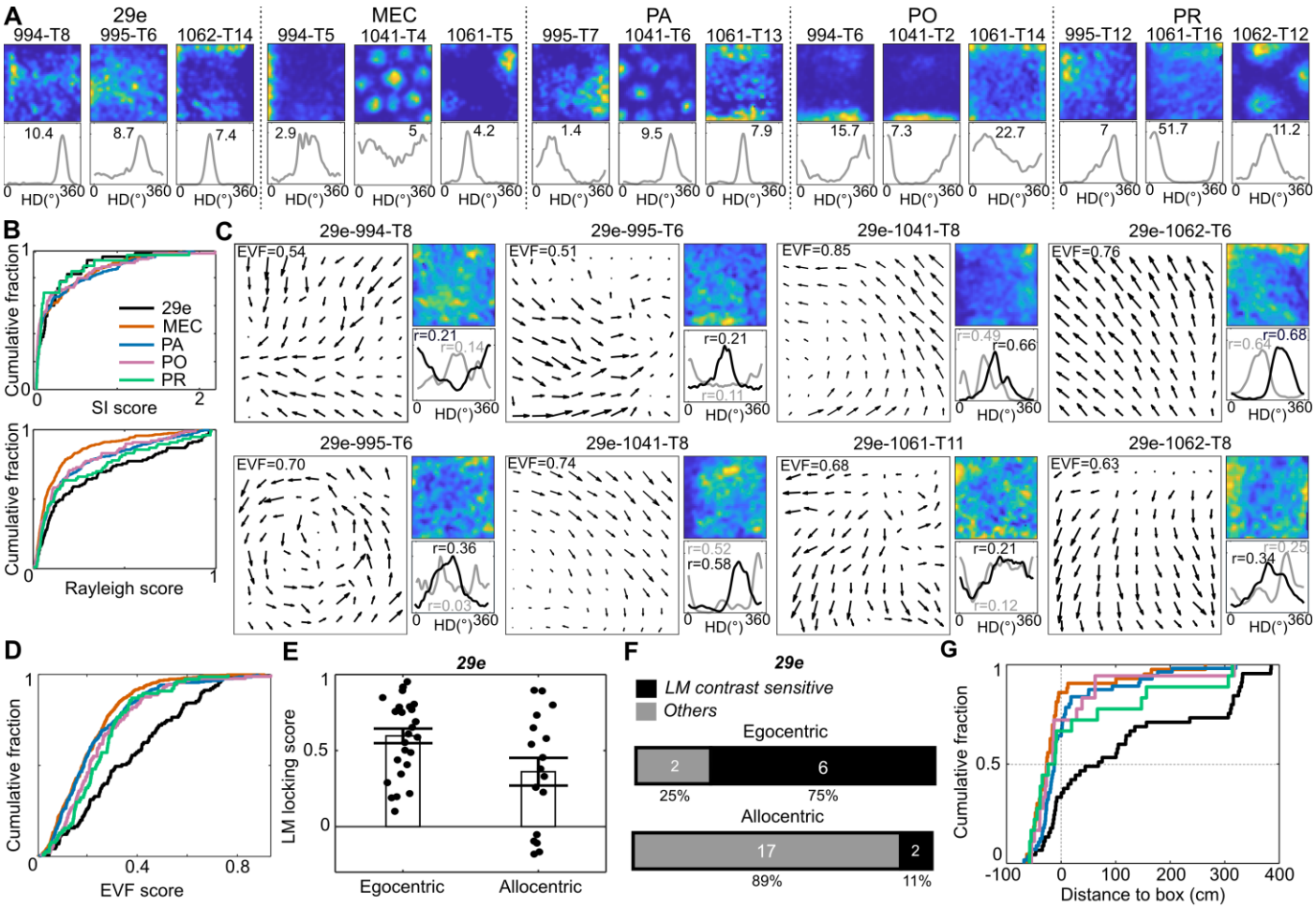


**Fig. 4.** Two-dimensional spatial representations of Area 29e neurons compared to neurons in neighboring parahippocampal regions (MEC, PA, PO, and PR).

**(A)** Allocentric tuning of three example neurons from each region. For each neuron, a 2D positional rate map (top) and a 1D allocentric head-direction (HD) tuning curve (bottom) are shown. Rat ID and tetrode number for each neuron are indicated above its rate map. The number inset in each HD plot denotes the peak-firing rate for head-direction tuning. The y-axis of each HD plot starts at zero.

**(B)** Cumulative distributions of SI score (top) and Rayleigh score (bottom). SI scores were not significantly different across regions (29e median [IQR] = 0.12 [0.04, 0.30], MEC = 0.10 [0.03, 0.47], PA = 0.09 [0.04, 0.48], PO = 0.07 [0.02, 0.48], PR = 0.08 [0.04, 0.30]; Kruskal-Wallis test $\chi^2(4) = 2.32$, $p = 0.675$). Rayleigh scores differed significantly across regions (Kruskal-Wallis test $\chi^2(4) = 40.9$, $p < 0.001$). Specifically, 29e (median [IQR] = 0.16 [0.06, 0.48]) exhibited significantly larger scores than MEC (0.06 [0.03, 0.15]), PA (0.10 [0.04, 0.27]), and PO (0.09 [0.04, 0.27]), but not PR (0.11 [0.04, 0.40]); post-hoc Wilcoxon rank-sum test with Holm-Bonferroni correction 29e vs. MEC: $Z = 5.6$, $p < 0.001$; 29e vs. PA: $Z = 2.8$, $p = 0.017$; 29e vs. PO: $Z = 2.5$, $p = 0.023$; 29e vs. PR: $Z = 1.4$, $p = 0.171$.

**(C)** Egocentric tuning of example 29e neurons. For each neuron, the left panel shows the HD vector field, with the EVF score indicated. Arrow direction depicts the neuron's preferred HD within a 15 × 15 cm positional bin centered at the arrow base; arrow size represents the product of the neuron's total firing rate (summed across head-direction bins) and its mean resultant length (MRL) inside the same positional bin. At right, the top panel shows the allocentric 2D positional rate map and the bottom panel

shows HD tuning curves in allocentric (gray) and egocentric (black) frames. Numbers in the HD plots denote the mean resultant length (r) of tuning in each frame.
**(D)** Cumulative distributions of EVF scores across regions (color-coded as in panel B). Significant regional differences were found (Kruskal-Wallis test $\chi^2(4) = 55.4$, $p < 0.001$): Neurons in 29e (median [IQR] = 0.35 [0.20, 0.52]) had significantly larger EVF score than in MEC (0.20 [0.12, 0.28]), PA (0.20 [0.12, 0.34]), PO (0.25 [0.16, 0.39]), and PR (0.23 [0.14, 0.35); post-hoc Wilcoxon rank-sum test with Holm-Bonferroni correction 29e vs. MEC: $Z = 7.1$, $p < 0.001$; 29e vs. PA: $Z = 5.6$, $p < 0.001$; 29e vs. PO: $Z = 2.9$, $p = 0.003$; 29e vs. PR: $Z = 3.81$, $p < 0.001$.
**(E)** Significant difference in the landmark-locking scores between 29e egocentric and allocentric neurons (represented as dots) during *LM-failure* sessions in the Dome. Bars show population means (egocentric: 0.60; allocentric: 0.36), and error bars indicate s.e.m. t-test egocentric vs. allocentric: $t(42) = 2.5$, $p = 0.016$.
**(F)** Significant difference in the prevalence of significant contrast sensitivity between egocentric and allocentric 29e neurons (Fisher's exact test $p = 0.0019$). Numbers inside the bars show the count and percentage of neurons in each category.
**(G)** Cumulative distributions of the signed distances from the estimated anchor points of egocentric neurons to the open-arena border. The signed distance was significantly larger in 29e than other regions (Kruskal-Wallis test $\chi^2(4) = 32.1$, $p < 0.001$; post-hoc Wilcoxon rank-sum test with Holm-Bonferroni correction 29e vs. MEC: $Z = 5.1$, $p < 0.001$; 29e vs. PA: $Z = 3.8$, $p < 0.001$; 29e vs. PO: $Z = 3.2$, $p = 0.002$; 29e vs. PR: $Z = 2.5$, $p = 0.011$).

## Area 29E differs from neighboring parahippocampal regions in theta and gamma modulation

Having demonstrated differences between 29e and the other regions in the strength of landmark anchoring and responses to changes in visual input, we next explored physiological characteristics that might underlie the network mechanisms governing the interaction among these regions. Area 29e differed from the other regions in both its local field potential (LFP; Fig. 5A) properties and its spike-LFP coupling. All regions showed significant LFP oscillatory power in the theta (6–10 Hz), theta harmonic (12–30 Hz), and gamma bands (50–120 Hz) (Fig. 5B). Area 29e had the lowest theta power (mean ± s.e.m. = 0.687 ± 0.072), which was significantly different than MEC (1.148 ± 0.028), PA (1.036 ± 0.043), and PO (1.365 ± 0.058), but not PR (0.735 ± 0.056) (fig. S10A). Gamma-band power did not show significant differences across regions (fig. S10B). To account for non-independence among LFP signals recorded within animals and brain regions, a linear mixed-effects model with two random intercepts—rat identity and region identity within each rat—yielded the same conclusions (fig. S10).

These regional differences in LFP were matched at the level of single-neuron firing properties. Single neuron mean firing rates in the Dome were lowest in 29e compared to the other regions (fig. S10C), although the difference was statistically significant only relative to MEC, PA and PR. Theta rhythmicity (*38–41*) in the neurons' spike autocorrelograms was significantly weaker in 29e than the other regions (Fig. 5C-D). In contrast, gamma-band rhythmicity was significantly higher in 29e (Fig. 5E). Spike coupling to LFP theta oscillations—quantified by the pairwise phase consistency of the spike-phase distribution (*42*)—was significantly lower in 29e than other recorded regions (Fig. 5F). We hypothesized that more strongly theta-modulated neurons in 29e would be more weakly anchored to landmarks, functionally resembling the weaker landmark anchoring we observed in MEC, PA, PO, and PR. Indeed, landmark-locking scores of spatially tuned 29e neurons were negatively correlated with the strength of their spike-phase coupling to LFP theta oscillations (Fig. 5G), whereas no significant correlation was observed in any other region (fig. S2). We also found a statistically significant, negative relationship between landmark-contrast tuning strength and spike-LFP theta phase coupling in 29e (Fig. 5H). No significant relationship was observed in MEC and PR, although the difference between 29e and MEC and PR was only marginally significant (fig. S5B). Finally, egocentric neurons of 29e had significantly lower theta PPC than allocentric neurons (Fig. 5I). The same pattern was also observed in other regions, reaching statistical significance in MEC and PA, and approaching significance in PO and PR (fig. S9B). These results demonstrate that neurons with more sensory-driven properties prevalent in 29e (landmark locking and egocentric tuning) were less strongly coupled to the dominant theta rhythm in the parahippocampal system.

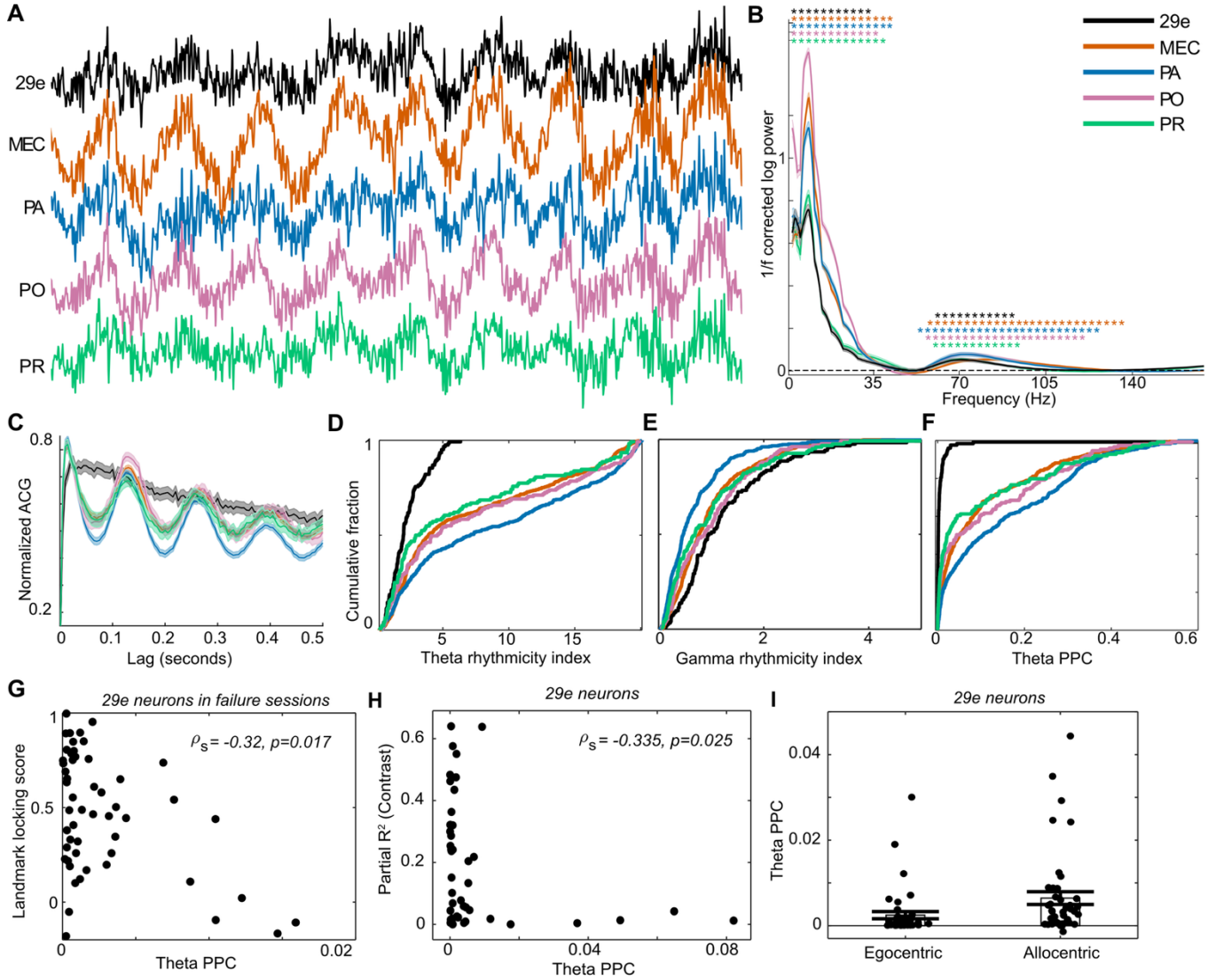


**Fig. 5.** Physiological differences between area 29e and neighboring parahippocampal areas (MEC, PA, PO, and PR).
**(A)** Representative LFP traces, simultaneously recorded from 29e, MEC, PA, PO, and PR.
**(B)** Mean ± 2 × s.e.m. log-power spectral density (PSD) of LFPs in all recorded regions (unique recording locations for 29e: n = 20, MEC: n = 104, PA: n = 64, PO: n =22, PR: n = 24). PSDs are computed after correcting the aperiodic 1/f background in the LFP recordings. Asterisk marks the statistical significance of the power at a particular frequency, as measured by a cluster permutation test to control familywise error rate at α = 0.05 (*43*).
**(C)** Population mean ± s.e.m. of the normalized spike autocorrelograms (ACGs) across single neurons in each region (colors as in panel B). Area 29e shows a monotonic, non-oscillatory decay, whereas other regions exhibit prominent oscillations at the theta frequency.
**(D-F)** Cumulative distributions of single-neuron physiological measures across recorded regions (area 29e: n = 123, MEC: n = 566, PA: n = 414, PO: n = 133, PR: n = 124). *Panel D* shows significantly lower theta rhythmicity of spike ACGs in 29e (median [IQR] = 2.01 [1.29, 2.89]) than other regions (MEC = 3.91 [2.06, 12.4], PA = 7.08 [2.35, 15.53], PO = 4.67 [1.79, 13.19], and PR = 3.08 [1.44, 10.29]; Kruskal-Wallis test $\chi^2(4) = 100.4$, $p < 0.001$; post-hoc Wilcoxon rank-sum tests with Holm-Bonferroni correction 29e vs. MEC: $Z = -8.1$, $p < 0.001$; 29e vs. PA: $Z = -9.4$, $p < 0.001$; 29e vs. PO: $Z = -6.2$, $p < 0.001$; 29e vs. PR: $Z = -4.1$, $p < 0.001$). *Panel E* shows significantly larger gamma rhythmicity in 29e (median [IQR] = 0.95 [0.63, 1.69]) than other regions (MEC = 0.76 [0.44, 1.25], PA = 0.46 [0.22, 0.91], PO = 0.87 [0.34, 1.43], PR = 0.69 [0.30, 1.38]; Kruskal-Wallis test $\chi^2(4) = 91.1$, $p < 0.001$; post-hoc Wilcoxon rank-sum tests with Holm-Bonferroni correction 29e vs. MEC: $Z = 3.40$, $p < 0.001$; 29e vs. PA: $Z = 7.7$, $p < 0.001$; 29e vs. PO: $Z = 2.2$, $p = 0.025$; 29e vs. PR: $Z = 3.2$, $p = 0.002$). *Panel F* shows significantly reduced theta PPC of neurons in 29e (median [IQR] = 0.0016 [0.0004, 0.0052]) than in other regions (MEC = 0.0496 [0.0119, 0.1629], PA = 0.1040 [0.0192, 0.2773], PO = 0.0376 [0.0046, 0.2066], and PR = 0.0218 [0.0044, 0.1652]; Kruskal-Wallis test $\chi^2(4) = 235.7$, $p < 0.001$; post-hoc Wilcoxon rank-sum tests with Holm-Bonferroni correction 29e vs. MEC: $Z = -13.7$, $p < 0.001$; 29e vs. PA: $Z = -14.1$, $p < 0.001$; 29e vs. PO: $Z = -8.7$, $p < 0.001$; 29e vs. PR: $Z = -8.4$, $p < 0.001$).
**(G)** Inverse relationship between landmark-locking score and spike-LFP theta phase coupling, quantified by pairwise phase consistency (PPC), of spatially tuned 29e neurons (each represented with a dot) in *LM-failure sessions.* Spearman's correlation coefficient and *p*-value are given inside the figure.
**(H)** Negative nonlinear relationship between the partial $R^2$ (x-axis) for landmark-contrast tuning of 29e neurons and their corresponding PPC quantifying the spike-LFP theta phase coupling (y-axis). As in panel F, each dot is a neuron.
**(I)** Significant difference in spike-LFP theta phase coupling strength (quantified by theta PPC) between egocentric 29e neurons (median [IQR] = 0.0006 [0.0001, 0.0017]) and allocentric 29e neurons (0.0033 [0.0006, 0.0065]). Wilcoxon's rank-sum test egocentric vs. allocentric: $Z = -3.83$, $p < 0.001$.

**The breakdown of theta- and gamma-mediated interactions between area 29e and MEC LFPs signifies the loss of landmark control across the parahippocampal system**

To investigate the temporal interactions and coordination between 29e and MEC networks under conditions of LM-control and LM-failure, we measured coherence and Granger causality between 29e and MEC at theta and gamma frequencies. During periods of stationary landmarks (i.e., the initial epoch with experimental gain = 1; Fig. 2D-E), average LFP–LFP coherence across 29e–MEC tetrode pairs (n = 32; 4 rats) exceeded chance levels throughout the theta band and at multiple gamma bands (Fig. 6A), paralleling the spectral profile of significant oscillatory power in both regions (Fig. 5B). To assess causal influence between 29e and MEC LFPs, we computed the frequency-resolved Granger causality (GC) spectra (*44*, *45*) and calculated a *directed-influence asymmetry index* (DAI) as $(GC_{29e \rightarrow MEC} - GC_{MEC \rightarrow 29e})/(GC_{29e \rightarrow MEC} + GC_{MEC \rightarrow 29e})$ (*46*). A significantly negative DAI indicates a stronger drive from MEC onto 29e, whereas a significantly positive DAI indicates a dominant drive from 29e to MEC. This analysis revealed that MEC significantly drove 29e in the theta band, whereas 29e significantly drove MEC in the low-medium gamma band (Fig. 6B).

We quantified, for each 29e-MEC tetrode pair, the changes in coherence and Granger causality from the initial epoch with stationary landmarks to the final epoch with rotating landmarks as (final – initial)/(final + initial). In *LM-control* sessions, neither theta nor gamma coherence changed significantly, whereas in *LM-failure* sessions, both decreased significantly (Fig. 6C). The decrease in gamma-band coherence between initial and final epochs in *LM-failure* sessions was significantly larger than in *LM-control* sessions, but this comparison was not significant for theta-band coherence. These results demonstrate that LM-failure was associated with a reduction in gamma coherence between 29e and MEC, with more ambiguous evidence indicating a similar reduction in theta coherence.

Across these session types, Granger causality analyses showed direction- and band–specific effects. Figure 6D shows the DAI from Fig 6B separated into LM-control and LM-failure sessions. For LM-control sessions, there was little difference between the initial epoch and the final epoch in the directionality of Granger causality in either theta or gamma bands (Fig. 6D, top). Thus, regardless of whether there was a conflict between path integration and landmarks, the strength of gamma-mediated, 29e→MEC drive and the strength of theta-mediated, MEC→29e drive was not changed. However, for LM-failure sessions, there was an overall shift downward of the DAI curve (Fig 6D, bottom), indicating a decrease in the gamma-mediated, 29e→MEC drive and an increase in the theta-mediated, MEC→29e drive (note that a more negative DAI reflects a greater MEC→29e drive). Across all tetrode pairs, the difference in DAI between final and initial epochs was significantly negative for both theta and gamma bands (Fig. 6E; see fig. S11 for further breakdown of the components of the DAI). Thus, *LM-failure* sessions exhibited a weaker net influence from 29e to MEC, reflecting a breakdown or reversal of the normal 29e-to-MEC gamma-band influence.

To address whether the disruption of 29e-MEC LFP interactions emerged before or after the loss of landmark control in *LM-failure* sessions, we quantified the ongoing changes in the relative strength of landmark control vs. putative path-integration control via lap-to-lap correlation of the spatially binned population activity vector (excluding 29e neurons) relative to the rotating landmark frame (see Methods). The trajectory of this relative landmark-control strength closely matched the ongoing changes in 29e-MEC LFP coupling measures (coherence and DAI) in both theta and gamma bands, albeit with some temporal differences (Fig. 6F). Cross-correlation analyses identified a moderately strong positive relationship between ongoing changes in landmark control strength and each LFP coupling. Compared to circularly shuffled distributions, of the 18 tetrode pairs, correlations were significant ($\alpha = 0.05$) in 11 pairs for theta-band coherence, in 13 pairs for gamma-band coherence, in 10 pairs for theta-band DAI, and in 10 pairs for gamma-band DAI (all $p < 0.001$; binomial test against a null probability of 0.05). Further testing with linear mixed-effects models to account for non-independence among tetrodes and animals confirmed the significance of the positive association between changes in landmark-control strength and the LFP coupling measures (theta coherence: $\beta = 0.40$; gamma coherence: $\beta = 0.31$; theta DAI: $\beta = 0.38$ gamma DAI: $\beta = 0.21$; all $p < 0.001$).

Analysis of cross-correlation lags using significant tetrode pairs showed that ongoing changes in landmark-control strength were synchronous with changes in gamma-band coherence and theta-band DAI across laps, but were significantly preceded by changes in theta-band coherence and gamma-band DAI. A direct comparison between these leading indicators showed that changes in gamma-band DAI occurred significantly earlier than changes in theta-band coherence ($Z = -2.34$, $p = 0.019$). Taken together with the existence of landmark-anchored neurons within 29e and the dominant directionality of gamma drive from 29e to MEC during stable landmark control, this finding suggests that reduced 29e-to-MEC gamma drive precedes weakened error correction by landmarks, during which path-integration errors presumably accumulate, ultimately culminating in a sudden and complete failure of landmark control.

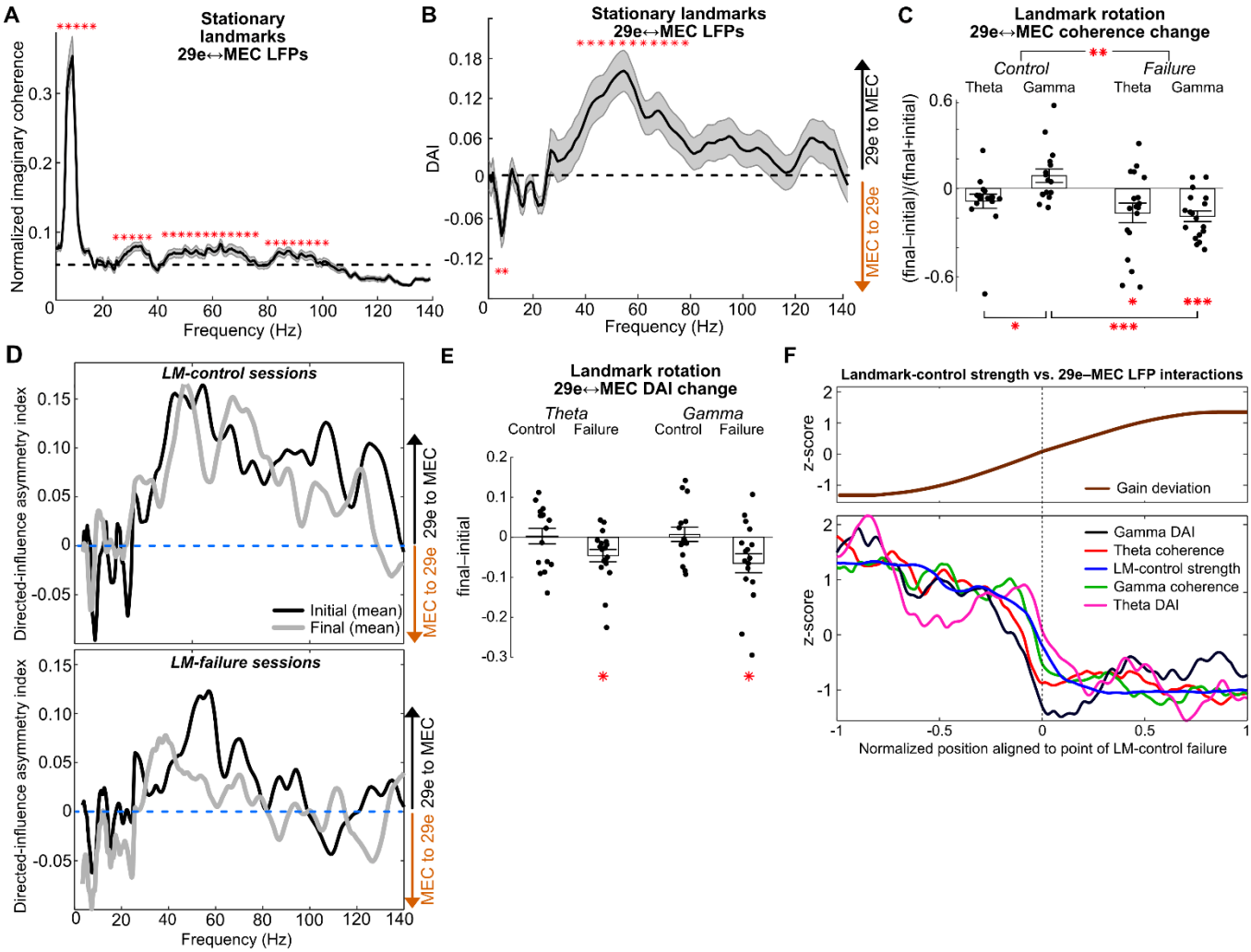


**Fig. 6.** Theta-gamma coordination between area 29e and MEC.
**(A)** LFP-LFP coherence spectrum between 29e and MEC when landmarks were stationary. Gray shaded area surrounding the solid black line indicates the mean ± s.e.m. of coherence spectra across 32 tetrode pairs. Asterisks mark the statistical significance of the coherence at a particular frequency, as measured by a hierarchical cluster-based permutation test to control familywise error rate at $\alpha = 0.05$.
**(B)** Directed-influence asymmetry index (DAI) between 29e and MEC when landmarks were stationary. The convention is the same as panel B.
**(C)** Normalized changes in theta- and gamma-band coherence between 29e and MEC LFPs from the initial epoch to the final epoch across *LM-control* and *LM-failure* sessions. Each dot represents a 29e-MEC tetrode pair; bars represent mean ± s.e.m. Asterisks below/above bars denote significance levels compared to zero; red asterisks below brackets denote significance between respective conditions. The coherence in LM-failure sessions was reduced significantly compared to initial sessions in both theta (mean ± s.e.m. = –0.21 ± 0.07, Holm-Bonferroni corrected one-sample t-test $t(17) = -2.5$ $p = 0.024$) and gamma bands (–0.19 ± 0.03, $t(17) = -5.2$ $p = 0.002$), whereas coherence in LM-control sessions did not differ significantly between initial and final sessions (theta : –0.08 ± 0.05, $t(15) = -1.7$ $p = 0.177$; gamma : 0.08 + 0.05, $t(15) = 1.82$ $p = 0.177$). There was a significant main effect of the session type (two-way repeated measures ANOVA; $F(1,32) = 8.5$, $p = 0.006$) and a significant two-way interaction of the session type x frequency-band ($F(1,32) = 8.5$, $p = 0.006$), but no significant main effect of the frequency band ($F(1,32) = 3.3$, $p = 0.077$). Post-hoc t tests identified two significant differences that underlie the interaction: gamma-band coherence changes in *LM-control vs. LM-failure* sessions (Holm-Bonferroni corrected $t(32) = 4.66$, $p < 0.001$) and theta vs. gamma-band coherence change within the *LM-control* session ($t(15) = 2.96$, $p = 0.028$).
**(D)** Mean DAI spectra across tetrode pairs in the initial (black) and final (grey) epochs of *LM-control* (left) and *LM-failure* (right)

sessions. The pattern of frequency-dependent DAI between epochs is similar across initial and final epochs in *LM-control* sessions. By contrast, the DAI in *LM-failure* sessions shifts downward in both theta- and gamma-bands, indicating a shift toward greater MEC drive onto 29e in the theta band and a decrease in 29e drive to MEC in the gamma band.
**(E)** Change in theta- and gamma-band directed-influence asymmetry index (DAI), quantified as $DAI_{final} - DAI_{initial}$, from the initial epoch with stationary landmarks to the final epoch with rotating landmarks across *LM-control* and *LM-failure* sessions. Each dot is a tetrode pair. Asterisks indicate significant comparisons relative to zero. DAI in failure sessions reduced significantly in both theta (mean ± s.e.m. = –0.050 ± 0.017, Holm-Bonferroni corrected one-sample t-test t(17) = –2.9 p = 0.039) and gamma bands (–0.071 ± 0.025, t(17) = –2.8 p = 0.039) whereas DAI in control sessions did not differ significantly from zero (theta : 0.003 ± 0.02, t(15) = 0.2 p = 1.000; gamma : 0.007 + 0.019, t(15) = 0.4 p = 1.000). Two-way repeated measures ANOVA (factors: session type and frequency-band) revealed significant main effect of the session type (F(1,32) = 9.0, p = 0.005), capturing the overall reduction in failure sessions as significantly different than the changes in control sessions. There was no significant main effect of the frequency band or the interaction.
**(F)** Average lapwise trajectories of gain deviation (top; defined as the absolute difference of experimental gain from 1) and of 29e–MEC LFP coupling measures (bottom) across 14 tetrode pairs from *LM-failure* sessions. One rat was excluded from this visualization due to instability of its non-29e neurons with respect to landmarks during stationary periods, but data from this rat were included in quantitative analyses. All traces were z-scored, smoothed with a moving average filter (half-width = 2 laps), aligned to the point of landmark-control failure (vertical dashed line at 0), time normalized (i.e., temporally scaled to also align the beginning and end points of all experiments), and averaged across tetrode pairs. For each session, the failure point was determined a priori—independently of quantitative analyses—by visual inspection of lapwise firing rate plots of non-29e neurons relative to landmarks (as in Fig. 2D–E); these visually identified failure points closely corresponded to the zero-crossing of the z-scored landmark-control strength trajectory in each session. Overall, the plots show that as gain deviation increased (top), landmark-control strength (bottom; blue) progressively declined, with a marked drop occurring at the point of landmark failure. This trend was closely tracked by the trajectories of 29e–MEC LFP coupling measures (theta-band coherence: median [IQR] Pearson's rho = 0.64 [0.28, 0.78]; gamma-band coherence = 0.66 [0.39, 0.79]; theta-band DAI = 0.41 [0.32, 0.53]; gamma-band DAI = 0.41 [0.30, 0.56]), but with apparent spatial (lapwise, x-axis) offsets. Specifically, reduction in gamma DAI—primarily reflecting loss of 29e→MEC gamma drive (see panel D)—preceded both the decline in landmark-control strength and changes in other LFP coupling measures. The decline in landmark-locking strength was largely synchronous with the decline in gamma coherence (median [IQR] lag (lap) = –0.2 [–1.4, 1.7]; Wilcoxon sign-rank test $Z = -0.22$, $p = 0.823$) and theta-band DAI (–1.6 [–3.6, 1.5]; $Z = -0.67$, $p = 0.498$), but was significantly preceded by changes in theta-band coherence (–0.6 [–1.6, 0]; $Z = -2.20$, $p = 0.027$) and gamma-band DAI (–3.0 [–4.0, –2.3]; $Z = -2.55$, $p = 0.010$).

## Gamma-band coupling and local circuit connectivity support coordination of landmark signals in 29e with parahippocampal circuits

To determine whether the spiking activities of 29e and MEC neurons are consistent with the LFP interactions reported above, we examined the coupling of spatially tuned 29e and MEC neurons to the other region's LFP using spike-LFP PPC (pairwise phase consistency). Consistent with the LFP-LFP coupling result (Fig. 6A), the spectral profile of cross-regional spike-LFP PPC showed clear peaks in the theta and gamma bands during periods of stationary landmarks in the Dome (Fig. 7A). The coupling of 29e neurons' firing to MEC gamma was significantly stronger than that of MEC neurons to 29e gamma, whereas the coupling of MEC neurons' firing to 29e theta was significantly stronger than that of 29e neurons' to MEC theta. This pattern matched the reversal in the dominant directionality of LFP-LFP Granger Causality influences across theta and gamma bands (Fig. 6B). While cross-regional PPC in both bands did not change significantly during gain manipulations in *LM-control* sessions, significant reductions in PPC were present during *LM-failure* sessions, specifically in the coupling of MEC neurons to 29e theta and 29e neurons to MEC gamma (Fig. 7B).

If the 29e neurons provided landmark information to MEC, we would expect that the landmark-anchored 29e neurons would be more strongly coupled than the non-anchored neurons to the MEC LFP. To test this hypothesis, we focused on *LM-failure* sessions—i.e., the only sessions for which we could dissociate the landmark-anchored from non-anchored neurons. We analyzed the cross-regional PPC spectra from the initial epoch (with stationary landmarks), calculating for each frequency the correlation between the neurons' PPC values and their landmark-locking scores (Fig. 7C). 29e neurons displayed a striking frequency-dependent pattern: coupling to higher frequencies of MEC gamma, particularly 100–120 Hz, was positively correlated with neurons' landmark-locking scores, whereas coupling to lower frequency MEC LFP oscillations, particularly in the theta-band, were negatively correlated with landmark-locking scores. By contrast, for MEC neurons, PPC–landmark-locking correlations were overall weak, with a modest significant peak at gamma frequencies around 80 Hz and no significant relationships otherwise. These results demonstrate that, under baseline conditions (i.e., stable landmarks), the landmark-anchored subpopulation of 29e were strongly coupled to MEC gamma and weakly coupled to MEC theta. In 29e, the difference between the maximum correlation at higher frequencies (> 50 Hz) and the minimum correlation at lower frequencies (<

20 Hz) was significantly greater than expected by chance ($p$ = 0.006) based on permutation controls (fig. S11B), whereas in MEC, this difference was non-significant ($p$ = 0.078*;* fig. S11C*)*.

Were the landmark-anchored 29e cells more likely to lose their coupling to MEC gamma than the non-anchored neurons when the MEC spatial maps broke free from the landmarks? Dividing 29e and MEC neuron populations into "PPC loss" and "PPC gain" groups at each frequency along the spectrum and comparing their landmark-locking scores produced a significant difference between the two groups only in 29e (fig. S11D). Specifically, among 29e neurons, loss of coupling to MEC gamma was associated with significantly higher landmark-locking scores, while gain of coupling to MEC theta was associated with significantly lower landmark-locking scores. This frequency-dependent pattern closely resembled the baseline PPC correlation results (Fig. 7C), suggesting that baseline coupling level may have confounded these group differences by affecting both whether a neuron loses or gains coupling toward a mean level and its degree of landmark anchoring. To control for this potentially confounding effect, we performed a logistic regression analysis, using baseline PPC values and landmark-locking scores as predictors, and the direction of PPC change (loss vs. gain) as the outcome variable. The logistic regression revealed that, after accounting for baseline PPC levels, the landmark-locking score remained a significant positive predictor of 29e neuron's PPC loss to MEC gamma (particularly 100–120 Hz; Fig. 7D). No significant association remained relative to lower-frequency oscillations of MEC LFP (e.g., theta), nor was it observed for MEC neurons' coupling to 29e LFP across the entire frequency spectrum. These findings suggest that gamma-band synchrony between 29e's landmark-anchored subpopulation and MEC may mediate the transfer of landmark-related information to parahippocampal path-integration circuits; accordingly, disruption of this synchrony may interfere with landmark control.

As a direct test of a landmark-information transfer from landmark-anchored 29e subpopulation to downstream neurons, we searched for putative monosynaptic excitatory connections among all simultaneously recorded neurons using their spike cross-correlograms. Although interregional connections in our data were too scarce to perform meaningful analyses, many intraregional connections were identified. Among 32 putative monosynaptic connections between 29e neurons during *LM-failure* sessions, presynaptic neurons exhibited significantly larger landmark-locking scores than their postsynaptic targets (Fig. 7E). In other regions (MEC, PA, PO, and PR), however, landmark-locking scores did not differ between pre- and post-synaptic neurons of putative monosynaptic connections (fig. S12). A direct comparison of the landmark-locking score difference (presynaptic–postsynaptic) between 29e and other regions (non-29e) confirmed that the greater landmark anchoring of presynaptic neurons compared to their postsynaptic targets was an effect specific to 29e (Wilcoxon's rank-sum test $Z = 2.8$, $p = 0.004$). Taken together with the selective loss of gamma-band coupling between landmark-anchored 29e neurons and MEC during landmark-control failure, this synaptic gradient of landmark anchoring within 29e provides evidence that landmark-anchored 29e neurons may serve as a key source of landmark information for parahippocampal circuits of path integration.

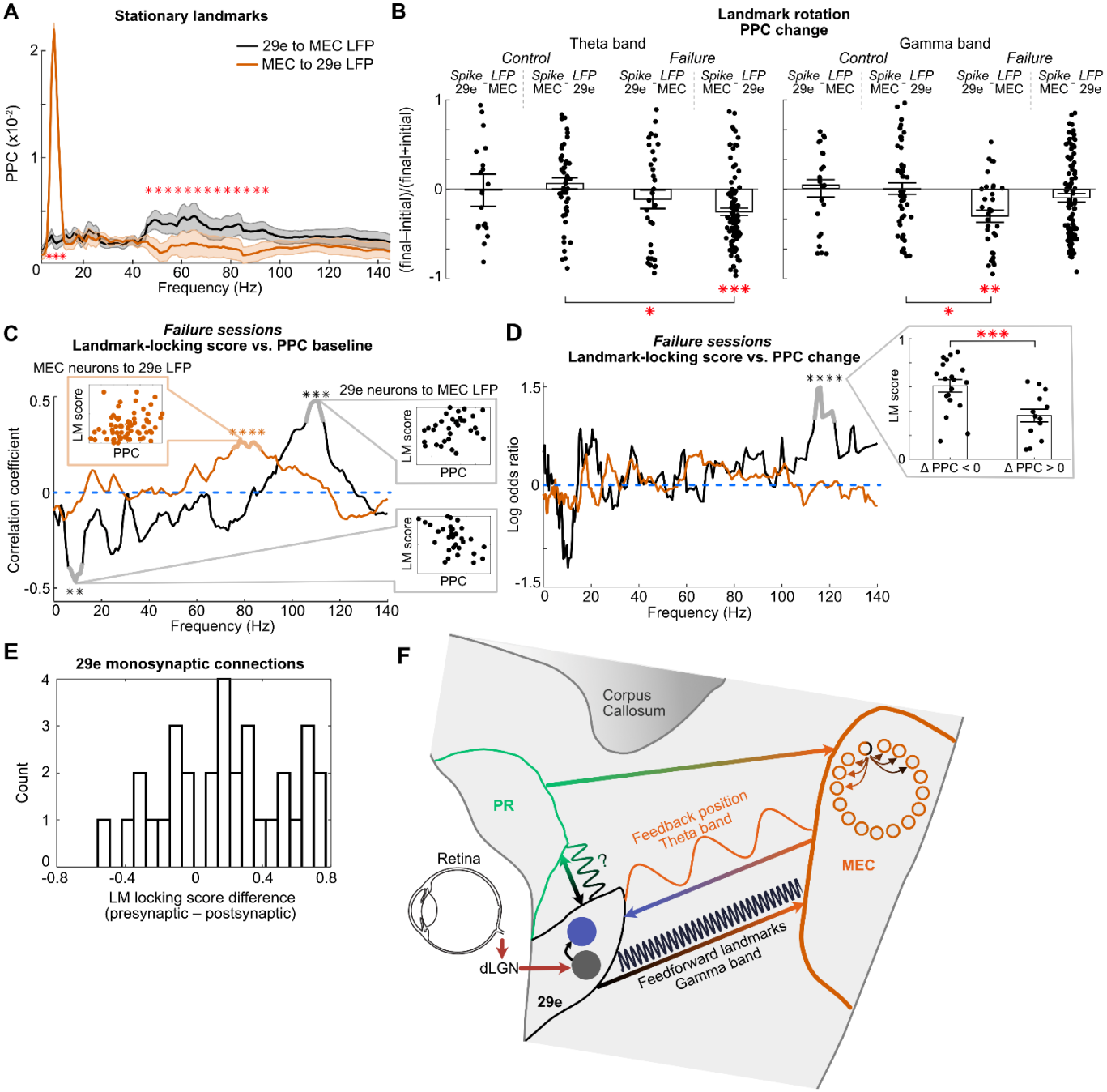


**Fig. 7.** MEC-gamma coupling, local connectivity of landmark-anchored 29e neurons and a conceptual model of inter-areal communication between area 29e and other parahippocampal areas.

**(A)** Cross-regional spike-LFP coupling spectrum between 29e and MEC when landmarks were stationary. Shaded area surrounding the solid black (29e neurons' coupling to MEC LFP) and orange (MEC neurons' coupling to 29e LFP) lines indicate the mean ± s.e.m. of the respective spike-LFP spectra. Asterisks mark the statistically significant differences between the two cross-coupling spectra at specific frequencies, determined by a cluster-based permutation test to control familywise error rate at α =0.05.

**(B)** Normalized changes in cross-regional spike-LFP coupling ([final – initial]/[final + initial]) for each neuron between 29e and MEC across *LM-control* and *LM-failure* sessions. Each dot represents a single neuron; bars indicate mean ± s.e.m. Asterisks below/above bars denote significance levels compared to zero; red asterisks below brackets denote significance between respective conditions. In *LM-control* sessions, coupling changes did not differ significantly from zero in either theta band (29 neurons-to-MEC theta: median [IQR] = –0.02 [–0.42, 0.44]; Holm-Bonferroni corrected Wilcoxon sign-rank test $Z = 0.2$, $p = 1.000$; MEC neuron–29e theta: 0.07 [–0.21, –0.32]; $Z = 1.1$, $p = 1.000$) or gamma band (29e neurons-to-MEC gamma: 0.04 [–0.49, 0.36]; $Z = –0.3$, $p = 1.000$; MEC neurons-to-29e gamma: –0.06 [–0.32, 0.26]; $Z = 0.09$, $p = 1.000$). By contrast, *LM-failure* sessions showed significant reductions in couplings of 29e neurons-to-MEC gamma (–0.31 [–0.55, –0.02]; $Z = –3.56$, $p = 0.001$) and of MEC neurons-to-29e theta (–0.32 [–0.52, –0.08]; $Z = –5.21$, $p < 0.001$) but no significant change in couplings of 29e neurons-to-MEC theta (–0.15 [–0.77, 0.41]; $Z = –1.12$, $p = 0.262$) or of MEC neurons-to-29e gamma (–0.16 [–0.51, 0.27]; $Z = –2.00$, $p = 0.092$). Three-way repeated measures ANOVA (factors: session type, frequency-band, and neuron region-LFP region pair identity) revealed significant main effect of the session type ($F(1,202) = 9.7$, $p = 0.002$) and a significant three-way interaction ($F(1,202) = 4.0$, $p = 0.048$) but no significant main effects of the frequency-band ($F(1,202) = 0.3$, $p = 0.583$) or neuron-LFP region pair ($F(1,202) = 0.54$, $p = 0.463$), or any two way interaction. Holm-Bonferroni corrected post-hoc pairwise Wilcoxon tests within each frequency band identified two significant differences pertaining to the interaction effect. Within theta-

band, the changes in MEC neuron-29e LFP theta coupling was significantly lower in *LM-failure* sessions than *LM-control* sessions ($Z = -4.4$, $p < 0.001$). Within gamma-band, the changes in 29e neuron-MEC LFP coupling across *LM-failure* sessions was significantly lower than the changes in MEC neuron-29e LFP coupling across *LM-control* sessions ($Z = -3.2$, $p = 0.012$).
**(C)** Correlation between baseline cross-regional spike-LFP PPC and landmark-locking score measured during the final 12 laps with rotating landmarks during failure sessions. Spearman's correlation coefficient (y axis; chosen for its robustness to skewness and magnitude differences in neurons' PPC values) is shown as a function of frequency (x axis) for MEC neurons to 29e LFP (orange) and for 29e neurons to MEC LFP (black). Insets show example scatterplots of landmark-locking scores (abbreviated as LM score) versus PPC values (arcsinh-transformed for visualization) at selected frequencies. Asterisks (color coded the same as the lines) and lighter color, thickened segments indicate frequency ranges with significant nonzero correlations (cluster-based permutation test to control familywise error rate at $\alpha = 0.05$).
**(D)** Logistic regression analysis relating landmark-locking score to direction of PPC change ($\Delta$PPC) across frequencies during failure sessions. The log odds ratio ($\beta$ coefficient from logistic regression; y axis) for landmark-locking score as a predictor of PPC loss ($\Delta PPC < 0$) versus gain ($\Delta PPC > 0$) is plotted as a function of frequency (x axis) for 29e neurons coupling to MEC LFP (black) and MEC neurons coupling to 29e LFP (orange). A log odds ratio of 0 indicates no change in the odds of PPC loss as per one standard-deviation increase in landmark-locking score, while a log odds ratio of 1.5 indicates an increase in odds by a factor of $\exp(1.5) \approx 4.5$ per the same amount of change in landmark-locking score. Asterisks and grey, thickened segments indicate the significant frequency ranges, determined based cluster-based permutation test as before.
**(E)** Distribution of landmark-locking score difference between pre- and post-synaptic neurons among putative monosynaptically connected neuron pairs of 29e. The distribution's mean was significantly greater than zero (mean ± s.e.m. = 0.19 ± 0.06; $t(31) = 3.04$, $p = 0.004$).
**(F)** Conceptual model of area-29e–mediated landmark control of path integration. Based on established anatomy and our physiological findings, we propose that $\gamma$-band drive from 29e conveys feedforward landmark information to MEC, whereas $\theta$-band drive from MEC conveys feedback, path-integration–based position estimates to 29e. Area 29e is reciprocally connected with MEC and PR and receives low-latency landmark signals via a direct retina→dLGN→29e relay that bypasses primary and secondary visual cortex. We propose that these visual landmark signals differentially innervate 29e neurons, yielding the gradient of landmark anchoring observed in our data. For simplicity, the schematic renders this continuum as two subpopulations, "landmark-locked" (dark gray) and "landmark-unlocked" (purple). Feedforward output from 29e could arise from the strongly landmark-anchored subpopulation, consistent with their stronger spike–LFP coupling to MEC $\gamma$ during landmark control and the largest loss of $\gamma$ coupling when landmark control failed. We further hypothesize that MEC feedback preferentially innervates the less landmark-anchored subset, accounting for their stronger $\theta$ coupling and functional similarities to neurons in other parahippocampal areas, including MEC. MEC, the putative path-integration hub, is often modeled as a continuous attractor network; during landmark failure, the MEC neuron population remained largely homogeneous—either landmark-controlled or not—consistent with attractor dynamics. Within 29e, putative monosynaptic connections are biased from landmark-locked to landmark-unlocked neurons, consistent with the skewness in the distribution of (presynaptic – postsynaptic) landmark-locking scores. Consequently, the 29e landmark-unlocked population integrates inputs from locked 29e cells as well as from other parahippocampal areas. A parallel route from 29e to MEC may relay via PR, although effective communication between 29e and PR remains to be shown. Together, these interactions form a functional loop in which 29e provides landmark-based correction signals to MEC path-integration circuits, while MEC feeds back position signals to 29e. Arrows denote established anatomical connectivity; colored waveforms indicate relevant frequency bands.

## Discussion

Brains build internal models to predict the world, and because the world is dynamic, these models must be continually updated by sensory feedback. In navigation, the cognitive map embodies an internal model of space, and external landmarks provide allothetic spatial cues to recognize environments and locations within them and to correct accumulated errors in the path-integration-based estimates of position on this map. The neural origins of the landmark-based correction signal remain unknown in mammals. To address this gap, we performed simultaneous recordings in rats across five parahippocampal regions in an immersive VR apparatus that preserves natural, unrestrained locomotion while affording accurate control over the position and salience of visual landmarks, thereby allowing us to probe the interplay between external cues and internal computation. Our results reveal physiological and functional dissociations between area 29e and its neighboring regions, providing the first such characterization of area 29e in rodents. Large cue conflicts from rapidly rotating distal visual landmarks disrupted landmark anchoring in most spatial neurons across MEC, PA, PO, and PR. However, many 29e neurons maintained landmark anchoring, even during immobility. Area 29e showed weaker theta in the LFP and weaker theta modulation of its neurons' spiking compared to MEC, PA, PO, and PR. 29e also showed stronger egocentric and landmark contrast tuning than other regions, and these sensory properties were markedly enhanced in its landmark-anchored subpopulation. Taken together with dynamic functional coupling between 29e and MEC that tracks the degree of landmark control, our results identify a visually driven, egocentric-HD population in 29e that relays landmark signals to parahippocampal circuits supporting path integration.

The *predictive coding framework* proposes that rapidly changing sensory information and prediction errors are conveyed via feedforward connections, while slower contextual predictions are transmitted via feedback connections (*47*). Consistent with these timescales, feedforward and feedback anatomical pathways within visual cortex operate at distinct frequency bands: bottom-up, feedforward signaling in high-frequency (gamma) and top-down feedback signaling in low-frequency (alpha/beta) brain rhythms (*46*, *48–50*). We found an analogous organization in the parahippocampal system: area 29e influenced MEC primarily in the gamma band, whereas MEC influenced 29e predominantly in the theta band, forming a gamma–theta-mediated closed loop that signals feedforward landmark information and feedback positional predictions between 29e and MEC (Fig. 7F). When path integration and landmark-based positional cues became increasingly in conflict in our experiments, in many cases these frequency-specific interactions were disrupted and 29e-MEC rhythms became desynchronized, followed by a disruption of landmark control across the parahippocampal system. At the level of individual neurons, 29e neurons that were strongly coupled to MEC theta exhibited reduced landmark anchoring and contrast sensitivity—similar to MEC neurons and thus presumably reflecting greater feedback influence from MEC—whereas those strongly coupled to MEC gamma exhibited enhanced landmark anchoring, consistent with a more feedforward role in 29e signaling landmark information to MEC.

Theta oscillations (4-8 Hz) are among the most prominent rhythms in the rodent brain, particularly dominant in the medial temporal lobe, where they play a crucial role in spatial learning and memory encoding (*1*, *51*, *52*). Traditionally, hippocampal and parahippocampal areas have been characterized by allocentric spatial cells that show strong theta modulation (*2*, *4*, *9*, *40*, *53*). However, recent studies have identified egocentric spatial cells in lateral entorhinal cortex, a parahippocampal area with weak theta modulation (*54*), and in a population of neurons with weak theta modulation in the postrhinal cortex (*55*). Our results show that the dissociation between weaker theta modulation in egocentric head-direction cells and stronger theta modulation in allocentric head-direction cells extends these findings to other parahippocampal regions, suggesting a general organizing principle of spatial processing in the parahippocampal system (i.e., allocentric processing is theta modulated, egocentric processing is not).

Area 29e's distinct physiological and functional properties raise the possibility that it serves a specialized computational role distinct from the theta-coordinated parahippocampal network. Brodmann divided the retrosplenial cortex (area 29) into five subfields (29a–e), noting that 29e differed from the others (*56*). Other anatomists treated 29e inconsistently: some incorporated 29e into PR or RSC (*57–61*), while others considered it part of PA (*62–64*). We targeted area 29e based on its identification in rats as a cytoarchitecturally distinct triangular field interposed between PR and PA (*23*, *65*). Recent work proposed that area 29e is the rodent homolog of the primate visual area prostriata (*20*, *28*, *66*), which is located next to the region of striate cortex (V1) that represents the most extreme periphery of the visual field and is characterized by broad orientation tuning, large receptive fields, and selectivity for fast-moving stimuli in peripheral vision (*22*, *21*, *67*, *68*).

29e neurons displayed hallmarks of distal visual landmark representation—strong landmark anchoring, contrast sensitivity, and egocentric HD tuning anchored to locations beyond the open arena. Consistent with these properties, recent work revealed that rodent prostriata receives widespread input from medial V1 (which processes peripheral vision) and dorsal lateral geniculate nucleus (dLGN; *36*, *37*, *39*). The direct dLGN connection places prostriata only two synapses from the retinal ganglion cells, potentially providing the fastest visual pathway to limbic circuits and explaining the short-latency responses observed in primates (*22*, *67*). Distal cues are known to be more powerful than proximal landmarks in controlling the preferred directions of HD cells, which are thought to be the major signal that orients the cognitive map relative to the external world. Prostriata efferents target PR and MEC (albeit more sparsely than PR), in addition to contralateral prostriata and visuomotor areas (*25*, *27*). Because MEC is also innervated by PR (*69*, *70*), considered a critical site (among others) for integration of an internal HD signal with external landmarks (*34*, *71–75*, *55*), this anatomical organization suggests at least two potential routes via which 29e might deliver visual landmark information to MEC, the putative locus for path integration. In support of such a route, our data showed that decline in 29e's gamma-band influence on MEC preceded landmark-control failure, a period also characterized by weakened coupling of 29e’s landmark-anchored population to MEC gamma. Experiments with targeted reversible inactivation will clarify the causal roles and anatomical pathways of 29e's landmark signals within the parahippocampal system.

# Methods

## Subjects

Five adult Long–Evans rats (Envigo Harlan) served as subjects: three males (IDs 994, 995, 1041) and two females (IDs 1061, 1062). At the time of surgery, males weighed 440–470 g and were 6–9 months old, whereas females weighed 315–325 g and were 15–18 months old. Animals were housed individually in a temperature- and humidity-controlled room on a 12 h:12 h light/dark cycle; all behavioral training and electrophysiological recordings were carried out during the dark phase. Rats were handled nearly daily throughout habituation, training, surgery, and data-collection periods. Data from all five animals were pooled for all subsequent analyses. All procedures conformed to the National Institutes of Health guidelines and were approved by the Johns Hopkins University Institutional Animal Care and Use Committee.

## Training

Rats were handled daily for 3-5 days initially to habituate them to human contact, then placed on a controlled feeding schedule to reduce body weight to approximately 80% of their *ad libitum* weight.

*Dome training:* Rats were first trained on a circular table in a room separate from the Dome apparatus. The table matched the Dome table in diameter but lacked the enclosure and automation (see "Dome apparatus"). Reward droplets (1:1 mixture of water and chocolate Ensure) were placed manually at arbitrary locations on the track, and the interval between rewards gradually increased to sustain running and delay satiation. Training continued until the rats consistently completed at least 80 laps in the same direction without experimenter intervention, typically after 3–4 weeks. The rats were then introduced to the Dome, which contained stationary visual landmarks, and trained there until their lap counts matched those achieved on the open table, usually within one additional week. After hyperdrive implantation, the rats were re-trained in the Dome and transitioned to automated reward delivery, in which drop timing varied to encourage continuous forward running with minimal pauses. Experiments began once the tetrodes reached the target recording regions and the rats consistently ran many laps.

*Open-arena training*: While rats were being trained to run laps on the circular training table, we simultaneously acclimated them to the open arena by giving them 2–3 consecutive days of free foraging for Bio-Serv Dustless Precision Pellets, intended to promote spontaneous exploration. After 1–2 weeks they explored the entire arena readily and uniformly. At this stage rats underwent surgical hyperdrive implantation. During postoperative foraging sessions we attached a FreeLynx wireless transmitter to the hyperdrive so that the rats could become accustomed to its weight (the FreeLynx was used in a subset of both dome and open-arena recordings; see "Open-arena apparatus"). Training continued until the rat, with the transmitter in place, traversed the arena broadly and almost continuously, pausing only briefly—a criterion typically achieved within 7–14 days after surgery. Experiments began once this behavioral criterion, the dome-training criterion, and accurate tetrode placement had all been met.

## Surgery and electrode implantation

After behavioral training, rats were implanted with custom hyperdrives carrying 18 independently drivable tetrodes . Each tetrode was composed of four twisted, heat-bonded nichrome wires (0.0017″ diameter, VG/HML insulation; California Fine Wire Co., CA, USA). Hyperdrives were built in-house using a custom design around a 72-channel interface board (EIB-72-QC; Neuralynx, Bozeman, MT, USA). During the 5–6 days preceding surgery, tetrode tips were gold-plated daily with a nanoZ system (White Matter LLC, Seattle, WA, USA) to reduce and stabilize impedance from 2–3 MΩ to ~130 kΩ. Each assembled hyperdrive was sterilized in ethylene-oxide gas (12-h cycle) and allowed to aerate for 36 h before implantation.

Anesthesia prior to surgery was induced with 4% isoflurane in oxygen (1 L/min) followed by ketamine (80 mg/kg) and xylazine (10 mg/kg); anesthesia was maintained with isoflurane as needed. Local analgesia was provided by applying 0.15 mL of bupivacaine (Marcaine) or ropivacaine directly to the skull. Postoperatively, meloxicam (1–2 mg/kg; Ostilox, Meloxidyl, or Metacam) was administered orally for two days. Postoperative antibiotics (30 mg tetracycline and 0.15 mL of a 22.7% enrofloxacin solution) were

given orally once daily for 10 days post-surgery. Under isoflurane anesthesia, a craniotomy was made over the right hemisphere, the rostral edge of the transverse sinus was exposed, and the dura was removed. The hyperdrive was positioned so that the posterior-most central tetrode entered the brain 350–530 µm anterior to the rostral edge of the transverse sinus and 4.30–4.55 mm lateral to bregma, yielding a mediolateral recording span of 3.4–5.45 mm lateral to bregma across animals. To increase effective tetrode travel within MEC, the hyperdrive was tilted 10° anteriorly in the sagittal plane. The craniotomy was then sealed with Kwik-Sil (World Precision Instruments). Hyperdrives were anchored to the skull with jeweler's screws; a screw over the cerebellum served as the recording ground. The implant was secured with a three-layer build of OptiBond (Kerr Dental), Charisma (Kulzer), and dental cement.

**Histology and tetrode track reconstruction**

After the final recording sessions, rats were transcardially perfused with 3.7% formalin. To improve the quality of tetrode tracks, the brain was partially exposed and soaked in PFA or formalin overnight with the hyperdrive attached before tetrodes were retracted. The brain was extracted and stored in 30% sucrose-formalin solution until fully submerged, and sectioned coronally at 40 µm intervals. The sections were mounted and stained with 0.1% cresyl violet.

For tetrode track reconstruction, Nissl-stained serial sections were imaged on a light microscope, and whole-section images were acquired with IC Capture 2.1. Images were imported into Free-D (*76*) for manual tracing of tetrode tracks across consecutive sections and 3D reconstruction of each tetrode's trajectory. Reconstructed trajectories were visualized from the top-down and registered to the known hyperdrive bundle geometry to assign tetrode identities. For each identified tetrode, the 3D trajectory was exported as an STL file and analyzed in MATLAB to compute the centerline (central axis) and its arc length, providing a measure of distance traveled. We tied arc-length positions to depth using one reference point per tetrode: the most ventral point of the 3D trajectory for in-brain tracks, or, for tracks that exited, the screw-turn value at layer II exit (estimated by the loss of spiking activity) entry, mapped to its Free-D pixel coordinates. This yielded a one-to-one mapping between screw turns and arc-length positions along the 3D trajectory. Using this mapping, per-session depths expressed in screw turns were converted to pixel coordinates and slice indices and these coordinates were examined under a high-magnification microscope to assign region identities.

High-resolution images of histological sections (Fig. 1A; fig. S1) were acquired on a KEYENCE BZ-X1000 fluorescence microscope, capturing six brightfield tiles (2×3) with a 4x objective and stitching them into a single mosaic with the BZ-X Analyzer (Stitching & Multi-Point Imaging module).

**Neural recordings**

Wideband signals were digitized at 30 kHz and acquired on a computer running Neuralynx Cheetah software using either a wireless FreeLynx transmitter or, for wired sessions, a Litz tether connected to a Digital Lynx SX system by a unity gain 72 channel headstage (HS72QC, Neuralynx) attached to the implanted hyperdrive. Both dome and open arena experiments were run with either wired or wireless configurations of this recording system. TTL pulses from the behavioral control computer (see Experimental control) were recorded as timestamped events on the acquisition system to enable post hoc synchronization of behavioral and neural data. Raw wideband data were saved as Neuralynx .nrd files and used for spike sorting.

**Experiment control and behavior tracking**

Dome sessions were run using three computers: (1) an experiment-control PC, (2) a neural-acquisition PC running Cheetah (Neuralynx), and (3) a video-tracking PC. Task logic and device control were implemented as Robot Operating System (*77*) nodes communicating continuously with a master node on the experiment-control PC. Synchronization was achieved by sending pseudorandom TTL pulses from the control PC to the acquisition system; these were time-stamped in Cheetah and used to align data streams across machines. Hardware/software integration and control details are described in a previous publication (*29*). Head position and 3D head orientation were estimated in real time at 30-45 fps using a single-camera, ROS-based tracker

that used custom software and fiducial markers mounted on the hyperdrive in a known 3D configuration (*78*).

Open-arena sessions typically used two computers: one for neural acquisition with FreeLynx/Cheetah and one for behavior tracking running the single-camera 3D tracker. In a subset of sessions recorded with the wired Digital Lynx SX system, a single computer handled both neural acquisition and behavioral tracking; in those sessions, head position and 2D head orientation were extracted from two LEDs mounted on the headstage.

**Spike sorting**

Wideband extracellular recordings were band-pass filtered between 300 and 3000 Hz to isolate spiking activity, whitened, and artifact-masked before automatic spike detection and clustering with MountainSort4 (*79*). Outlier events within each cluster were identified in the peak-amplitude feature space of the spike waveforms using MATLAB's *robustcov* function and removed, thereby reducing residual contamination from other sources (*80*). The cleaned clusters were transferred to Phy via the SpikeInterface framework (*81*) for further manual curation based on spike waveforms, amplitude stability over time, and the distribution of waveforms in principal-component feature space. Inter-spike-interval histograms and pairwise cross-correlograms were also examined to decide whether clusters should be merged or split: clusters were split when mixed waveform populations were evident and merged when two clusters displayed nearly identical waveforms together with a pronounced refractory trough in their cross-correlogram. Units showing clear amplitude drift or more than 1% of inter-spike intervals shorter than a 1.5 ms refractory period were discarded. The remaining well-isolated, temporally stable clusters were retained for all subsequent analyses. In a subset of sessions, MountainSort4 units were compared to manually sorted clusters using custom software (WinClust, J. J. Knierim) in a subset of sessions and showed comparable isolation quality, as indicated by similar waveform features and refractory-period violations.

**Selection criteria for independent neuron and LFP samples**

To avoid including the same neuron more than once, we employed a deliberately conservative, depth-based duplicate-control procedure. Two clusters recorded on different days were judged to be distinct only if the tetrode had been advanced by at least three ⅛-turn screw steps—equivalent to 3/8 of a 0-80 screw pitch, or ≈119 µm. For each analysis, clusters from all sessions were first pooled by rat and tetrode; the largest subset of clusters that satisfied this constraint was then chosen through an optimization algorithm. The same depth-based constraint was applied to LFP signals: LFPs from the same region were considered independent samples only if they were recorded at least 119 µm apart.

**Inclusion criteria**

During preprocessing, we enforced a common set of inclusion criteria across analyses. Unless otherwise specified, spikes were analyzed only when the animal's running speed exceeded 4 cm/s and landmarks were visible. Units were included if they produced ≥ 100 spikes within the relevant analysis epochs. Only clusters that could be unequivocally assigned to MEC, PA, PO, PR, or 29e—by histological examination, or, when histology was ambiguous, by our physiological-feature classifier—were retained (see "Brain region classification from single-cell physiological features").

For tetrode-level landmark-OFF response analyses (Fig. 3A, B), tetrodes were included only if the population mean firing rate was ≥ 2.5 Hz during the analyzed period. For cross-regional LFP interaction analyses, a tetrode was included only if at least one spatially tuned neuron was recorded during the period with stationary landmarks in the Dome VR. For monosynaptic-connection analyses, putative monosynaptic pairs were considered only if both participating units fired at ≥ 0.2 Hz on average.

For open-arena analyses, we used sessions that were ≥ 20 min. To ensure sufficient coverage during running, we further required that in every square bin of a coarse 4 × 4 grid tiling the arena, the animal had spent at least 75 seconds over the full session and at least 30 seconds within each half of the session.

For cross-regional LFP-LFP and spike-LFP coupling analyses, we used tetrodes that had at least one spatially tuned neuron, detected based on the initial epoch of the Dome VR experiments with stationary landmarks.

**Cluster matching between dome and open arena recording sessions**

Neurons were matched across dome and open arena recording sessions performed on the same day based on the similarity of their spike waveform features. Peak waveform voltage features from the tetrode channels were extracted for each cluster and modeled as multivariate Gaussian distributions. The 'cluster distance' between each pair of clusters across sessions was quantified as the minimum of the two asymmetric Kullback-Leibler (KL) divergence values between their Gaussian distributions. All dome-open arena cluster pairs that had a cluster distance > 8 were discarded. For each cluster in a given session (i.e., Dome or open arena), we picked the cluster in the other session with the minimum cluster distance as its putative match. If another candidate cluster fell within 0.5 of that minimum cluster distance, we treated that case as ambiguous and did not assign a matching cluster and rejected the putative match. Finally, we only kept matches that were bidirectional, i.e. each cluster had to choose the other as its unambiguous match.

**Statistics**

Statistical analyses were performed in MATLAB (MathWorks). All tests were two-sided and evaluated at a familywise $\alpha = 0.05$ unless otherwise indicated. Whenever multiple comparisons were performed, p-values were adjusted using the Holm–Bonferroni step-down method to control the familywise error rate.

Nonparametric tests (Kruskal-Wallis for multi group, Wilcoxon tests for two groups) were used for multiple group comparisons unless data satisfied the following parametric assumptions. Normality was assessed with the Shapiro–Wilk test (*82*). For groups exhibiting evidence of heavy tails (sample kurtosis > 3), we used the Shapiro–Francia test (*83–85*). Homogeneity of variances across groups was examined with both Levene's test (absolute-deviation variant) and Bartlett's $\chi^2$ test (MATLAB *vartestn* with options 'LeveneAbsolute' and 'Bartlett'). If every group passed the normality test and either one of the tests for equal variances were non-significant ($p > 0.05$), we treated the data as suitable for parametric analysis. We ran a one-way ANOVA to test for overall group differences, checked that the ANOVA residuals were still normal, and then compared groups pairwise with standard two-sample t-tests.

For two group unpaired comparisons, we used the nonparametric Wilcoxon rank-sum test unless the data met parametric assumptions. If both groups were normally distributed, we tested equality of variances with the two-sample F-test; equal variances led to the standard two-sample t-test, and unequal variances led to Welch's t-test. For paired data, we analyzed the within-pair differences: if these difference scores were normally distributed, we applied a paired t-test; otherwise, we used the Wilcoxon signed-rank test.

**Dome apparatus**

The virtual-reality Dome (*12*, *29*) is a planetarium-style setup built around a hemispherical fiberglass shell with a 2.3-m inner diameter. A 15-cm aperture at the apex allowed light emitted from a ceiling-mounted projector (Sony VPL-FH30) fitted with a long-throw lens (Navitar ZM 70–125 mm). A 25-cm hemispherical first-surface mirror (JR Cumberland), mounted on a central pillar at the geometric center, reflected the projected image onto the inner surface of the dome to create full-field visual stimulation. Visual scenes were rendered in C++ using OpenGL and pre-warped to compensate for the projection optics before display. To provide uniform, rotationally symmetric background illumination that did not overlap the landmarks, a narrow overhead ring was projected continuously, including during landmark-absent epochs. Behavior was monitored with an overhead near-infrared camera providing real-time, top-down video (see "Experiment control and behavior tracking").

Rats locomoted along the outer edge of an annular table (outer diameter 152.4 cm, inner diameter 45.7 cm) positioned at the center of the Dome. An enclosure subtending 45° around the rat was attached to a motorized central pillar via radial boom arms to ensure that the animal remains near the table's outer rim and to carry the transmitter unit of the neural recording system (in wireless recording sessions) or the headstage and Litz tethers (for wired recording sessions). The motorized central pillar incrementally advanced the

enclosure to keep the rat near a predefined setpoint within the enclosure; it engaged only when the rat was within a defined window around that setpoint, ensuring the enclosure moved along with the rat. Liquid rewards (Ensure diluted 50% with water) were delivered pseudo randomly onto the table via a feed tube mounted on a boom arm diametrically opposite the enclosure; delivery timing and volume were controlled by a micro-peristaltic pump (Takasago fluidics) on the central pillar using custom software (*29*). This boom arm also held a plastic spreader and paper towels to disperse urine and food odors and to remove feces, minimizing the salience and stability of local olfactory cues. After each session the track was thoroughly wiped and then rotated by a multiple of 45° (one of eight possible orientations), altering the spatial relationship of any tactile cues to the rest of the apparatus. This prevented local tactile features on the annular track from becoming stable global landmarks.

**Open arena apparatus**

During open-field foraging sessions, each rat foraged for randomly distributed precision chocolate pellets (Bio-Serv Dustless Precision Pellets, Purified), on a square platform that measured 137 × 137 cm and was surrounded by opaque walls 36.5 cm high. Experiments were conducted in two different recording rooms. In the larger room (approximately 330 × 700 cm) neural activity was transmitted wirelessly via a FreeLynx device, whereas in the second room (292 × 292 cm) signals were carried through a tether connected to a DigitalLynx SX system and Saturn commutator. Both rooms were dimly illuminated by overhead white LEDs and contained fixed distal cues—such as shelving, computers, and other laboratory equipment—that were largely kept in the same positions across days to provide stable landmarks for the animals. After every session the arena floor was wiped with 70 % ethanol. Any urine or feces were removed immediately during the sessions once the rat had moved away from that spot. Throughout each 30-40 min session the experimenter walked outside the arena while dispensing the chocolate precision pellets.

**Closed-loop gain manipulation experiments**

Location of visual landmarks were updated in closed loop with the rat's movement according to an experimental gain, G, defined as the ratio between landmark-frame and laboratory-frame speed. Landmarks were stationary when $G = 1$. They were rotated along the circular track in the same direction as the animal when $0 < G < 1$ or in the opposite direction when $G > 1$. Every gain-manipulation session comprised four epochs. In Epoch 1 the animal ran 8–15 laps with stationary landmarks ($G = 1$). During Epoch 2, G was ramped linearly at a rate of 1/52 per lap until it reached its final value, $G_{final}$. Epoch 3 held G constant at $G_{final}$, and in Epoch 4 all landmarks were extinguished, leaving only a dim, non-polarizing ring for illumination. $G_{final}$ took the form of $1 \pm n/13$ ($n = 0, 1, 2, 3, 4\ldots$), so that positions in the laboratory and landmark frames coincided only once every 13 laps when $n > 0$. Each rat first completed one to three baseline sessions with $G = 1$; thereafter the gain was systematically altered in following sessions. Sessions with more extreme values (much more or less than $G_{final} = 1$) often showed landmark-control failure. Thus, to maximize the number of sessions that retained strong landmark control, more extreme values of $G_{final}$ were chosen progressively across days and were seldom repeated on consecutive sessions. Investigators were aware of the gain during data collection and analysis, and sample sizes were determined empirically without formal power calculations.

**Open-loop gain manipulation experiments**

To dissociate landmark motion from the animal's self-motion in some experiments, visual landmarks were controlled by a pre-recorded self-motion trajectory obtained from a different session. The reference trajectory (recorded as a ROS .bag file) contained the animal's angular position along the circular track as a function of time. During open-loop sessions, this trajectory was replayed in real time and used to control landmark motion via the same experiment gain (G) parameter used in closed-loop experiments. If the open-loop session duration outlasted the reference trajectory duration, the trajectory was looped from its beginning without interruption to provide continuous control of landmark position.

Each open-loop session followed a standardized gain protocol. Epoch 1 began with gain $G = 1$, during which landmarks were stationary. In Epoch 2, G was ramped from 1 to a final value, similar to closed-loop gain manipulation experiments. Subsequent epochs consisted of step changes ("jumps") to additional non-unity

gains. The set of gains always included at least one value > 1 and at least one value < 1. At non-unity gains, landmark position changed according to the replayed trajectory (scaled by G), such that landmarks could move even if the animal was stationary, consistent with the open-loop design. At the end of the session, landmarks were extinguished.

**Luminance manipulation experiments**

Landmarks and the background were implemented as separate OpenGL objects, allowing independent control of their luminance by scaling object intensities. Intensities were normalized to the projector's dynamic range (0–1). Landmark (LM) luminance took values 1.00 (High) and 0.55 (Low); background (BG) luminance took values 0.47 (High) and 0.01 (Low). For all contrast (LM–BG) combinations, LM luminance was slightly greater than BG luminance to avoid "negative contrast" conditions (i.e., landmarks appearing by virtue of being darker than the background).

During luminance manipulation blocks, landmarks were stationary (experiment gain G=1). Each session comprised fixed-length epochs of either 6 or 8 laps. Within a given epoch, LM and BG luminance were held constant. The four illumination conditions (2 LM luminance levels X 2 BG luminance levels) were presented in pseudorandom order. Across a session, the luminance conditions changed only at epoch boundaries, and each of the four conditions were presented at least three times.

At the end of the luminance epochs, the experiment gain was abruptly changed to an extreme value (i.e., much larger or smaller than 1), which induced landmark failure, allowing us to test the landmark anchoring strength for all cells, as described in the "Landmark-locking score" subsection of Methods.

**Brain region classification from single-cell physiological features**

*Pipeline training*

In cases where the histological brain-region assignment of a tetrode was ambiguous or infeasible due to histological imperfections, we applied a machine-learning (ML) pipeline to classify the recording region with high confidence, based on the firing properties of all neurons recorded on that tetrode (fig. S1B). We trained two separate binary classification pipelines: one to distinguish area 29e from other regions (MEC, PA, and PO), and one to distinguish presubiculum from other regions. For each pipeline, the "positive class" was defined as neurons assigned to the target region (area 29e or presubiculum), while the "negative class" included the remaining neurons assigned to all other regions.

The first layer of each pipeline comprised an XGBoost model (a boosted decision-tree algorithm; *83*) that performed brain-region classification using the physiological features of single neurons. Features included: (i) spike-waveform characteristics—the peak-aligned normalized waveform, spike width, and spike asymmetry (trough-to-peak amplitude ratio); (ii) theta-modulation measures—the mean resultant length (MRL) of spike–theta phases (*40*) and three metrics quantifying theta rhythmicity (*40*, *41*, *35*); (iii) firing-pattern features—mean firing rate, burst ratio (proportion of inter-spike intervals <8 ms), burst index and refractory period (*87*); and (iv) spike-autocorrelogram (ACG) properties—mean and mode lag of the ACG, and the power spectrum of the spike ACG (1–90 Hz). After eliminating highly correlated features in this set, a four-fold cross validation routine was employed for final feature selection and optimization of model hyperparameters on the training data. Classification probabilities from the resulting XGBoost model were then calibrated with Platt scaling (*88*, *89*) via an additional cross-validation procedure on the training data.

The second layer employed stacked generalization (*90*)—a meta-model that classified the brain region belonging to the multiple simultaneously recorded neurons from the same tetrode by combining their corresponding single-neuron probability outputs from the first classification layer. To ensure the meta-model was invariant to the presentation order of neurons, we first transformed single-neuron probabilities from the first layer into a permutation-invariant feature representation using symmetric aggregations. e.g., sum, sum-of-cosines (*91*). These permutation-invariant representations served as input to a logistic regression meta-model. We trained this meta-model with a synthetic dataset generated by random subsampling of the positive and negative classes in the training data for each pipeline (i.e., 29e vs. rest or PR vs. rest pipeline).

Hyperparameter optimization and Platt scaling-based probability calibration were performed by cross-validation schemes on this synthetic dataset.

The final layer applied independent confidence thresholds to the output probabilities of the meta-model in each pipeline for both positive ("29e" or "PR") and negative ("not 29e" or "not PR") class assignments—a technique known as classification with a reject option (*92*, *93*). Region assignments were accepted only when the output probability for either class exceeded its respective threshold; otherwise, no assignments were made to ensure that only high-confidence assignments were accepted. Thresholds for each pipeline were optimized via cross-validation on the training data: after meta-model fitting on each fold's training data, a range of threshold values was scanned on validation data to quantify both coverage (the fraction of accepted assignments) and accuracy among accepted assignments. Pareto optimization was then used to select threshold values that provided an optimal trade-off between these metrics for both positive and negative class assignments.

*Pipeline verification*

To assess pipeline performance on unseen data, we performed group-stratified, five-fold cross-validation (CV) on the histological ground-truth dataset. In each fold of this group-stratified CV, the dataset was split into training and test sets in a "tetrode-aware" fashion, i.e., by leaving out all data from selected tetrodes. This split ensured that neurons recorded on the same tetrode did not appear in both sets, preventing potential data leakage due to correlated nature of single units recorded on the same electrode. After training the pipeline, we evaluated it on the test set comprising neurons from withheld tetrodes. To simulate varying numbers of simultaneously recorded neurons, we generated synthetic test samples by randomly subsampling neurons from the held-out tetrodes. This approach allowed us to quantify sensitivity and specificity for identifying the respective positive class ("area 29e" or "PR") as a function of the number of neurons recorded simultaneously on a tetrode (fig. S1C). The accuracy and sensitivity of both 29e and PR models increased as the number of simultaneously recorded neurons on a given tetrode increased. Accordingly, to ensure that our models were only applied when their performance was sufficiently high (i.e., both sensitivity and specificity >= 0.85), we set minimum thresholds for the number of simultaneously recorded cells per tetrode. Specifically, we applied the 29e model to tetrodes with at least 5 neurons, and the PR model to tetrodes with at least 7 neurons. Both models were applied in a blinded fashion: region assignments of histologically ambiguous recording sites were finalized by the machine learning models prior to all data analyses.

## Power spectral analysis of LFP

*1/f background correction*

The wavelet transform was applied to each tetrode's LFP signal using Morlet wavelets spanning 1–140 Hz (Buzsáki Lab, GitHub: https://github.com/buzsakilab/buzcode). Instantaneous power was computed from the wavelet coefficients and averaged across the session. To isolate oscillatory power from the aperiodic background in each LFP power spectrum, we used the FOOOF algorithm (*94*) with the following parameters: knee mode, peak threshold 2.5, peak width 2–45 Hz, and max_n_peaks 4. Starting from the original spectrum, FOOOF was run iteratively as suggested in (*95*). In each iteration, FOOOF took the spectrum from the previous iteration as an input and fitted a parametric model for the oscillatory peaks and the aperiodic (1/f) background. Subtracting the identified peaks from this spectrum resulted in a refined spectrum, which was then used as input for the next iteration. This process continued until no oscillatory peaks greater than 1% above the aperiodic background remained, or until a maximum of ten iterations. The final peak-removed spectrum was then fit with a simple log–linear model to robustly estimate the aperiodic background. This fitted background was subtracted from the log-transformed original spectrum to obtain the 1/f-corrected (flattened) log power spectrum for each tetrode. Positive values in the 1/f-corrected log power spectrum indicate frequencies where the power exceeded the modeled aperiodic background, suggesting presence of oscillatory components, while negative values indicate frequencies without a detectable oscillatory excess.

*Cluster-based permutation testing of significant oscillatory power across frequencies*

To assess the statistical significance of oscillatory components across tetrodes within each brain region while controlling for familywise error, we used cluster-based permutation testing (*43*). For each

permutation, the sign of the entire 1/f-corrected log power spectrum from each tetrode was randomly flipped, preserving spectral structure at the tetrode level but disrupting any systematic region-level effects. At each frequency, a one-sample t-test was performed across tetrodes for both the observed and permuted values. Clusters were defined as contiguous frequencies with significant positive deviation from zero according to $p < 0.05$ (one-sided). The size of each observed cluster (calculated as the sum of t-statistics within the cluster) was then compared to the distribution of maximal cluster sizes from the permuted data, yielding permutation-corrected cluster-level p-values that control the familywise error rate and preserve spectral contiguity. Clusters with corrected $p < 0.05$ were considered significant.

*Mixed effects-model of theta- and gamma-band LFP power*

Average power in theta (6–10 Hz) and gamma (50–120 Hz) band were calculated from the 1/f-corrected log-power spectrum of each tetrode. We tested for regional differences in these band-limited powers by fitting linear mixed-effects models with region as a fixed effect and random intercepts for rat identity and rat-by-region interaction.

**Theta and gamma rhythmicity of single neurons**

Rhythmicity was assessed from power spectrum of each neuron's spike autocorrelogram as follows: The theta index was calculated as mean power in 6–10 Hz divided by mean power in 1–50 Hz (*40*), and the gamma index as mean power in 50–120 Hz divided by mean power in 5–250 Hz (*96*).

**Coupling of single neurons to LFP theta rhythm**

Each tetrode's LFP signal was band-pass filtered between 6–10 Hz (4$^{th}$ order Butterworth filter), and the Hilbert transform was applied to extract theta-band power and phase. For each neuron, theta phase from all tetrodes was circularly interpolated at spike times, and pairwise phase consistency (PPC) was computed for spike theta phase distribution of each tetrode using FieldTrip (*97*).The highest PPC obtained across tetrodes was used to quantify each neuron's coupling to LFP theta rhythm.

**Spatial tuning in the Dome**

A circular firing-rate map was created for each neuron to quantify its spatial tuning in the Dome when landmarks were stationary (i.e., experimental gain = 1). We assigned both the angular position of each spike and the animal's position at each behavioral time point to 36 angular bins (10° per bin) spanning all locations across the circular track. We then computed the firing rate in each bin by dividing the number of spikes by the amount of time spent in that bin. The resulting rate maps were smoothed with a circular Gaussian kernel ($\sigma = 15°$). The smoothed circular rate map was then used to calculate each neuron's Skaggs' spatial information (SI) score (in bits per spike) (*32*):

$$\mathrm{SI} = \sum_i p_i \frac{r_i}{r} \log_2 \frac{r_i}{r}$$

where $p_i$ is the fraction of total session time the animal spent in $i^{th}$ angular bin, $r_i$ is the neuron's firing in the same bin, and $r$ is the neuron's overall mean firing rate;the summation is over the bins, $i = 1, \ldots, 36$. Because this score (originally developed for 2D firing-rate maps) can produce both false-positive and false-negative errors when applied to data from 1D circular tracks (*98*), we also quantified spatial tuning using two alternative SI metrics, the Olypher SI score and the mutual SI score, defined below.

The Olypher SI score defined as the maximum Kullback-Leibler divergence between the neuron's spike count distribution at any given position and its overall spike count distribution (*99*):

$$\text{Olypher SI} = \max_i \sum_{k \geq 0} P_i(k) \log_2 \frac{P_i(k)}{P(k)}$$

Here, $P_i(k)$ is the probability of observing k spikes within a 100 ms time-segment when the animal occupies positional bin $i$, and $P(k)$ is the marginal probability of observing k spikes, regardless of the animal's position.

The mutual SI score defined as the mutual information between the neuron's spike count and the animal's position (*100*, *101*):

$$\text{Mutual SI} = \sum_{i,k\geq 0} P(k,i)\log_2 \frac{P(k,i)}{P(k)P(i)}$$

Here, $P(i)$ is the marginal probability of the animal occupying the positional bin i within a 100 ms time segment, independent of the number of spikes, and $P(k,i)$ is the joint probability of observing k spikes and the animal being in positional bin i within the same time segment.

To assess significance of each SI score for each neuron, we generated a null distribution by circularly shifting the neuron's spike train relative to behavioral data by a randomly chosen time offset (between 25 and T – 25 seconds, where T is the total duration of the first experimental epoch) and recalculating the SI scores 100 times. A neuron was considered significantly spatially tuned, if at least one of its observed SIs exceeded the 99$^{th}$ percentile of the respective shuffled SI distribution.

**Landmark-selective firing modulation in the Dome**

*Z-index*

The circular firing-rate map was linearly interpolated to 1° resolution and normalized to z-scores. For each landmark location, we computed the average z-scored firing rate within a ±12° radius around the landmark. The same calculation was performed for midpoint locations halfway between each pair of adjacent landmarks. The landmark selectivity z-index was then defined as the absolute difference between the average z-scored firing rate around the landmark locations and that around the midpoints.

*Local similarity index*

A sector was defined around each landmark by identifying the arc spanning from the midpoint between that landmark and its preceding neighbor to the midpoint between it and its following neighbor. After linearly interpolating the neuron's circular firing-rate map to 1° resolution, we extracted the portion of the firing-rate map lying within each sector. For each pair of landmarks, the Pearson correlation coefficient was computed between the local firing-rate profiles, using only the angular range shared by both sectors (i.e., their intersection). This shared range varied from as little as ±20° up to ±60° for different pairs, depending on the number and spatial arrangement of landmarks within the Dome (Fig. 1B). The local similarity index for each neuron was then defined as the average of all such pairwise correlations across landmark pairs.

**Landmark-locking score**

For each neuron, we computed a lapwise firing-rate map in the landmark frame by binning spikes and the animal's behavioral data within each lap into 10° angular bins, dividing the spike count in each bin by the time spent in that bin, and smoothing with a Gaussian kernel with σ = 15°. Using the last 12 laps of this firing-rate map, we calculated the spatial autocorrelation function for spatial lags between 0 and 10 laps. Neurons with stable lapwise firing exhibited autocorrelation functions with prominent oscillations at integer-lap periods, indicating consistent periodicity across laps (Fig. 2; fig. S2), whereas neurons that broke free from landmarks displayed autocorrelation functions with weak or irregular oscillatory structure (Fig. 2; fig. S2).

To quantify the lap-to-lap periodicity of each neuron's autocorrelation function, we computed all possible pairwise Pearson correlations among the circularly rotated versions of the autocorrelation function at full-lap lags (rotations between 3 and 8 laps, in 1-lap steps), as well as all possible correlations between these full-lap rotated versions and the half-lap rotated versions (rotations from 3.5 to 7.5 laps, in 1-lap steps). Neurons with stable lapwise periodicity are expected to show higher correlations among the full-lap rotations than between the full-lap and half-lap groups.

Accordingly, the landmark-locking score was defined as the normalized difference: the sum of all Pearson correlations within the full-lap rotation group minus the sum of all correlations between the full-lap and half-lap groups, divided by the total number of correlations (Fig. 2; fig. S2). A score close to 1 indicates strong,

consistent periodicity at the lap timescale, while a score near zero indicates little or no periodic firing structure.

**Unsupervised identification of LM-control and LM-failure session types**

To identify session-wise differences in landmark control over neuronal populations, we first computed the average landmark-locking score across all recorded neurons in each session. Sessions were then clustered based on their respective average landmark-locking score using an enhanced density-based clustering algorithm (*dbscan* in MATLAB) procedure that set MinPts = 4 and automatically tuned the neighborhood radius ε through k-distance heuristic with k = MinPts (*102*). Briefly, for each session, the distance between its respective average landmark-locking score and that of its $4^{th}$-nearest neighbor session was measured. The neighborhood radius ε was set as the distance corresponding to the knee point of the k-distance graph obtained from these distances. DBSCAN were ran with these ε and MinPts. Any points labeled as noise (i.e., left out of clustering) were assigned to the cluster whose centroid was nearest.

**Multi-unit responses to landmark removal**

Multi-unit, unclustered spike trains from each tetrode were binned at 2.5 ms resolution, and the resulting temporal firing rates were smoothed with a 125 ms moving boxcar filter. To quantify the neural response to landmark removal, we aligned the smoothed firing rates to the time of landmark extinction and extracted a window from –0.375 to +0.375 seconds relative to this time for each session. An Epanechnikov kernel density estimate (KDE) was fitted to the pre-event (time < 0) firing rate distribution to serve as the baseline; this kernel was chosen for its optimal mean square error properties, ensuring robust nonparametric estimation (*103*).

To assess the statistical rarity, or "surprise," of post-event changes in firing rate, we computed both a right-tail probability (the likelihood that the observed firing rate exceeded the baseline) and a left-tail probability (the likelihood that it was lower) at each post-event time point. These probabilities were log-transformed and smoothed with a 100 ms moving window. For each time point in the post-event period, we determined the tail direction (increase or decrease) with the largest deviation by subtracting the corresponding post-event log-tail probability from the minimum log-tail probability observed pre-event in the same direction (i.e., the most "surprising" baseline value). This difference was then normalized by the sum of their absolute values, ensuring that extreme increases and decreases in firing were treated symmetrically. The maximal normalized deviation observed at any post-event time—the greatest "surprise"—was defined as the landmark removal response score for each tetrode.

**Single neuron responses to landmark and background luminance manipulations**

Lapwise firing rate maps for each neuron were computed as before (see Landmark-locking score section).

<u>*Luminance sensitivity analysis*</u>

We fitted a two-way ANOVA to each neuron's lapwise peak firing rates, using lapwise landmark luminance (LM) and background luminance (BG) as factors. The effect size for each factor X ∈ {LM, BG} was quantified by

$$\eta_X^2 = \frac{SS_X}{SS_{Total}},$$

where $SS_X$ denotes the sum of the squares in peak firing rate explained by the variation in the factor *X* and $SS_{Total}$ denotes the total sum of squares in the peak firing rates. Because these luminance factors were independently manipulated and uncorrelated, we quantified their combined overall effect size as the sum $\eta_{overall}^2 = \eta_{LM}^2 + \eta_{BG}^2$.

Contrast analysis

Although landmark and background luminance were independently manipulated by a two-factorial design, the resulting contrast (C=LM – BG) and total luminance (TL=LM + BG) values were linearly dependent and did not obey a fully factorial design, precluding the use of ANOVA to analyze firing-rate dependence on (C,

TL). Accordingly, a linear model was fit with C and TL as predictors and each neuron's peak firing rates as the dependent variable. The unique contribution of each predictor X ∈ {C, TL} was quantified using partial $R^2$:

$$R^2_{\text{partial}}(X) = \frac{(\text{SSE}_{\text{reduced}} - \text{SSE}_{\text{full}})}{\text{SSE}_{\text{reduced}}} = \frac{(R^2_{\text{full}} - R^2_{\text{reduced}})}{(1 - R^2_{\text{reduced}})}.$$

Here, SSE is the sum of squared errors, "full" refers to the model with both predictors, and "reduced" refers to the model with X removed. Partial $R^2$ thus quantifies the additional variance in firing rate explained by a predictor, after accounting for the presence of the other, even when the predictors are correlated.

**Allocentric place tuning in the open arena**

A two-dimensional (2D) spatial firing rate map was created for each neuron by first binning the (x, y) coordinates of its spike train and the animal's behavioral trajectory into 3.5 x 3.5 $cm^2$ bins, and then dividing the number of spikes per bin by the amount of time spent in that bin. The resulting rate maps were smoothed with a 2D gaussian kernel (s = 3.5 cm in both x and y directions). The Skaggs spatial information (SI) score of each neuron was then calculated in bits per spike from its smoothed rate map as above.

*Testing significance and stability*

To generate a null distribution, we circularly shifted each neuron's spike train by a randomly chosen time offset (between 25 and T – 25 seconds, where T is the total session duration), recalculating the SI score for 100 times. We also quantified the tuning stability of each neuron by calculating the Pearson correlation between its 2D rate maps from the first and second halves of the session. A neuron was considered significantly tuned to place, if its observed SI exceeded the 99$^{th}$ percentile of its shuffled SI distribution and its split-session stability exceeded 0.5.

**Allocentric head-direction tuning in the open arena**

The animal's head direction (HD) was binned into 90 angular bins (4° width), and the firing rate in each bin was computed by dividing the number of spikes by the time spent in that HD bin. Tuning curves were then smoothed with a circular Gaussian kernel (σ = 4°). We calculated the mean resultant length (MRL) of the resulting smoothed polar tuning curve as a measure of HD tuning strength in allocentric coordinates.

*Testing significance and stability*

The uniformity of the smoothed HD tuning curve was tested using the Rayleigh test. We also generated a null distribution for statistical assessment by using the same circular time-shifting procedure as for place tuning: spike times were circularly shifted relative to the behavioral HD time series by a randomly chosen time offset (between 25 seconds and T−25 seconds, where T is the session duration), and the MRL was recalculated 100 times. For tuning stability, we computed the difference in mean angular direction between the first and second halves of the session. A neuron was considered significantly tuned to allocentric HD if the p-value from the Rayleigh test of uniformity was < 0.01, if its observed MRL exceeded the 99th percentile of the shuffled distribution, and if the split-session mean directional difference was less than 45° as previously used (*75*).

*Dissociating head-direction and place tuning in allocentric coordinates*

To verify that our findings on regional differences in place and HD tuning scores were not confounded by differences in behavioral sampling, we disentangled allocentric place and HD tuning of neurons by using a Poisson generalized linear model (GLM), as in previous work (*74*, *104*). Briefly, each neuron's spike train was binned into $dt$ = 125 ms segments. For each segment $t_i$, the expected spike count was modeled as

$$\lambda(t_i) = dt \cdot \exp\left[X_p(t_i)\, w_p + X_h(t_i) w_h\right],$$

where $X_p$ and $X_h$ are one-hot encoded row vectors representing, respectively, the animal's (x,y) position (in 7 x 7 $cm^2$ bins) and HD (in 8° angular bins) at the center of that segment. The column vectors $w_p$ and $w_h$ denote the predictive weights for position and HD (analogous to tuning curves). Fitting of these weights was

performed by maximizing an objective function that combined the Poisson log-likelihood of the observed spike counts with a smoothing penalty to discourage large weight differences between adjacent bins, as previously described (*74*, *104*). Optimization was performed using the *fminunc* search routine in MATLAB, aided by analytically computed gradients. Using the optimized weights $\widehat{w}_p$ and $\widehat{w}_h$ for each neuron, we constructed a 2D spatial firing rate map and a 1D HD tuning curve, each marginalized over the other behavioral variable:

$$r_p(X_p) = \exp[X_p\ \widehat{w}_p]\frac{1}{N_h}\sum_{X_h}\exp[X_h\ \widehat{w}_h]$$

$$r_h(X_h) = \exp[X_h\ \widehat{w}_h]\frac{1}{N_p}\sum_{X_p}\exp[X_p\ \widehat{w}_p],$$

Here, $N_h = 45$ (the number of 8° HD bins) and $N_p = 400$ (the number of 7 x 7 cm$^2$ positional bins). These marginal rate maps were then used to calculate the SI (place-tuning score) and MRL (HD-tuning score) for each neuron as described above.

**Egocentric head-direction tuning in the open arena**

Because egocentric coding can be anchored to any arbitrary point in an environment, quantifying a neuron's egocentric tuning curve necessitates an exhaustive search to determine its optimal anchor point. In contrast, allocentric coding is characterized by a single possible tuning curve per neuron, requiring no anchor-point search. If one chooses the egocentric anchor point producing the most specific tuning curve, this asymmetry creates a bias in favor of the egocentric model over the allocentric model when evaluating a neuron's preferred frame of reference (*54*). Model selection metrics criteria (e.g., AIC/BIC) partly compensate for the extra anchor point parameter this bias but rely on assumptions that poorly capture the complexity of the anchor search and can still reward overfitting. More rigorous controls (e.g., surrogate tests) would help but are computationally prohibitive because each surrogate demands a new exhaustive anchor search. To circumvent these issues, we developed an egocentric vector-field score, as follows.

We constructed a 2D HD vector field for each neuron by dividing the arena into a uniform 9 × 9 grid of (x, y) locations. At each grid location, we began with a spatial bin size of 15 × 15 cm² centered at that point. We identified all time points when the animal's position fell within the bin and assigned the corresponding HDs to 12 angular bins (30° each). If any angular bin at a grid location had less than 0.2 seconds of occupancy, the spatial bin size at that location was increased iteratively until every HD bin reached this sampling threshold.

For the local HD tuning curve constructed at each (x, y) grid location, we computed its complex-valued first harmonic vector,

$$v_{hd} = \sum_{k=1}^{12} FR_k e^{i\theta_k},$$

where $FR_k$ is the firing rate in HD bin *k* associated with the angle $\theta_k$. Note that the angle of this vector is the same as the mean angular direction of the local HD tuning curve, while its magnitude is equal to the product of summed firing rate within the local HD tuning curve and the MRL of the local HD-tuning curve. This vector is equal to the first (i.e., fundamental) Fourier component of the local HD-tuning curve, which defines the single sinusoid that best fits the tuning curve in the least-squares sense. The collection of these vectors across all grid locations comprised the 2D HD vector field for the neuron.

Egocentric vector field score

To quantify egocentric tuning without specifying an anchor point, we analyzed the spatial derivatives of each neuron's local HD vectors (i.e., how these vectors vary along the x and y axes of the arena). Specifically, we computed two classical vector calculus measures, *curl* and *divergence,* for each spatial bin (x, y) of the open arena (fig. S8).

The *Curl* of a vector field captures local rotational (swirling) structure of the HD vectors:

$$\mathrm{curl}(x,y) \triangleq \frac{\partial Q(x,y)}{\partial x} - \frac{\partial P(x,y)}{\partial y}$$

The *Divergence* captures the local inward/outward flow structure of the HD vectors:

$$\mathrm{div}(x,y) \triangleq \frac{\partial P(x,y)}{\partial x} + \frac{\partial Q(x,y)}{\partial y}$$

These partial derivatives were estimated using centered-difference approximations between bin centers. Neurons with allocentric HD tuning, characterized by parallel vectors throughout the arena, exhibited near-zero curl and divergence everywhere, as well as neurons lacking any systematic HD tuning. By contrast, neurons with strong egocentric tuning generated spatially consistent, high curl and/or divergence values (fig. S8).

We combined the curl and divergence values at each spatial bin into a 2D vector. The curl was assigned as the horizontal component of this vector, whereas the divergence was assigned as its vertical component. This approach merged the separate curl and divergence fields into a new vector field that captures both rotational and flow characteristics of the preferred HD throughout the arena.

We then calculated the Egocentric Vector Field (EVF) score as the mean resultant length (MRL) of all divergence-curl vectors across the arena. This score ranges from 0 to 1, where values close to 0 indicate random or inconsistent curl/divergence patterns, whereas values close to 1 indicate highly consistent patterns characteristic of strong egocentric tuning.

*Generalized linear models for egocentric versus allocentric preference*

To dissociate each HD-tuned neuron's preferred frame of reference (egocentric vs. allocentric), we used a Poisson GLM framework (*54*, *74*, *75*). Specifically, for each neuron, we fitted two separate GLMs to its spike train, binned into 125 ms time segments: one GLM used allocentric head direction (HD) as a predictor, while the other used egocentric HD, computed relative to the (x, y) coordinates of a candidate anchor point. For the egocentric model, the optimal anchor point was identified by grid search: the GLM was re-fit at each candidate anchor location spaced every 5 cm across the arena in both x and y directions, and the location yielding the largest log-likelihood was selected. To compare the predictive performance of the two models while accounting for the increased complexity of the egocentric GLM ($K_{ego} = 2$ additional parameters corresponding to the anchor–point optimization), we calculated the difference in Bayesian information criterion

$$\Delta\mathrm{BIC} = 2\ln\hat{L}_{allo} - 2\ln\hat{L}_{ego} + K_{ego}\ln N,$$

where $\hat{L}_{ego}$, $\hat{L}_{allo}$ are the optimal log-likelihoods of GLMs with egocentric HD and allocentric HD variables, respectively, and N is the number of bins (time segments). A positive $\Delta BIC$ suggests that the allocentric model provides a better fit, whereas a negative $\Delta BIC$ suggests a better fit for the egocentric model.

*Testing significance and stability*

We generated two null distributions for the anchor-free EVF score of each neuron. Similar to other spatial tuning measures, one null distribution was obtained by circularly shifting the neuron's spike train relative to the animal's behavioral data by a single, randomly chosen time offset (between 25 seconds and T−25 seconds, where TT is the total session duration), and recomputing the EVF score 100 times. The second null distribution was generated by disrupting the relationship between position and head-direction vectors in the HD vector field 1,000 times: for each iteration, we circularly translated the entire HD vector field along both the x and y axes by random amounts and then recomputed the EVF score.

For each neuron, we also constructed a polar head-direction tuning curve referenced to the optimal anchor point identified by the GLM protocol, using the same bin size and smoothing as for the allocentric HD tuning curve. A neuron was considered significantly tuned to egocentric HD if its observed EVF score exceeded the 99th percentile of both null distributions and the split-session mean directional difference was less than 45°.

**LFP-LFP coherence**

LFP signals were segmented into 1-second candidate windows with 95% overlap (0.05 s step size). These windows were evaluated sequentially from the start of the recording. Any window in which the animal's velocity was below 4 cm/s for more than 25% of the time, or where the maximum velocity did not reach 10 cm/s, was discarded. If a window satisfied both speed criteria, it was retained for analysis. Other candidate windows that overlapped in time with this accepted window were excluded from further consideration. This process was repeated iteratively until no windows remained, resulting in a set of non-overlapping, speed filtered 1-second windows for the subsequent spectral analysis.

Within each retained window, LFP signals were determined. Spectral analysis was performed using the multi-taper Fourier transform with Slepian (DPSS) tapers via FieldTrip (*97*) for frequencies between 0 and 140 Hz with a frequency resolution of 1 Hz. For frequencies below 25 Hz, three tapers were used (yielding a frequency smoothing half-width of 2 Hz); for frequencies above 25 Hz, six tapers were used (smoothing half-width 3.5 Hz). For each window and frequency, the complex-valued cross-spectral density (CSD) matrix was computed from all simultaneously recorded tetrode pairs.

*Baseline analysis*

For each tetrode pair, we estimated the complex coherency ($C$) based on averaged bivariate CSD matrices across all retained, non-overlapping windows within the initial stationary epoch. The resulting estimate was biased due to a limited number of windows and has a variable variance that again depends on the number of windows. Under the null hypothesis of zero coherence, both bias and variance have analytically known forms (*105*, *106*) which can be used for bias correction and variance normalization as follows:

$$coh = \frac{\mathrm{C}}{|\mathrm{C}|}\sqrt{\frac{|C|^2 - \frac{1}{\nu - 2}}{\frac{1}{\nu - 2}}}$$

Here, ν denotes the degrees of freedom (equal to twice the product of number of tapers and number of windows), $C$ is the estimated, raw coherency, and *coh* is bias-corrected, variance normalized coherency estimate. To capture true (i.e., time-lagged, non-spurious) coupling between LFP signals that is insensitive to instantaneous, volume-conduction like effects (*107*), we focused on the imaginary part of this corrected coherency, which we further normalized it by the real component and then Fisher z-transformed as follows:

$$\mathrm{zCoh} = \tanh^{-1}\left(\frac{|\mathrm{Im(coh)}|}{\sqrt{1 - \mathrm{Re(coh)}^2}}\right)$$

We refer to the resulting quantity as the z-imaginary coherence spectrum. This coherence spectrum at the single tetrode-pair level was then averaged across all 29e-MEC tetrode pairs, yielding a region pair-level average imaginary coherence spectrum.

To assess significance of the average z-imaginary coherence spectra observed at the region-pair level, we used a hierarchical, cluster-based permutation test (*43*, *108*). For each 29e-MEC tetrode pair, a null distribution of CSD values was generated by randomly flipping the sign of the imaginary component of the CSDs from retained windows, then recalculating the z-imaginary coherence spectrum after averaging the sign-flipped CSDs. This permutation was repeated 1,000 times per tetrode pair. To generate a group-level (region pair) null, we randomly sampled from the resulting individual tetrode-pair nulls 5,000 times) and calculated, for each random sampling, the average z-imaginary coherence spectra. The observed region pair-level z-imaginary coherence at a frequency was considered significant if it exceeded the 95$^{th}$ percentile of the permutation group-level null distribution. Clusters were defined as contiguous frequencies that are significant with no gap. To control the familywise error rate of the comparisons across the whole frequency spectrum while respecting spectral contiguity, the cluster size (sum of coherence values within the cluster) was compared to the distribution of maximal cluster sizes from the group-level permutations. Clusters with corrected $p < 0.05$ were considered significant.

*Initial epoch-to-final epoch coherence change*

For each tetrode pair, we computed the z-imaginary coherence spectrum in the initial and final experimental epochs after averaging their bivariate CSD matrices across accepted 1-second, non-overlapping windows from that epoch. For each frequency band—theta (6–10 Hz) and gamma (50–120 Hz)—we then identified

the frequency bin with the maximum z-imaginary coherence, and used this value as the representative coherence for that band in a given epoch. The normalized change in coherence for each band was then calculated as (final – initial)/(final + initial).

**LFP-LFP Granger causality**

For Granger causality analysis, LFP signals were segmented into candidate windows of 3 seconds with 98% overlap (0.05 s step size). As in previous analyses, windows were speed filtered, except that for Granger analysis, we required the velocity to exceed 4 cm/s for more than 50% of the window (rather than 75%) because of larger window size.

Within each accepted 3-second window, LFP signals were detrended and transformed to the frequency domain using a multi-taper Fourier transform with Slepian (DPSS) tapers (0.4 Hz resolution) via FieldTrip (*97*). For low frequencies (<20 Hz), the entire 3-second window was used. For higher frequencies (≥20 Hz), each 3-second window was divided into two equal, non-overlapping 1.5-second segments; spectral analysis was performed separately for each segment to improve robustness against nonstationarity of LFP signals in the higher frequencies, and the results were subsequently averaged. The combined spectra from both frequency ranges yielded a full-frequency spectral representation for each window.

Granger causalities between each 29e–MEC tetrode pair was computed for every accepted 3-second window using the full-frequency spectral representations, conditioning (partializing) on all other simultaneously recorded tetrodes to remove indirect and common source effects and thereby isolate direct influences (*44*, *109*). To smooth the resulting Granger causality spectra, a moving average filter spanning 2 frequency bins was applied in the frequency domain.

*Baseline analysis*

For each 29e–MEC tetrode pair, the smoothed Granger causality spectra from all accepted windows in the initial stationary epoch were averaged, yielding two mean spectra per pair: one for the 29e→MEC direction ($GC_{29e\rightarrow MEC}$ ), and one for the reciprocal MEC→29e direction ($GC_{MEC\rightarrow 29e}$). The directed asymmetry index (DAI) was then calculated for each pair as the normalized difference between the two:

$$\mathrm{DAI} = \frac{GC_{29e\rightarrow MEC} - GC_{MEC\rightarrow 29e}}{GC_{29e\rightarrow MEC} + GC_{MEC\rightarrow 29e}}.$$

To assess the statistical significance of DAI values across tetrode pairs, we used a cluster-based permutation approach. At each frequency, a one-sample t-test determined whether DAI values across tetrode pairs for a region pair significantly deviated from zero. To control the familywise error rate, null distributions of maximal cluster size were generated by randomly flipping the region labels of tetrode pairs and repeating the t-test procedure for 1000 permutations. Clusters were defined as contiguous frequencies with a significant positive deviation from zero ($p < 0.05$, one-sided). For each observed cluster, the sum of t-statistics within the cluster was compared to the permutation distribution to generate cluster-level, permutation-corrected p-values. Clusters with corrected $p < 0.05$ were considered significant.

*Initial epoch-to-final epoch Granger Causality and DAI change*

For each tetrode pair, we calculated the average Granger Causality spectra for both directions (i.e., 29e→MEC and MEC→29e) during the initial and final experimental epochs by averaging the Granger causality spectra from all accepted windows in each of these epochs. For each direction and each frequency band—theta (6–10 Hz) and gamma (50–120 Hz)—we then identified the frequency bin with the maximum Granger causality. The normalized change in coherence for each band was then calculated as (final – initial)/(final + initial).

*Cross correlation analyses between ongoing changes in DAI, coherence, and relative landmark-control strength*

The 1-second, speed-filtered windows included in spectral analysis were distributed unevenly relative to the animal's unwrapped position in the landmark frame of reference, with consecutive windows typically separated by 30–60 degrees and covering the full range of unwrapped landmark-frame positions within each session. To investigate the correlation between ongoing changes in landmark control strength and LFP–LFP coherence during each session, we resampled the cross-spectral density (CSD) measurements from these

non-uniform windows onto a uniform spatial grid (90-degree spacing) in the reference frame of rotating landmarks, using local linear kernel regression (Gaussian kernel, 135-degree standard deviation). From these spatially uniform, resampled CSDs, we computed the z-imaginary coherence spectrum at all grid positions, yielding position-resolved coherence values.

Landmark control strength was quantified at the same spatial resolution. For each 90-degree bin, we calculated the mean firing rates of all spatially tuned neurons (excluding those from 29e) and constructed a population vector (PV). The full-lap PV correlation at each bin was calculated as the average Pearson correlation between the PV at that position and those from the same location one and two laps earlier (offsets of 360 and 720 degrees). The half-lap PV correlation was calculated as the average correlation between the PV at that position and PVs from bins 180 and 540 degrees earlier. The landmark control-strength score at each bin was then taken as half the difference between the full-lap and half-lap PV correlations, providing a measure of landmark-anchored lap-to-lap consistency.

For each tetrode pair in each session, we then calculated the Pearson correlation coefficient between the landmark control-strength scores and the z-imaginary coherence spectrum at every frequency across spatial bins. For both the theta (6–10 Hz) and gamma (50–120 Hz) bands, we identified the maximum correlation within each band and used these as the representative values for that tetrode pair and session. To assess statistical significance, we generated null distributions for each session by circularly shuffled the landmark control-strength trajectory by a random number of bins (between 12 [four laps] and N–12, with N the total number of spatial bins, typically >200), and repeating the correlation analysis for 500 iterations. For each shuffled trajectory, we recalculated its correlations with the original z-imaginary coherence spectrum at all frequencies and again recorded the maximum values in the theta and gamma bands to construct null distributions for each. Observed theta- and gamma-band correlation values of a tetrode pair were considered significant if they exceeded the 95th percentile of their respective null distributions.

We also assessed the significance of the positive relationship between trajectories of landmark control strength and theta- or gamma-band coherence across all sessions, animals, and tetrode pairs for each region pair, using two linear mixed-effects (LME) models—one for theta-band coherence and one for gamma-band coherence. In each model, the position-resolved landmark control-strength scores served as the predictor variable, while coherence within the respective band served as the outcome variable. Random intercepts were included for rat identity and tetrode pair to account for repeated measures within subjects and electrode combinations. Model parameters and statistical significance were estimated using restricted maximum likelihood (REML) in MATLAB *fitlme* function.

## Spike-LFP coupling

*Baseline analysis*

We computed the spectrum of pairwise phase consistency (PPC) values from 1 to 140 Hz (with 1 Hz frequency resolution) for each neuron relative to each available LFP channel, using its spikes during the initial epoch with stationary landmarks in a session. For both the theta and gamma bands, we searched across all available LFP channels and all frequencies within each band, identifying the channel and frequency combination at which the PPC was maximal. This maximum PPC value was then used as the representative measure for that band for each tetrode pair and session.

## Identification of monosynaptic excitatory connections

We ran the GLMCC algorithm (*110*) in likelihood-ratio (LR) mode (*111*), which returned a directed connectivity matrix among all simultaneously recorded neurons in each session. A neuron was classified as excitatory if ≥ 80% of its outgoing weights were positive. Monosynaptic connections of excitatory neurons were then defined as outgoing edges with weights exceeding a threshold of 1, as suggested in (*110*).

## Acknowledgments

This work was supported by the Johns Hopkins Kavli Discovery Institute through a distinguished postdoctoral fellowship (G.S.) and distinguished graduate student fellowship (B.K.), as well as by the National Institutes of Health grants R01 NS102537 (N.J.C., J.J.K.), R01 MH118926 (J.J.K., N.J.C.) and a Biomedical Engineering Training Program Grant 5T32GM007057 (B.K.). We thank Rahul Jakati, Ravikrishnan Jayakumar, Shahin Lashkari, Francesco Savelli, Manu Madhav, Katelan Balkissoon, Bethel Gebreselassie and Makenna Dixon.

# Supplementary Figures

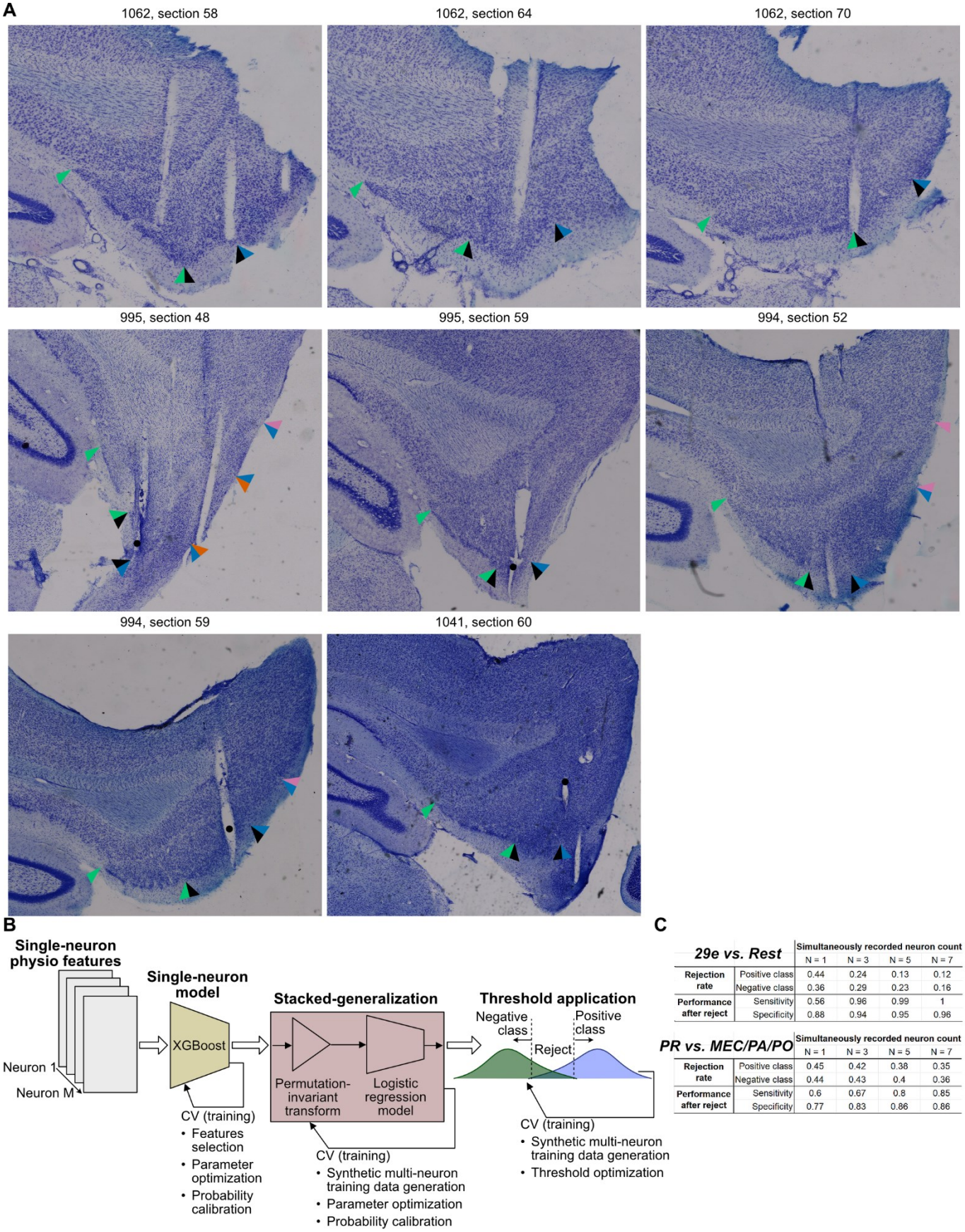


| 29e vs. Rest | | Simultaneously recorded neuron count | | | |
|---|---|---|---|---|---|
| | | N = 1 | N = 3 | N = 5 | N = 7 |
| Rejection rate | Positive class | 0.44 | 0.24 | 0.13 | 0.12 |
| | Negative class | 0.36 | 0.29 | 0.23 | 0.16 |
| Performance after reject | Sensitivity | 0.56 | 0.96 | 0.99 | 1 |
| | Specificity | 0.88 | 0.94 | 0.95 | 0.96 |

| PR vs. MEC/PA/PO | | Simultaneously recorded neuron count | | | |
|---|---|---|---|---|---|
| | | N = 1 | N = 3 | N = 5 | N = 7 |
| Rejection rate | Positive class | 0.45 | 0.42 | 0.38 | 0.35 |
| | Negative class | 0.44 | 0.43 | 0.4 | 0.36 |
| Performance after reject | Sensitivity | 0.6 | 0.67 | 0.8 | 0.85 |
| | Specificity | 0.77 | 0.83 | 0.86 | 0.86 |

**Fig. S1.** Additional histological sections showing recording sites in area 29e and machine learning pipeline for brain-region assignment from single-cell physiology and its performance metrics.
**(A)** Colored arrowheads indicate boundaries between areas following the same color scheme as Fig. 1A: area 29e (black), MEC

(orange), PA (blue), PO (pink) and PR (green). Top row: Three sections from Rat 1062. Due to tissue detachment in the lateral posterior region during sectioning, tetrode tracks could not be individually identified histologically and assigned to recordings. Regional assignments (29e or PR) were determined using a machine learning classification model. Sections 58 and 70 show tetrode locations at the ambiguous 29e/PA border, while section 64 shows a tetrode unambiguously located within area 29e. Middle row: sections from Rats 995 and 994. Rat 995, sections 48 and 59 show tetrode tracks within area 29e. Rat 994, section 52 shows a reference tetrode in area 29e. Bottom row: Rat 994, section 59 shows a tetrode track in area 29e. Rat 1041, section 60 shows a histologically ambiguous tetrode track assigned to the 29e/PA border, subsequently classified as area 29e using the machine learning model.

**(B)** Model architecture. When histology was ambiguous, we used a three-stage classifier trained as two separate one-vs-rest models (29e vs. rest and PR vs. rest). First, an XGBoost classifier used each neuron's physiological features to estimate the probability that it belonged to the target region. Next, we aggregated evidence across all neurons simultaneously recorded on the same tetrode by transforming them into a permutation-invariant representation, which was passed through a logistic-regression "meta-model" to obtain a tetrode-level probability estimate. Class-specific confidence thresholds were applied to the tetrode-level probabilities to assign either the positive (e.g., 29e) or negative (e.g., not 29e) label only when the corresponding probability exceeded its threshold; otherwise, we made no assignment (reject).

**(C)** Cross-validated performance for tetrode-stratified fivefold cross-validation and associated rejection rates. For each classifier (29e vs. rest and PR vs. rest), the rejection rate quantifies the fraction of samples that were not assigned. For accepted (confident) samples, sensitivity (true positive rate) and specificity (true negative rate) are reported in the table. As the number of simultaneously recorded cells on a tetrode increased, the rejection rate decreased, and sensitivity and specificity increased for both the 29e and PR models. Accordingly, the 29e vs. rest and PR vs. rest models were applied when there were more than 5 and 7 simultaneously recorded cells on a tetrode, respectively.

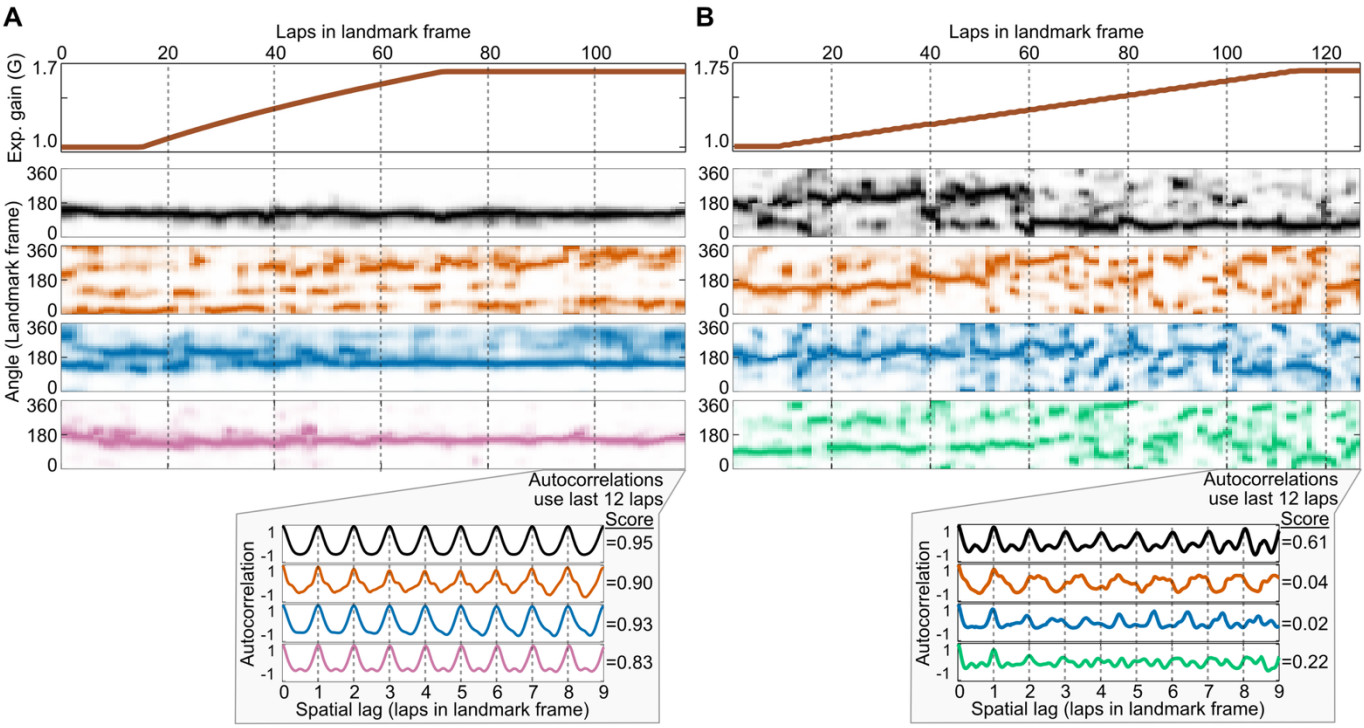


**Fig. S2.** More examples illustrating landmark anchoring in 29e relative to other regions and the autocorrelation-based landmark-locking score. Figure organization and panels are similar to Fig. 2D, E.

**(A)** An *LM-control* session in which spatially tuned neurons remain anchored to the rotating landmarks. Brown trace in the top panel shows the experimental gain protocol (gain = 1 at baseline, then ramped to a higher/lower target and held there for 10-30 laps). Middle panel firing rate of simultaneously recorded neurons across laps in the landmark reference frame (same format as in Fig. 2D, E). Neurons fire at fixed angles relative to landmarks throughout the session, producing stationary bands of firing rates in the landmark frame. Bottom shows the spatial autocorrelograms of the last 12 laps for example neurons. Clear peaks indicate strong 1-lap periodicity; the accompanying score quantifies this periodicity (see "landmark-locking score" in Methods).

**(B)** An *LM-failur*e session in which most spatially tuned neurons from regions, other than 29e lose landmark anchoring. Conventions as in (A). Around lap 65-75, firing fields of neurons recorded outside 29e started to drift in the landmark frame, yielding autocorrelograms that are not lap-to-lap periodic and exhibiting low landmark-locking scores. By contrast, a considerable subset of 29e neurons (example in black) remained locked to landmarks. Together, (A–B) illustrate how landmark-relative anchoring of firing fields (or its loss) is captured by the autocorrelation-based score.

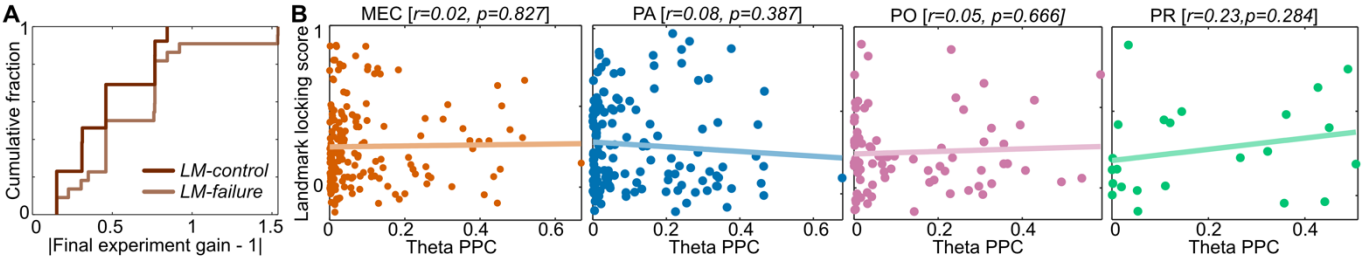


**Fig. S3.** Dependence of session types on experiment gain (panel A) and the relationship between spike-LFP theta phase coupling and the landmark-locking score (panel B).
**(A)** A larger fraction of LM-failure sessions occurred when the final value of the experimental gain was more extreme (i.e., much higher or lower than 1). The median value of the absolute difference between the final value of the experimental gain and 1 was higher in *LM-failure* sessions (median [IQR] = 0.61 [0.46-0.76]) than in *LM-control* sessions (0.45 [0.27-0.76]). This difference between session types was, however, not statistically significant (Wilcoxon rank-sum test: $Z = -1.2$, $p = 0.225$).
**(B)** Unlike 29e (see main text), no significant correlation was observed between landmark-locking score and the strength of spike-LFP theta phase coupling across neurons in MEC, PA, PO, and PR (from left to right), as indicated by the correlation coefficients ($r$) and the corresponding p-values in the figure titles. To draw comparisons between regions, a multiple regression model including regional identity (29e vs. others), spike-LFP theta phase coupling, and their interaction as predictors confirmed that the inverse relationship between spike-LFP theta phase coupling and landmark locking score was specific to area 29e (slope in 29e: $\beta = -20.05$, $t(457) = -4.2$, $p < 0.001$; interaction term: $\beta = 20.07$, $t(457) = 4.2$, $p < 0.001$).

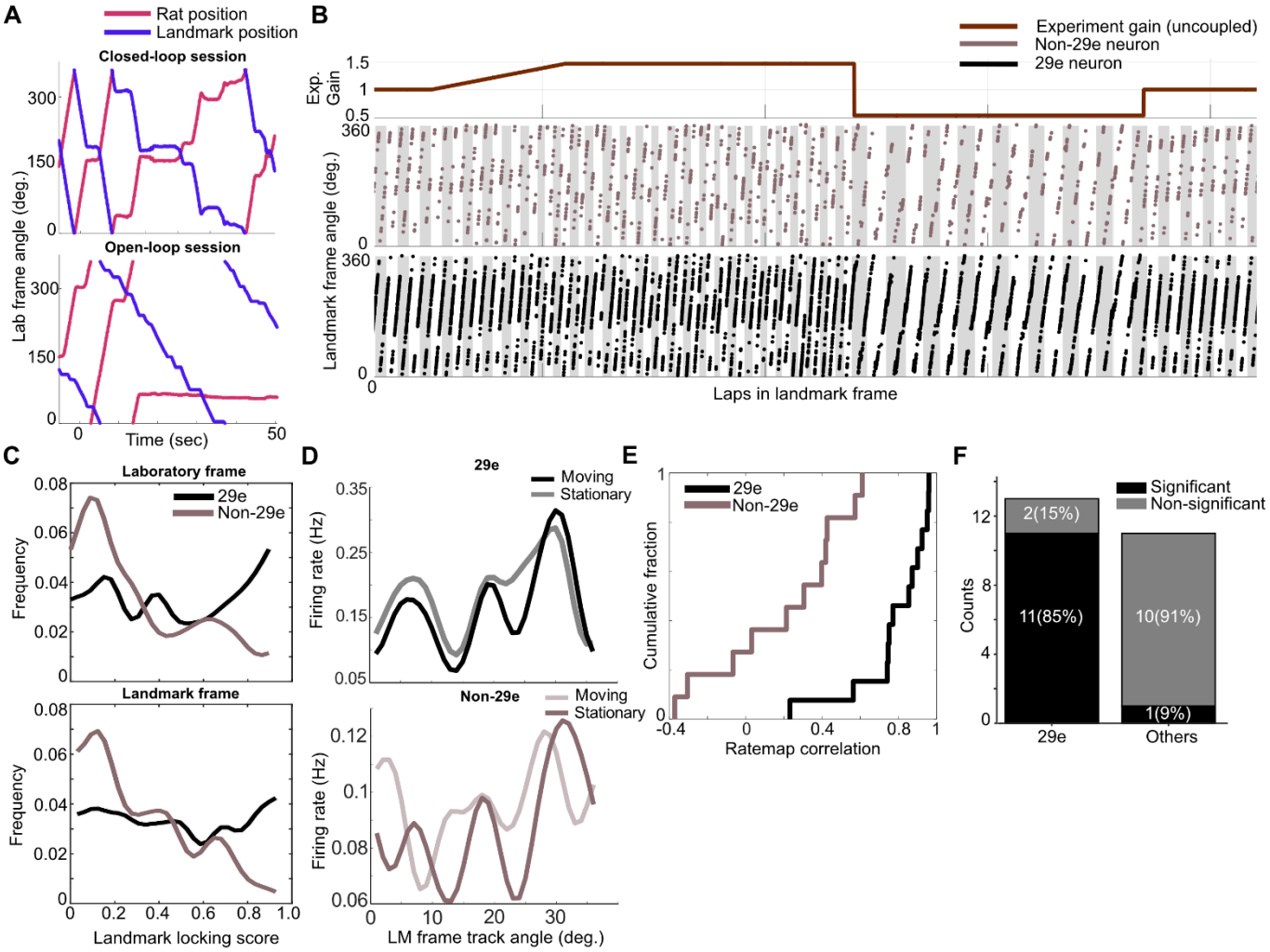


**Fig. S4.** 29e neurons remain landmark-anchored during open-loop landmark movement—including when the animal is stationary and landmarks are moving.
**(A)** Example rat and landmark trajectories in closed and open-loop experiments. Top: Closed-loop (G>1) session in which landmark rotation was coupled to the rat's movement. Bottom: Open-loop session in which landmark rotation was yoked to a rat's trajectory from a different session; note multi-second bout of immobility where the rat was stationary while landmarks rotated past it.
**(B)** Landmark-frame raster plot across laps (format same as in Fig. 3D–E) for an example non-29e neuron (middle) and a 29e neuron (bottom); the open-loop experiment gain is shown on top. The example non-29e neuron loses landmark anchoring towards the end of the gain ramp epoch, whereas the 29e neuron remained anchored to landmarks throughout.
**(C)** Distributions of landmark-locking scores in open-loop experiments for 29e (n = 31 neurons) versus non-29e (n = 40 neurons)

regions. Scores were computed with velocity filtering in the laboratory frame (top) and in the landmark frame (bottom). 29e neurons showed higher landmark-locking scores in both cases (Lab frame: median [IQR] 29e = 0.419 [0.191, 0.730], Non-29e = 0.230 [0.107, 0.517], Wilcoxon rank-sum test: $Z = 2.22$, $p = 0.026$; Landmark frame: median [IQR] 29e = 0.464 [0.241, 0.718], Non-29e = 0.261 [0.139, 0.470], Wilcoxon rank-sum test: $Z = 2.16$, $p = 0.031$).

**(D)** Comparison of firing rate profiles across track angle in landmark frame for an example 29e neuron (top) and a non-29e neuron (bottom) under moving and stationary conditions. Each example neuron represents the median value from the distribution of rate map correlations between moving and stationary conditions.
**(E)** Cumulative distributions of landmark frame rate-map correlations between stationary and moving epochs for landmark-anchored 29e (n = 13) and non-29e (n = 11) neurons. 29e neurons showed higher stationary-vs-moving rate map correlations than non-29e neurons(median [IQR] 29e = 0.855 [0.745, 0.931], Non-29e = 0.306 [-0.042, 0.425], Wilcoxon rank-sum test: $Z = 3.65$, $p < 0.001$).
**(F)** Proportion of landmark-anchored neurons with significant stationary-vs-moving rate-map similarity based on a shuffle test (10,000 circular-shifted shuffles of the stationary map relative to the moving map; α=0.05). Most 29e neurons remain significantly landmark-anchored when the animal was stationary, unlike non-29e neurons (Fisher's exact test: $p < 0.001$).

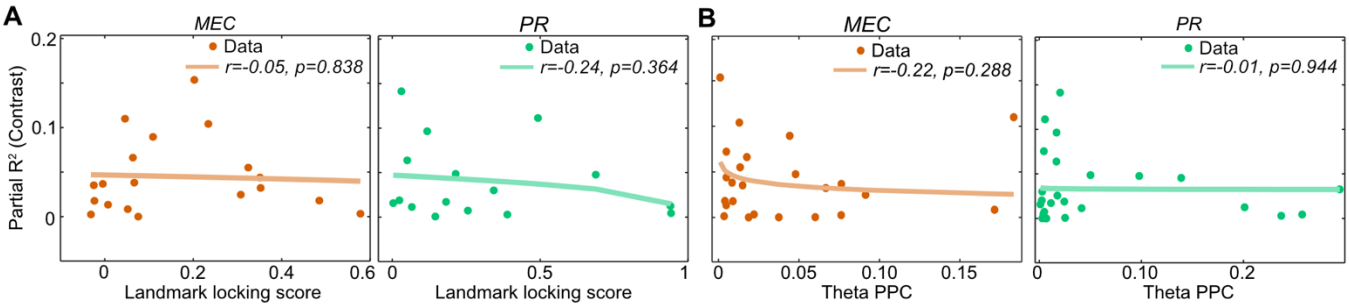


**Fig. S5.** (A) There was no clear dependence of partial $R^2$ for landmark contrast tuning on landmark-locking score within MEC or PR. Lines indicate the corresponding best fit. Each dot is a neuron. (B) Likewise, there was no dependence of partial $R^2$ for landmark contrast tuning on theta PPC. Same format as (A). Unlike 29e, which showed a significant negative relationship (see main text), there was no trend for MEC or PR. The specificity of the observed negative relationship to 29e was marginally significant, as measured by the interaction term of multiple regression model (slope in 29e: $\beta = -0.48$, $t(90) = -3.4$, $p < 0.001$; interaction term: $\beta = 0.44$, $t(90) = 1.90$, $p = 0.060$).

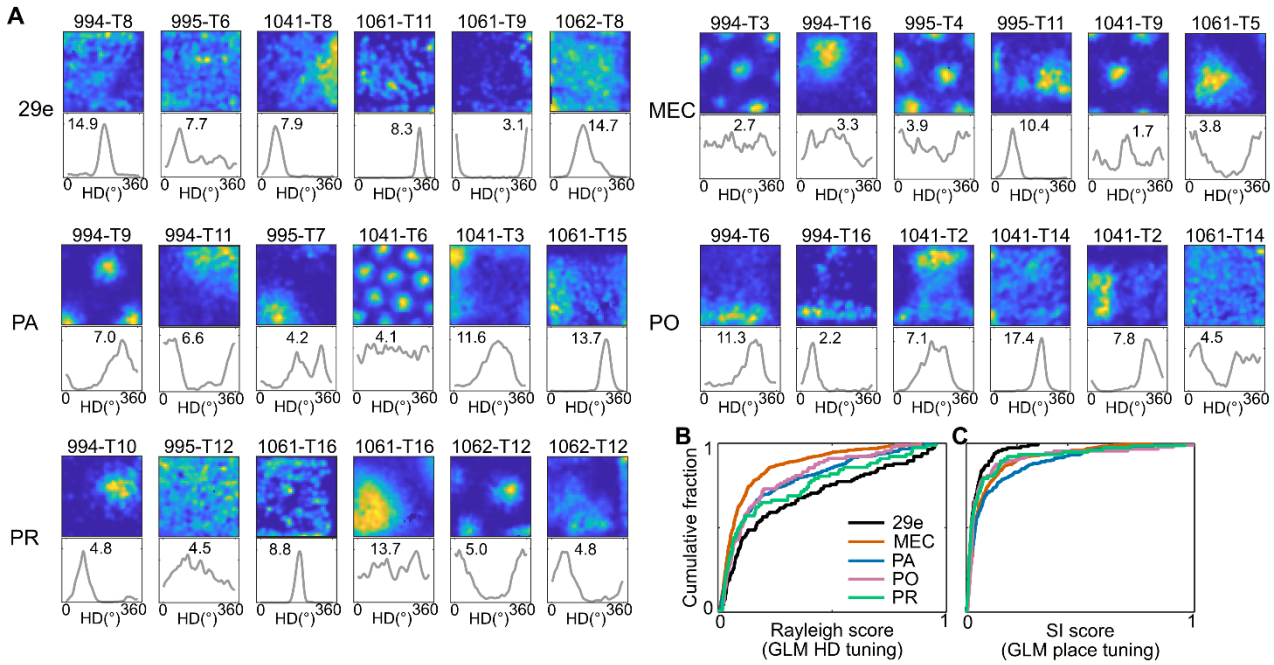


**Fig. S6.** Allocentric code of position and head direction across regions.
**(A)** Example spatially tuned neurons from each region. For each neuron, a 2D positional rate map (top) and a 1D allocentric head-direction (HD) tuning curve (bottom) are shown. Five representative neurons are displayed per region. Rat ID and tetrode number for each neuron are indicated above its rate map. The number inset in each HD plot denotes the peak-firing rate for head-direction tuning. The y-axis of each HD plot starts at zero.
**(B-C)** Cumulative distributions of Rayleigh HD scores (B) and Skaggs' SI scores (C) for all neurons across brain regions (color-coded as indicated). Unlike the main analysis (Fig. 5), Rayleigh and SI scores of each neuron were calculated from tuning curves

estimated by a generalized linear model (GLM) that jointly captures both 2D position and head direction. This approach supplements the traditional analysis and controls for potential behavioral bias, ensuring that apparent spatial or head-direction tuning differences across regions are not confounded by correlated foraging behavior.

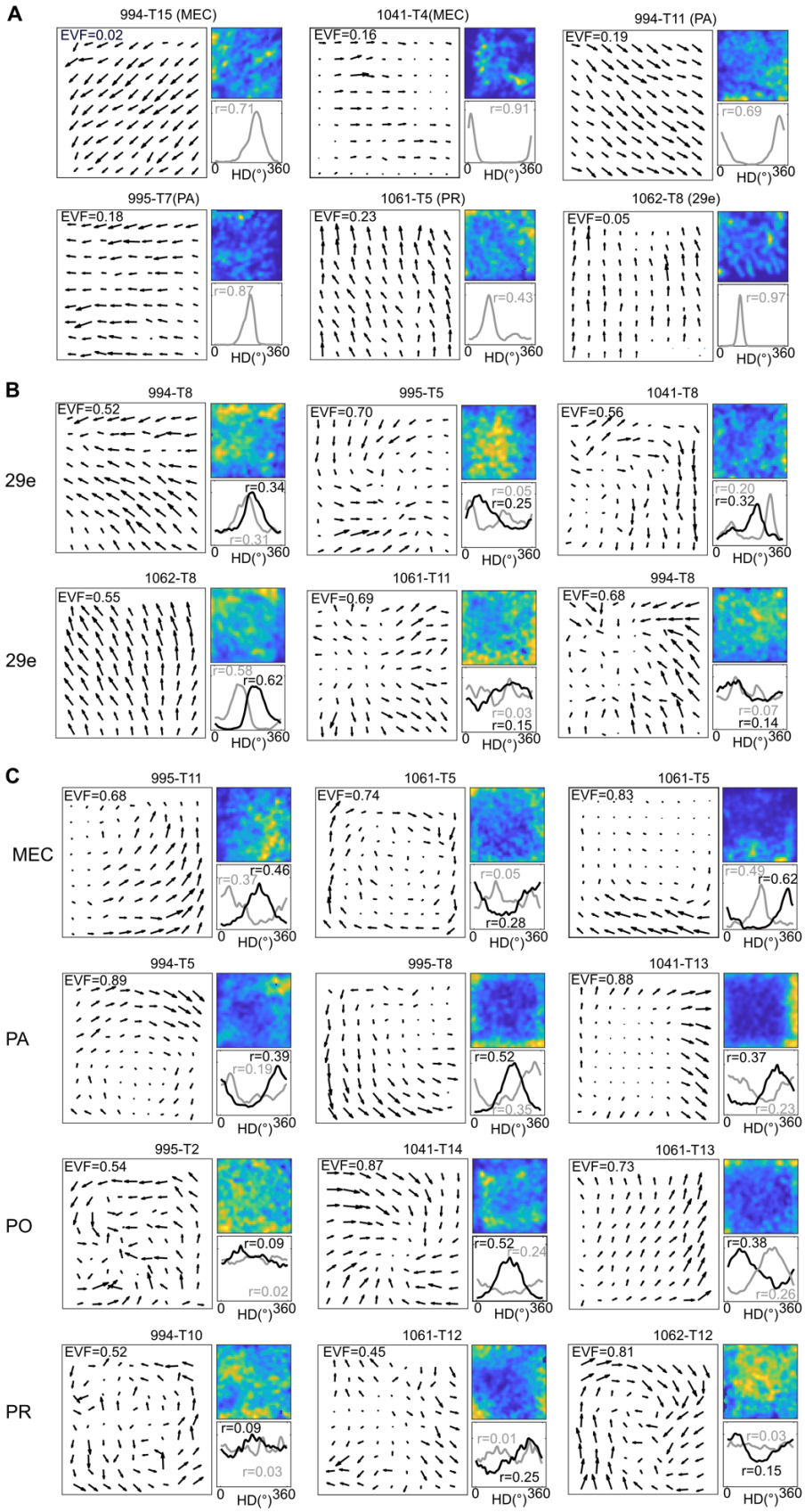


**Fig. S7.** Egocentric tuning of example neurons across different regions. For each neuron, the left panel shows the egocentric HD vector field, with the EVF score indicated at top left. Arrow direction depicts the neuron's preferred HD within a 15 × 15 cm positional bin centered at the arrow base; arrow size represents the product of the neuron's total firing rate (summed across head-

direction bins) and its mean resultant length (MRL), measured inside the same positional bin. This product is mathematically equal to the first (i.e., fundamental) Fourier component of the local HD tuning curve within the corresponding positional bin, and it represents the single sine that best fits this local HD tuning curve. On the right, the top panel shows the allocentric 2D positional rate map, and the bottom panel shows HD tuning curves in allocentric (gray) and egocentric (black) frames. Numbers in the HD plots denote the mean resultant length (r) of tuning in each frame.

**(A)** Example HD neurons that show classical, allocentric tuning. Notice that the preferred HD vectors are roughly parallel at all locations across the open arena, as expected from their allocentric nature. Rat ID and tetrode number for each neuron are indicated along with the region identity above the respective panels.

**(B)** Example egocentric neurons from 29E.

**(C)** Example egocentric neurons from MEC, PA, PO, and PR.

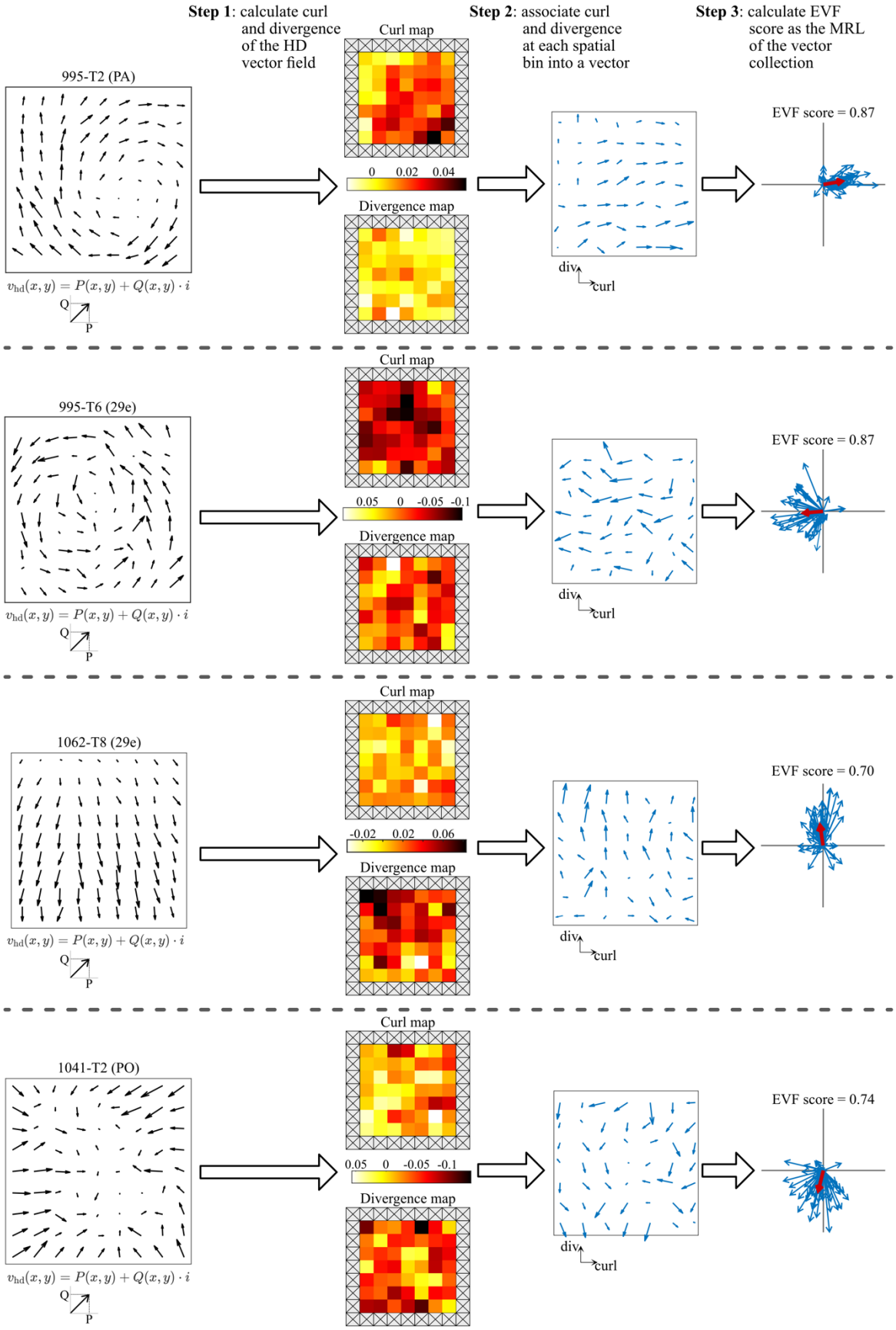


**Fig. S8.** Workflow for computing the anchor-free egocentric-vector-field (EVF) score, illustrated with four example head-direction (HD) cells. **Input**: HD vector field (left-most column). The HD tuning curve within each spatial bin (*x, y*) is reduced to a single vector corresponding to the first Fourier component of the circular tuning curve (i.e., the single sinusoid that, in a least-squares sense, best fits the full circular tuning curve). The phase of this Fourier component is mathematically equivalent to the preferred HD (i.e., the mean angular direction) and its amplitude equals the summed firing rate of the HD tuning curve × the mean resultant length of the HD tuning curve. Collectively, these HD tuning vectors define a two–dimensional vector field $v_{hd}(x,y) = P(x,y) + Q(x,y)i$, where $P$ and $Q$ are the horizontal components of each vector, and $i$ is the imaginary number corresponding to the unit vector in the vertical direction. **Step 1**: Curl- and divergence-maps. For every spatial bin, we compute $curl(x,y) =$

$\frac{\partial Q(x,y)}{\partial x} - \frac{\partial P(x,y)}{\partial y}$ and $div(x,y) = \frac{\partial P(x,y)}{\partial x} + \frac{\partial Q(x,y)}{\partial y}$. The resulting scalar values are displayed as heat maps (curl on top, divergence underneath), where lighter colors correspond to values close to 0, and darker colors correspond to progressively larger absolute values. Therefore, the darkest color can represent either a large positive or a large negative value, depending on the neuron. The color scale is normalized separately for each neuron so that its full dynamic range is visible**. Step 2**: Curl/divergence vectors. For each spatial bin, the ordered pair (curl, div) is treated as a new 2D vector (horizontal = curl, vertical = div), forming the curl-divergence field shown next. Curl captures rotational patterns (preferred egocentric bearing to the left or right; top two examples). Divergence captures radial patterns (preferred bearing to the front or back; bottom two examples). **Step 3**: Calculation of the EVF score. All (curl, div) vectors are replotted in polar coordinates (blue). The red arrow is obtained with the same first-Fourier-component approach used in column 1: it is the single vector that, in a least-squares sense, best represents the entire set. Consequently, its angle equals the circular mean direction of the (curl, div) vectors, and its length equals (mean vector length) × (mean resultant length) of those vectors. The anchor-free EVF score is the mean resultant length (MRL) itself—that is, the red-arrow length divided by the mean vector length—providing a measure of how consistently the egocentric pattern is expressed across the arena (0 = randomly distributed vectors, 1 = perfectly aligned vectors).

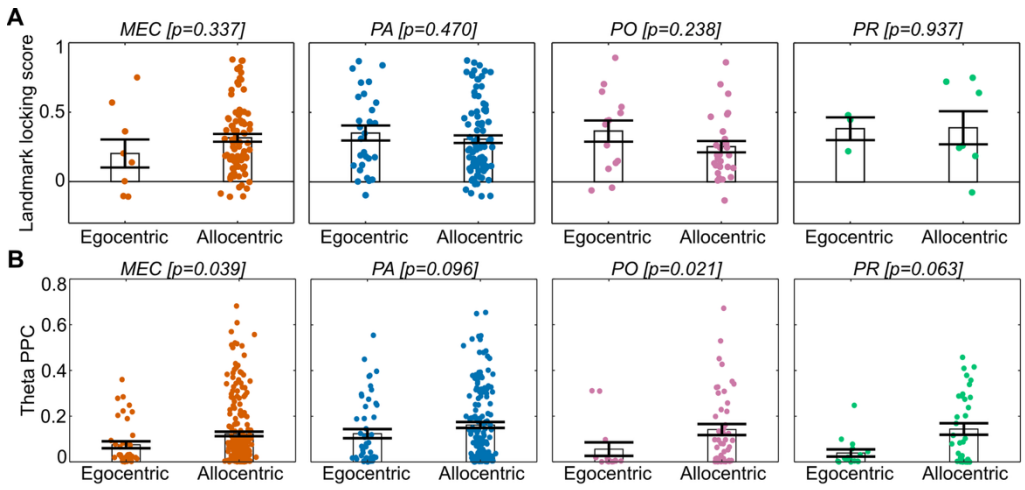


**Fig. S9.** Relationship between a cell's preferred spatial frame of reference (egocentric vs. allocentric) and three single-cell properties. **(A)** No significant relationship between landmark-locking scores and egocentric vs allocentric HD tuning in MEC, PA, PO, or PR. **(B)** In all regions, allocentric HD cells were more strongly coupled to theta than egocentric HD cells. Although, this difference was significant only in MEC and PO. Each dot represents a single neuron. Bars represent mean ± s.e.m. p-values shown above each subplot are from statistical tests comparing the egocentric and allocentric groups within that region (Wilcoxon's rank-sum test).

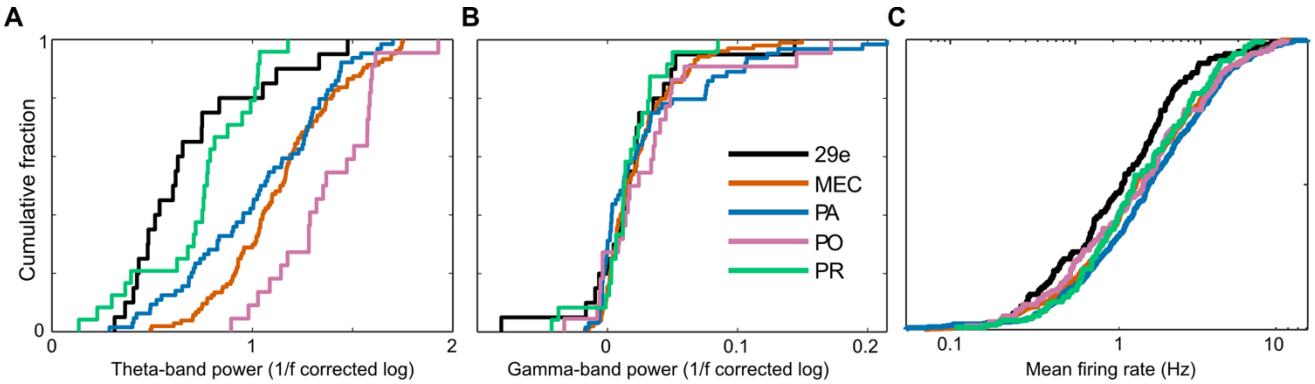


**Fig. S10. (A)** Cumulative distribution of 1/f-corrected theta-band power across regions. Area 29e had the lowest theta power (mean ± s.e.m. = 0.687 ± 0.072), which was significantly different than MEC (1.148 ± 0.028), PA (1.036 ± 0.043), and PO (1.365 ± 0.058), but not PR (0.735 ± 0.056) as determined by an ANOVA omnibus test $F(4,227) = 21.0$, $p < 0.001$; post-hoc t tests with Holm-Bonferroni correction 29e vs. MEC: $t(122) = -6.3$, $p < 0.001$; 29e vs. PA: $t(82) = -3.9$, $p < 0.001$; 29e vs. PO $t(38) = -7.25$, $p < 0.001$; 29e vs. PR: $t(42) = -0.52$, $p = 0.600$). **(B)** Same format as (A) for 1/f-corrected gamma-band power. There were no statistically significant differences in gamma-band power across regions (Kruskal-Wallis test $\chi^2(4) = 2.6$, $p = 0.614$). A linear-mixed effects model verified these findings: theta-band power in 29e was significantly lower than MEC ($p < 0.001$), PA ($p = 0.037$), and PO ($p < 0.001$), but not PR ($p = 0.810$), whereas gamma-band differences between 29e and other regions were non-significant (29e vs. MEC: $p = 0.291$, 29e vs. PA: $p = 0.423$, 29e vs. PO: $p = 0.535$, and 29e vs. PR: $p = 0.320$). (C) Cumulative distribution of single-neuron firing rates across regions. 29e neurons exhibited significantly lower mean firing rate (median [IQR] = 2.34 [0.90, 4.81]) compared to other regions except PO (MEC = 3.03 [1.45, 8.11], PA = 3.86 [1.61, 9.75], PR = 2.90 [1.42,

7.79], PO = 3.07 [0.97, 7.31]; Kruskal-Wallis test $\chi^2(4) = 19.4$, $p < 0.001$; post-hoc Wilcoxon rank-sum tests with Holm-Bonferroni correction 29e vs. MEC: $Z = -2.97$, $p = 0.008$; 29e vs. PA: $Z = -4.24$, $p < 0.001$; 29e vs. PO: $Z = -1.61$, $p = 0.105$; 29e vs. PR: $Z = -2.28$, $p = 0.044$).

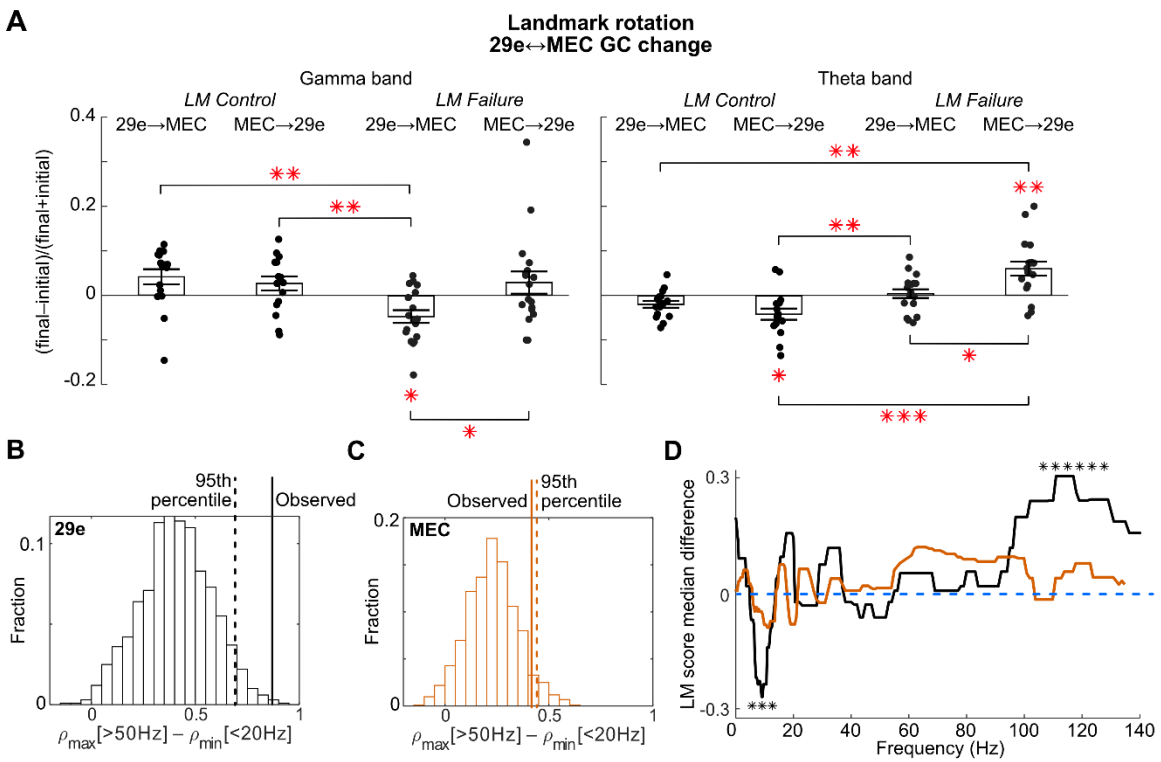


**Fig. S11.** Changes in directed LFP interactions of 29e and MEC tetrode pairs during landmark rotations and the relationship between their cross-regional spike-LFP coupling and landmark anchoring.

**(A)** Normalized changes in theta- and gamma-band Granger causality between 29e and MEC LFPs from the initial epoch to the final epoch across *LM-control* and *LM-failure* sessions. Theta band GCs showed significant changes in the MEC→29e direction during both *LM-control* (mean ± s.e.m. = –0.05 ± 0.01, Holm-Bonferroni corrected one-sample t-test $t(15) = -3.2$, p = 0.022) and *LM-failure* sessions (0.06 ± 0.01, $t(17) = -3.8$ $p = 0.005$); theta-band GC changes in the reciprocal direction (29e→MEC) were non-significant during both *LM-control* (–0.018 ± 0.008, $t(15) = p = 0.057$) and *LM-failure* sessions (0.003 ± 0.009, $t(17) = 0.35$ $p = 0.726$). For gamma-band GCs, changes were found significant in the 29e→MEC direction during *LM*-failure sessions (–0.047 ± 0.014, $t(17) = -3.3$ $p = 0.013$) and marginally significant in the same direction during *LM-control* sessions (0.041 ± 0.017, $t(15) = 2.4$ $p = 0.074$). Three-way repeated measures ANOVA (factors: session type, frequency band, and direction) identified significant session type x frequency band ($F(1,32) = 16.2$, $p < 0.001$) and significant session type x direction ($F(1,32) = 25.9$, $p < 0.001$) interactions, in addition to significant main effect of the direction ($F(1,32) = 5.0$, $p = 0.031$). Holm-Bonferroni corrected post-hoc pairwise t-tests revealed that, within theta-band, changes in MEC→29e GC during *LM-failure* sessions were significantly higher compared to the changes in [i] MEC→29e GC during *LM-control* sessions ($t(32) = 4.9$ $p < 0.001$) and [ii] 29e→MEC GC during *LM-control* sessions ($t(32) = 4.5$ $p < 0.001$) and [iii] 29e→MEC GC during *LM-failure* sessions ($t(17) = 2.9$ $p = 0.032$). Within the gamma band, directionally opposite but statistically similar differences were observed: changes in 29e→MEC gamma-band GC during *LM-failure* sessions were significantly lower compared to the changes in [i] 29e→MEC gamma-band GC during *LM-control* sessions ($t(32) = -3.9$ $p = 0.002$) and [ii] MEC→29e gamma-band GC during *LM-control* sessions ($t(32) = -3.4$ $p = 0.008$) and [iii] MEC→29e gamma-band GC during *LM-failure* sessions ($t(17) = -3.1$ $p = 0.027$).

**(B-C)** Permutation-based significance testing of the frequency-selective landmark locking–LFP phase coupling pattern for 29e **(B)** and MEC **(C)** neurons. At each permutation, landmark-locking scores from LM-failure sessions were randomly shuffled across 29e or MEC neurons. For each frequency bin (as in Fig. 7C), the correlation across neurons between their baseline PPC values (from the initial stationary-landmark epoch) and the shuffled landmark-locking scores was recalculated, generating a new correlation spectrum for each permutation. From this spectrum, the difference between the maximum correlation above 50 Hz and the minimum correlation below 20 Hz was computed. Repeating this procedure for 1000 permutations yielded null distributions of frequency-based correlation-coefficient differences. The observed difference (solid line) significantly exceeded the 95th percentile of the permutation distribution (dashed line) in 29e (B; $p = 0.006$) but not in MEC (C; $p = 0.078$).

**(D)** Comparison of landmark-locking scores between "PPC loss" and "PPC gain" neuron groups during LM-failure sessions for 29e (black) and MEC (orange) populations. At each frequency, neurons were divided into PPC loss or PPC gain groups, and the median difference in landmark-locking scores between groups was calculated across the population. The statistical significance of the difference between medians at each frequency was assessed with a Wilcoxon signed-rank test. To control for multiple comparisons, a cluster-based permutation test was used in conjunction with this rank test: contiguous frequency bins with uncorrected $p < 0.05$ were defined as clusters, and cluster-level statistics were compared to a null distribution generated by 1000

random permutations of group labels. Asterisks indicate frequency ranges with significant differences after cluster-level, permutation-based correction ($p < 0.05$).

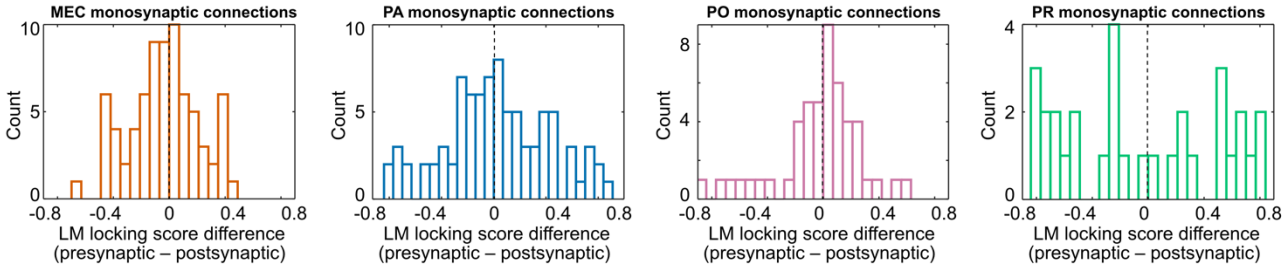


**Fig. S12.** Distributions of landmark-locking score differences between putative pre- and post-synaptic neuron pairs. There were no significant deviations from zero in any region (MEC: mean ± s.e.m. = –0.04 ± 0.03, one-sample t test $t(73) = -1.34$ $p = 0.181$; PA: mean ± s.e.m. = 0.02 ± 0.04, one-sample t test $t(85) = 0.57$ $p = 0.56$; PO: median [IQR] = 0.01 [–0.15, 0.12], Wilcoxon signed rank test $Z = -0.11$, $p = 0.905$; PR: median [IQR] = –0.17 [–0.56, 0.52], Wilcoxon signed rank test $Z = -0.48$ $p = 0.631$).

## References


1. J. Winson, Loss of hippocampal theta rhythm results in spatial memory deficit in the rat. *Science* **201**, 160–163 (1978).

2. G. Buzsáki, Theta oscillations in the hippocampus. *Neuron* **33**, 325–340 (2002).

3. L. L. Colgin, T. Denninger, M. Fyhn, T. Hafting, T. Bonnevie, O. Jensen, M.-B. Moser, E. I. Moser, Frequency of gamma oscillations routes flow of information in the hippocampus. *Nature* **462**, 353–357 (2009).

4. G. Buzsáki, E. I. Moser, Memory, navigation and theta rhythm in the hippocampal-entorhinal system. *Nat. Neurosci.* **16**, 130–138 (2013).

5. L. L. Colgin, Rhythms of the hippocampal network. *Nat. Rev. Neurosci.* **17**, 239–249 (2016).

6. M.-L. Mittelstaedt, H. Mittelstaedt, Homing by path integration in a mammal. *Naturwissenschaften* **67**, 566–567 (1980).

7. A. S. Etienne, K. J. Jeffery, Path integration in mammals. *Hippocampus* **14**, 180–192 (2004).

8. F. Savelli, J. J. Knierim, Origin and role of path integration in the cognitive representations of the hippocampus: computational insights into open questions. *J. Exp. Biol.* **222** (2019).

9. B. L. McNaughton, F. P. Battaglia, O. Jensen, E. I. Moser, M. B. Moser, Path integration and the neural basis of the “cognitive map.” *Nat. Rev. Neurosci.* **7**, 663–678 (2006).

10. J. Knierim, H. Kudrimoti, B. McNaughton, Place cells, head direction cells, and the learning of landmark stability. *J. Neurosci.* **15**, 1648–1659 (1995).

11. J. J. Knierim, H. S. Kudrimoti, B. L. McNaughton, Interactions between idiothetic cues and external landmarks in the control of place cells and head direction cells. *J. Neurophysiol.* **80**, 425–446 (1998).

12. R. P. Jayakumar, M. S. Madhav, F. Savelli, H. T. Blair, N. J. Cowan, J. J. Knierim, Recalibration of path integration in hippocampal place cells. *Nature* **566**, 533–537 (2019).

13. K. M. Gothard, W. E. Skaggs, B. L. McNaughton, Dynamics of mismatch correction in the hippocampal ensemble code for space: interaction between path integration and environmental cues. *J. Neurosci.* **16**, 8027–8040 (1996).

14. T. Hafting, M. Fyhn, S. Molden, M. Moser, E. I. Moser, Microstructure of a spatial map in the entorhinal cortex. *Nature* **436**, 801–806 (2005).

15. T. Solstad, C. N. Bocarra, E. Kropff, M. B. Moser, E. Moser, Representation of geometric borders in the entorhinal cortex. *Science* **322**, 1861–1865 (2008).

16. F. Savelli, D. Yoganarasimha, J. J. Knierim, Influence of boundary removal on the spatial representations of the medial entorhinal cortex. *Hippocampus* **18**, 1270–1282 (2008).

17. E. Kropff, J. E. Carmichael, M.-B. Moser, E. I. Moser, Speed cells in the medial entorhinal cortex. *Nature* **523**, 419–424 (2015).

18. F. Sargolini, M. Fyhn, T. Hafting, B. L. McNaughton, M. P. Witter, M.-B. Moser, E. I. Moser, Conjunctive representation of position, direction, and velocity in entorhinal cortex. *Science* **312**, 758–762 (2006).

19. H. Stensola, T. Stensola, T. Solstad, K. Frøland, M.-B. Moser, E. I. Moser, The entorhinal grid map is discretized. *Nature* **492**, 72–78 (2012).

20. S. Ding, Comparative anatomy of the prosubiculum, subiculum, presubiculum, postsubiculum, and parasubiculum in human, monkey, and rodent. *J. Comp. Neurol.* **521**, 4145–4162 (2013).

21. K. Mikellidou, J. W. Kurzawski, F. Frijia, D. Montanaro, V. Greco, D. C. Burr, M. C. Morrone, Area prostriata in the human brain. *Curr. Biol.* **27**, 3056-3060.e3 (2017).

22. H.-H. Yu, T. A. Chaplin, A. J. Davies, R. Verma, M. G. P. Rosa, A specialized area in limbic cortex for fast analysis of peripheral vision. *Curr. Biol.* **22**, 1351–1357 (2012).

23. T. W. Blackstad, Commissural connections of the hippocampal region in the rat, with special reference to their mode of termination. *J. Comp. Neurol.* **105**, 417–537 (1956).

24. F.-M. Š. Haug, *Sulphide Silver Pattern and Cytoarchitectonics of Parahippocampal Areas in the Rat* (Springer Berlin Heidelberg, Berlin, Heidelberg, 1976; http://link.springer.com/10.1007/978-3-642-66448-9).

25. C.-H. Chen, J.-M. Hu, S.-Y. Zhang, X.-J. Xiang, S.-Q. Chen, S.-L. Ding, Rodent area prostriata converges multimodal hierarchical inputs and projects to the structures important for visuomotor behaviors. *Front. Neurosci.* **15**, 772016 (2021).

26. J.-M. Hu, C.-H. Chen, S.-Q. Chen, S.-L. Ding, Afferent projections to area prostriata of the mouse. *Front. Neuroanat.* **14**, 605021 (2020).

27. C.-H. Chen, J.-M. Hu, S.-Q. Chen, S.-M. Liu, S.-L. Ding, Homotopic commissural projections of area prostriata in rat and mouse: comparison with presubiculum and parasubiculum. *Front. Neural Circuits* **14**, 605332 (2020).

28. W. Lu, S. Chen, X. Chen, J. Hu, A. Xuan, S. Ding, Localization of area prostriata and its connections with primary visual cortex in rodent. *J. Comp. Neurol.* **528**, 389–406 (2020).

29. M. S. Madhav, R. P. Jayakumar, S. G. Lashkari, F. Savelli, H. T. Blair, J. J. Knierim, N. J. Cowan, The dome: a virtual reality apparatus for freely locomoting rodents. *J. Neurosci. Methods* **368**, 109336 (2022).

30. M. S. Madhav, R. P. Jayakumar, B. Y. Li, S. G. Lashkari, K. Wright, F. Savelli, J. J. Knierim, N. J. Cowan, Control and recalibration of path integration in place cells using optic flow. *Nat. Neurosci.* **27**, 1599–1608 (2024).

31. R. P. Jayakumar, Y. Sueoka, M. K. Ferreyros, B. Y. Li, M. S. Madhav, X. Chen, J. J. Knierim, N. J. Cowan, Synchronized path-integration recalibration but distinct landmark-control dynamics in head direction and CA1 place cells. Neuroscience [Preprint] (2025). https://doi.org/10.1101/2025.10.08.681135.

32. W. Skaggs, B. McNaughton, K. Gothard, “An information-theoretic approach to deciphering the hippocampal code” in *Advances in Neural Information Processing Systems*, S. Hanson, J. Cowan, C. Giles, Eds. (Morgan-Kaufmann, 1992)vol. 5.

33. E. Batschelet, *Circular Statistics in Biology* (Academic Press, 1981)*Mathematics in biology*.

34. J. P. Goodridge, J. S. Taube, Interaction between the postsubiculum and anterior thalamus in the generation of head direction cell activity. *J. Neurosci.* **17**, 9315–9330 (1997).

35. F. Cacucci, C. Lever, T. J. Wills, N. Burgess, J. O’Keefe, Theta-modulated place-by-direction cells in the hippocampal formation in the rat. *J. Neurosci.* **24**, 8265–8277 (2004).

36. N. Burgess, F. Cacucci, C. Lever, J. O’Keefe, Characterizing multiple independent behavioral correlates of cell firing in freely moving animals. *Hippocampus* **15**, 149–153 (2005).

37. J. S. Taube, R. U. Muller, J. B. Ranck, Head-direction cells recorded from the postsubiculum in freely moving rats. I. Description and quantitative analysis. *J. Neurosci.* **10**, 420–435 (1990).

38. A. Jeewajee, C. Barry, J. O'Keefe, N. Burgess, Grid cells and theta as oscillatory interference: electrophysiological data from freely moving rats. *Hippocampus* **18**, 1175–1185 (2008).

39. C. N. Boccara, F. Sargolini, V. H. Thoresen, T. Solstad, M. P. Witter, E. I. Moser, M.-B. Moser, Grid cells in pre- and parasubiculum. *Nat Neurosci* **13**, 987–994 (2010).

40. S. S. Deshmukh, D. Yoganarasimha, H. Voicu, J. J. Knierim, Theta modulation in the medial and the lateral entorhinal cortices. *J. Neurophysiol.* **104**, 994–1006 (2010).

41. M. M. Yartsev, M. P. Witter, N. Ulanovsky, Grid cells without theta oscillations in the entorhinal cortex of bats. *Nature* **479**, 103–107 (2011).

42. M. Vinck, M. Van Wingerden, T. Womelsdorf, P. Fries, C. M. A. Pennartz, The pairwise phase consistency: a bias-free measure of rhythmic neuronal synchronization. *Neuroimage* **51**, 112–122 (2010).

43. E. Maris, R. Oostenveld, Nonparametric statistical testing of EEG- and MEG-data. *J. Neurosci. Methods* **164**, 177–190 (2007).

44. M. Dhamala, G. Rangarajan, M. Ding, Analyzing information flow in brain networks with nonparametric granger causality. *Neuroimage* **41**, 354–362 (2008).

45. Y. B. Saalmann, M. A. Pinsk, L. Wang, X. Li, S. Kastner, The pulvinar regulates information transmission between cortical areas based on attention demands. *Science* **337**, 753–756 (2012).

46. A. M. Bastos, J. Vezoli, C. A. Bosman, J.-M. Schoffelen, R. Oostenveld, J. R. Dowdall, P. De Weerd, H. Kennedy, P. Fries, Visual areas exert feedforward and feedback influences through distinct frequency channels. *Neuron* **85**, 390–401 (2015).

47. A. M. Bastos, W. M. Usrey, R. A. Adams, G. R. Mangun, P. Fries, K. J. Friston, Canonical microcircuits for predictive coding. *Neuron* **76**, 695–711 (2012).

48. G. Michalareas, J. Vezoli, S. van Pelt, J.-M. Schoffelen, H. Kennedy, P. Fries, Alpha-beta and gamma rhythms subserve feedback and feedforward influences among human visual cortical areas. *Neuron* **89**, 384–397 (2016).

49. J. D. Semedo, A. I. Jasper, A. Zandvakili, A. Krishna, A. Aschner, C. K. Machens, A. Kohn, B. M. Yu, Feedforward and feedback interactions between visual cortical areas use different population activity patterns. *Nat. Commun.* **13**, 1099 (2022).

50. T. Van Kerkoerle, M. W. Self, B. Dagnino, M.-A. Gariel-Mathis, J. Poort, C. Van Der Togt, P. R. Roelfsema, Alpha and gamma oscillations characterize feedback and feedforward processing in monkey visual cortex. *Proc. Natl. Acad. Sci.* **111**, 14332–14341 (2014).

51. M. P. Brandon, A. R. Bogaard, C. P. Libby, M. A. Connerney, K. Gupta, M. E. Hasselmo, Reduction of theta rhythm dissociates grid cell spatial periodicity from directional tuning. *Science* **332**, 595–599 (2011).

52. J. Koenig, A. N. Linder, J. K. Leutgeb, S. Leutgeb, The spatial periodicity of grid cells is not sustained during reduced theta oscillations. *Science* **332**, 592–595 (2011).

53. L. L. Colgin, Mechanisms and functions of theta rhythms. *Annu. Rev. Neurosci.* **36**, 295–312 (2013).

54. C. Wang, X. Chen, H. Lee, S. S. Deshmukh, D. Yoganarasimha, F. Savelli, J. J. Knierim, Egocentric coding of external items in the lateral entorhinal cortex. *Science* **362**, 945–949 (2018).

55. P. A. LaChance, J. Graham, B. L. Shapiro, A. J. Morris, J. S. Taube, Landmark-modulated directional coding in postrhinal cortex. *Sci. Adv.* **8**, eabg8404 (2022).

56. K. Brodmann, *Vergleichende Lokalisationslehre Der Grosshirnrinde : In Ihren Prinzipien Dargestellt Auf Grund Des Zellenbaues* (Barth, Leipzig, 2 unveränderte Aufl., 1909).

57. W. J. S. Krieg, Connections of the cerebral cortex. I. The albino rat. A. Topography of the cortical areas. *J. Comp. Neurol.* **84**, 221–275 (1946).

58. W. J. S. Krieg, Connections of the cerebral cortex. I. The albino rat. B. Structure of the cortical areas. *J. Comp. Neurol.* **84**, 277–323 (1946).

59. V. S. Caviness, Architectonic map of neocortex of the normal mouse. *J. Comp. Neurol.* **164**, 247–263 (1975).

60. J. E. Rose, C. N. Woolsey, Structure and relations of limbic cortex and anterior thalamic nuclei in rabbit and cat. *J. Comp. Neurol.* **89**, 279–347 (1948).

61. B. A. Vogt, A. Peters, Form and distribution of neurons in rat cingulate cortex: areas 32, 24, and 29. *J. Comp. Neurol.* **195**, 603–625 (1981).

62. H. Stephan, Ed., *Allocortex* (Springer Berlin Heidelberg, Berlin, Heidelberg, 1975)vol. 4/9 of *Handbuch der mikroskopischen Anatomie des Menschen*.

63. M. P. Witter, Organization of the Entorhinal-Hippocampal System: A Review of Current Anatomical Data. *Hippocampus* **3**, 33–44 (1993).

64. C. N. Boccara, L. J. Kjonigsen, I. M. Hammer, J. G. Bjaalie, T. B. Leergaard, M. P. Witter, A three-plane architectonic atlas of the rat hippocampal region. *Hippocampus* **25**, 838–857 (2015).

65. A. V. Ferreira, The cortical areas of the albino rat studied by silver impregnation. *J. Comp. Neurol.* **95**, 177–243 (1951).

66. S. Chen, C. Chen, X. Xiang, S. Zhang, S. Ding, Chemoarchitecture of area prostriata in adult and developing mice: comparison with presubiculum and parasubiculum. *J. Comp. Neurol.* **530**, 2486–2517 (2022).

67. K. S. Rockland, Visual system: prostriata — a visual area off the beaten path. *Curr. Biol.* **22**, R571–R573 (2012).

68. M. Tamietto, D. A. Leopold, Visual cortex: the eccentric area prostriata in the human brain. *Curr. Biol.* **28**, R17–R19 (2018).

69. C. B. Canto, N. Koganezawa, P. Beed, E. I. Moser, M. P. Witter, All layers of medial entorhinal cortex receive presubicular and parasubicular inputs. *J. Neurosci.* **32**, 17620–17631 (2012).

70. P. Preston-Ferrer, S. Coletta, M. Frey, A. Burgalossi, Anatomical organization of presubicular head-direction circuits. *eLife* **5**, e14592 (2016).

71. R. M. Yoder, B. J. Clark, J. S. Taube, Origins of landmark encoding in the brain. *Trends Neurosci.* **34**, 561–571 (2011).

72. A. S. Alexander, D. A. Nitz, Retrosplenial cortex maps the conjunction of internal and external spaces. *Nat Neurosci* **18**, 1143–1151 (2015).

73. A. Peyrache, N. Schieferstein, G. Buzsáki, Transformation of the head-direction signal into a spatial code. *Nat. Commun.* **8**, 1752 (2017).

74. P. A. LaChance, T. P. Todd, J. S. Taube, A sense of space in postrhinal cortex. *Science* **365**, eaax4192 (2019).

75. A. S. Alexander, L. C. Carstensen, J. R. Hinman, F. Raudies, G. W. Chapman, M. E. Hasselmo, Egocentric boundary vector tuning of the retrosplenial cortex. *Sci. Adv.* **6**, eaaz2322.

76. P. Andrey, Y. Maurin, *Free-D*: an integrated environment for three-dimensional reconstruction from serial sections. *J. Neurosci. Methods* **145**, 233–244 (2005).

77. M. Quigley, K. Conley, B. Gerkey, J. Faust, T. Foote, J. Leibs, R. Wheeler, A. Y. Ng, “ROS: an open-source robot operating system” in *ICRA Workshop on Open Source Software* (Kobe, 2009)vol. 3, p. 5.

78. B. P. Vagvolgyi, R. P. Jayakumar, M. S. Madhav, J. J. Knierim, N. J. Cowan, Wide-angle, monocular head tracking using passive markers. *Journal of Neuroscience Methods* **368**, 109453 (2022).

79. J. E. Chung, J. F. Magland, A. H. Barnett, V. M. Tolosa, A. C. Tooker, K. Y. Lee, K. G. Shah, S. H. Felix, L. M. Frank, L. F. Greengard, A fully automated approach to spike sorting. *Neuron* **95**, 1381-1394.e6 (2017).

80. G. Secer, B. Krishnan, N. J. Cowan, J. J. Knierim, “Automated vs. manual spike sorting: assessing the quality of automated spike sorting using grid cells” in *2023 Neuroscience Meeting Planner* (Society for Neuroscience, Washington, D.C.).

81. A. P. Buccino, C. L. Hurwitz, S. Garcia, J. Magland, J. H. Siegle, R. Hurwitz, M. H. Hennig, SpikeInterface, a unified framework for spike sorting. *eLife* **9**, e61834 (2020).

82. S. S. Shapiro, M. B. Wilk, An analysis of variance test for normality (complete samples). *Biometrika* **52**, 591–611 (1965).

83. S. S. Shapiro, R. S. Francia, An approximate analysis of variance test for normality. *J. Am. Stat. Assoc.* **67**, 215–216 (1972).

84. J. P. Royston, An extension of shapiro and wilk’s W test for normality to large samples. *Appl. Stat.* **31**, 115 (1982).

85. P. Royston, Approximating the shapiro-wilk W-test for non-normality. *Stat. Comput.* **2**, 117–119 (1992).

86. T. Chen, C. Guestrin, “XGBoost: a scalable tree boosting system” in *Proceedings of the 22nd ACM SIGKDD International Conference on Knowledge Discovery and Data Mining* (ACM, San Francisco California USA, 2016; https://dl.acm.org/doi/10.1145/2939672.2939785), pp. 785–794.

87. S. Royer, B. V. Zemelman, A. Losonczy, J. Kim, F. Chance, J. C. Magee, G. Buzsáki, Control of timing, rate and bursts of hippocampal place cells by dendritic and somatic inhibition. *Nat. Neurosci.* **15**, 769–775 (2012).

88. J. Platt, Probabilistic outputs for support vector machines and comparisons to regularized likelihood methods. *Adv, Large Margin Classif,* **10** (2000).

89. A. Niculescu-Mizil, R. Caruana, “Predicting good probabilities with supervised learning” in *Proceedings of the 22nd International Conference on Machine Learning* (Association for Computing Machinery, New York, NY, USA, 2005)*ICML ’05*, pp. 625–632.

90. D. H. Wolpert, Stacked generalization. *Neural Networks* **5**, 241–259 (1992).

91. M. Zaheer, S. Kottur, S. Ravanbakhsh, B. Poczos, R. R. Salakhutdinov, A. J. Smola, “Deep sets” in *Advances in Neural Information Processing Systems* (Curran Associates, Inc., 2017)vol. 30.

92. C. Chow, On optimum recognition error and reject tradeoff. *IEEE Trans, Inf, Theor,* **16**, 41–46 (1970).

93. R. El-Yaniv, Y. Wiener, On the foundations of noise-free selective classification. *J. Mach. Learn. Res.* **11**, 1605–1641 (2010).

94. T. Donoghue, M. Haller, E. J. Peterson, P. Varma, P. Sebastian, R. Gao, T. Noto, A. H. Lara, J. D. Wallis, R. T. Knight, A. Shestyuk, B. Voytek, Parameterizing neural power spectra into periodic and aperiodic components. *Nat. Neurosci.* **23**, 1655–1665 (2020).

95. G. Kühn, H. E. Rashidy, F. Calegari, S. Dhingra, Aperiodicity in mouse CA1 and DG power spectra. bioRxiv [Preprint] (2025). https://doi.org/10.1101/2025.01.30.635678.

96. P. Hegedüs, J. Heckenast, B. Hangya, Differential recruitment of ventral pallidal e-types by behaviorally salient stimuli during pavlovian conditioning. *iScience* **24** (2021).

97. R. Oostenveld, P. Fries, E. Maris, J.-M. Schoffelen, FieldTrip: open source software for advanced analysis of MEG, EEG, and invasive electrophysiological data. *Comput. Intell. Neurosci.* **2011**, 156869 (2011).

98. J. D. Monaco, G. Rao, E. D. Roth, J. J. Knierim, Attentive scanning behavior drives one-trial potentiation of hippocampal place fields. *Nat. Neurosci.* **17**, 725–731 (2014).

99. A. V. Olypher, P. Lánský, R. U. Muller, A. A. Fenton, Quantifying location-specific information in the discharge of rat hippocampal place cells. *J. Neurosci. Methods* **127**, 123–135 (2003).

100. C. E. Shannon, A mathematical theory of communication. *Bell Syst. Tech. J.* **27**, 379–423 (1948).

101. B. C. Souza, R. Pavão, H. Belchior, A. B. L. Tort, On information metrics for spatial coding. *Neuroscience* **375**, 62–73 (2018).

102. M. Ester, H.-P. Kriegel, J. Sander, X. Xu, "A density-based algorithm for discovering clusters in large spatial databases with noise" in *Proceedings of the Second International Conference on Knowledge Discovery and Data Mining* (AAAI Press, Portland, Oregon, 1996)*KDD'96*, pp. 226–231.

103. B. W. Silverman, Density estimation for statistics and data analysis. *Biom. J.* **30**, 876–877 (1988).

104. K. Hardcastle, N. Maheswaranathan, S. Ganguli, L. M. Giocomo, A Multiplexed, Heterogeneous, and Adaptive Code for Navigation in Medial Entorhinal Cortex. *Neuron* **94**, 375-387.e7 (2017).

105. G. Carter, C. Knapp, A. Nuttall, Estimation of the magnitude-squared coherence function via overlapped fast fourier transform processing. *IEEE Trans. Audio Electroacoust.* **21**, 337–344 (1973).

106. M. R. Jarvis, P. P. Mitra, Sampling properties of the spectrum and coherency of sequences of action potentials. *Neural Comput.* **13**, 717–749 (2001).

107. G. Nolte, O. Bai, L. Wheaton, Z. Mari, S. Vorbach, M. Hallett, Identifying true brain interaction from EEG data using the imaginary part of coherency. *Clin. Neurophysiol.* **115**, 2292–2307 (2004).

108. V. Saravanan, G. J. Berman, S. J. Sober, Application of the hierarchical bootstrap to multi-level data in neuroscience. *Neurons Behav. DATA Anal. Theory* **3**, 0–29 (2020).

109. A. M. Bastos, J.-M. Schoffelen, A tutorial review of functional connectivity analysis methods and their interpretational pitfalls. *Front. Syst. Neurosci.* **9**, 0–23 (2016).

110. R. Kobayashi, S. Kurita, A. Kurth, K. Kitano, K. Mizuseki, M. Diesmann, B. J. Richmond, S. Shinomoto, Reconstructing neuronal circuitry from parallel spike trains. *Nat. Commun.* **10**, 4468 (2019).

111. D. Endo, R. Kobayashi, R. Bartolo, B. B. Averbeck, Y. Sugase-Miyamoto, K. Hayashi, K. Kawano, B. J. Richmond, S. Shinomoto, A convolutional neural network for estimating synaptic connectivity from spike trains. *Sci. Rep.* **11**, 12087 (2021).